REACTIONS OF PYRIDAZINE AND SOME GASEOUS OXIDES ON THE GE(100) SURFACE

HE JINGHUI

NATIONAL UNIVERSITY OF SINGAPORE

2012

REACTIONS OF PYRIDAZINE AND SOME GASEOUS OXIDES ON THE GE(100) SURFACE

HE JINGHUI
(M.Sc., NANJING UNIVERSITY)

A THESIS SUBMITTED
FOR THE DEGREE OF DOCTOR OF PHILOSOPHY

DEPARTMENT OF CHEMISTRY
NATIONAL UNIVERSITY OF SINGAPORE

2012

Thesis Declaration

The work in this thesis is the original work of He Jinghui, performed independently under the supervision of Xu Guo Qin, (in the laboratory S7-01-28), Chemistry Department, National University of Singapore, between Aug, 2008 and July, 2012.

The content of the thesis has been partly published in:

1). Unique geometric and electronic structure of CO adsorbed on Ge(100): A DFT study.

He, J. H., Zhang, Y. P., Mao, W., Xu, G. Q. and Tok, E. S.

Surface Science, **2012**, 606(9-10): 784-790.

Name	Signature	Date

Acknowledgement

I owe my most sincere gratitude to my supervisor, Prof. Xu Guo Qin for his invaluable and continuous guidance of this work. His encouragement, support and friendly personalities were priceless for my graduate study. I learnt a lot from him about the wise of study, work and life, which will benefit my whole life.

I am very grateful to Prof. Tok Eng Soon, Prof. Cheng Han Song, Prof. Kang Hway Chuan, for their valuable guidance and useful discussions during my research work.

I would like to thank Dr. Dong Dong, for his guidance in theoretical modeling and linux programming. I also gratefully acknowledge Dr. Zhang Yong Ping, Dr. Wang Shuai, Dr. Shao Yan Xia, Dr. Tang Hai hua, Dr. Wu Ji Hong and Mao Wei for their help and suggestions during my experiments.

I appreciate my group colleagues, Tan Wee Boon, Li Wan chao, Chen Zhang Xian and others from the laboratory for their generous support for my research work.

I would like to extend my heartful thanks to my wife, Xia Lin ling for her love, patience and support. To my parents, my brother and sister, I am forever thankful for their everlasting encouragement and support.

Finally, I thank National University of Singapore for awarding me the research scholarship.

Contents

Thesis Declaration i

Acknowledgement ii

Table Of Contents i

Summary vi

List of Tables i

List of Figures ii

List of Publications iv

Chapter 1 Introduction 1

1.1 Motivation 1

1.2 Ge(100) and its surface reconstruction 4

1.2.1 Dimer reconstruction of Ge(100) 4

1.2.2 Buckling of dimers 6

1.2.3 Higher order reconstructions 6

1.3 Reaction mechanisms of organic molecules on Ge(100) 7

1.3.1 Cycloadditions 7

1.3.1.1 [2+2] cycloadditions 8

1.3.1.2 [4+2] cycloadditions 10
1.3.1.3 The mechanism of cycloadditions 12
1.3.2 Dative bonding 16
1.3.2.1 Dative bonding of Lewis acids: Ge→B, Ge→Al 16
1.3.2.2 Dative bonding of Lewis bases: N→Ge 16
1.3.2.3 Dative bonding of Lewis bases: S→Ge 18
1.3.2.4 Dative bonding of Lewis bases: O→Ge 18
1.3.3 Dissociation 19
1.3.3.1 N-H dissociation 20
1.3.3.2 O-H dissociation 21
1.3.3.3 S-H dissociation 22
1.3.3.4 C-H dissociation: ene-like reaction 22
1.3.4 Reactions of multifunctional molecules 23
1.4 Reactions of gaseous molecules on Ge(100) 25
1.4.1 Reactions of oxygen 25
1.4.2 Reactions of hydrogen 27
1.4.2.1 Monohydride and dihydride 28
1.4.2.2 Hemihydrides 29
1.4.3 Reactions of halogens and halides 30
1.4.3.1 Reactions of halogens 31
1.4.3.2 Reactions of hydrogen halides 32
1.4.4 Reactions of gaseous oxides 32
1.4.4.1 Reactions of nitrogen oxides: NO and N_2O 33

1.4.4.2 Reactions of carbon oxides: CO and CO_2 34

1.5 Ge in catalysis 35

1.6 Objectives and scope 37

Chapter 2 Experimental and computational methods 41

2.1 Principles of surface analytical techniques 41

2.2 Scanning tunneling microscopy (STM) 42

2.2.1 Working principle 43

2.2.2 Instrumentation 45

2.2.3 STM theory 47

2.2.3.1 Bardeen's approximation 47

2.2.3.2 Tersoff-Hamman approximation 48

2.2.3.3 Lang's approximation 49

2.2.4 Orbital resolution with STM 51

2.2.4.1 Substrate requirements 52

2.2.4.2 Modifications of STM tips 54

2.2.4.3 Choice of molecules 57

2.2.4.4 Issues of orbital imaging 58

2.3 High resolution electron energy loss spectroscopy (HREELS) 59

2.4 Experimental procedures 63

2.4.1 Ultra-high vacuum chamber (UHV) 63

2.4.2 Sample preparation 67

2.4.3 Organic molecules 67

2.5 Theoretical Calculations 68

2.5.1 Density functional theory 68

2.5.1.1 Schördinger equation 68

2.5.1.2 Kohn-Sham equation 69

2.5.2 Exchange-correlation functionals 72

2.5.3 SCF Solution of the KS equation 74

2.5.3.1 Variational principle 74

2.5.3.2 Periodic systems and Bloch theorem 75

2.5.3.3 Basis set: plane waves 76

2.5.3.4 Basis set: linear combination of atomic orbitals (LCAO) 78

2.5.3.5 Evaluation of the electron density and total energy . . . 79

2.5.3.6 Self-consistent field procedure to solve the Kohn-Sham equation 80

2.5.4 Calculation of electron-related properties 82

2.5.4.1 Vibration frequencies calculation 82

2.5.4.2 STM image simulation 84

2.5.4.3 Transition state search 84

2.5.5 Calculation softwares 85

2.5.5.1 Siesta 85

2.5.5.2 CASTEP 86

2.5.6 Computational procedures 87

Chapter 3 Imaging molecular orbitals of pyridazine datively bonded on Ge(100) at room temperature 89

3.1 Introduction 89

3.2 Experimental and Computational details 91

3.3 Results and discussion 93

Chapter 4 Unique geometric and electronic structure of CO adsorbed on Ge(100): A DFT study 106

4.1 Introduction 106

4.2 Computational details 108

4.3 Results and discussion 111

4.3.1 Substrate geometries 111

4.3.2 Adsorbate configurations 114

4.3.3 Bonding analysis 118

4.3.4 Other possible adsorption structures 122

4.3.5 Adsorption and diffusion pathways 125

4.4 Conclusion 126

Chapter 5 Atomic processes of NO oxynitridation on Ge(100): a theoretical investigation 128

5.1 Introduction 128

5.2 Computational details 130

5.3 Results and discussion 132

5.3.1 Monomeric adsorption 132

5.3.1.1 Non-dissociative adsorption 132

5.3.1.2 Dissociative products 134

5.3.1.3 Dissociation from N12–O3 and N17–O 140

5.3.1.4 Dissociation from N1–O2 and N12–O2 144

5.3.2 Dimeric adsorption 146

5.4 Conclusion 150

Chapter 6 Conclusion **152**

6.1 Summary 152

6.2 Limitations and future work 154

References **156**

Summary

Study on adsorption of inorganic gas molecules and multifunctional heterocycles on Ge(100) is important to the application of Ge in microelectronics, molecular devices and catalysis. Advanced surface analytical techniques, including high resolution electron energy loss spectroscopy (HREELS) and scanning tunneling microscope (STM), together with density functional theory calculation (DFT) were used to investigate the reactions of pyridazine, CO and NO on Ge(100)-2×1.

Imaging orbitals of individual organic molecules by scanning tunneling microscope (STM) is critical in developing molecular devices. Orbital imaging on clean semiconductor surfaces is difficult to achieve due to the electronic coupling between adsorbed molecules and substrates. By preparing a sharp STM tungsten tip, orbitals of pyridazine molecule were clearly imaged on Ge(100). Two distinct features with three and four lobes were imaged by STM. They were identified as N-dative-B and NN-dative bonding configurations from an combinational study of orbital resolved STM images and STM image simulations. The assignment of the two bonding configurations were supported by theoretic simulations and the electron energy loss spectra. The results demonstrated that molecular orbitals on clean semiconductor surfaces can be resolved by STM, and the orbital resolved STM is capable of determining the complex surface chemistry of organic molecules on semiconductors.

The study of CO adsorption on semiconductor surfaces, particularly on Ge surfaces, is of great importance in catalysis and future microelectronics. CO adsorption on the Ge(100) surface was investigated using a slab model with density functional theory implemented in SIESTA. CO was found to be exclusively adsorbed on the asymmetric dimer

with C attaching on the lower Ge dimer atom. The adsorption process is barrierless. The calculated adsorption energy and vibration frequencies are comparable to previous experimental results. The crystal orbital Hamilton analysis showed that the bonding between Ge and CO is mainly attributable to the Ge $4p_z$ orbital overlapping with C 2s, or with CO molecular orbitals 3σ and 4σ. The repulsive energy between adsorbed CO molecules is less than 1 kcal/mol. The diffusion barrier of CO on the Ge(100) surface is about 14 kcal/mol.

Oxynitridation of Ge surfaces by nitric oxide (NO) is an important method to synthesize gate material for Ge-based complementary metal oxide semiconductor circuits. Understanding the atomic processes of NO oxynitridation on Ge(100) is highly desirable to optimize the N incorporating efficiency. Adsorption and dissociation of NO on Ge(100) were investigated on periodic models using DFT package CASTEP. Six nondissociative adsorption structures were found, and the O end of NO is almost inactive toward Ge(100). The nondissociative precursors can transform into various dissociative products, resulting in the lowering of system energy as well as the coordination numbers of N and O atoms. The transition state search indicates that the dissociation from interdimer precursors and the model with N insertion into a back bond are kinetically unfavorable with barriers around 1 eV. The intradimer adduct N1–O2 can dissociate to various N-2/3/4fold coordinated structures with most of barriers in between 0.2∼0.4. These barriers allow the dissociative processes to occur around 150 K, in agreement with the TPD experiments. The NO molecules can also dimerize first and react with the Ge surface when the dosing mount of NO is high. Only the cis-ONNO chains with two O atoms binding to Ge atoms can release N_2 molecules. These N_2 releasing processes are less exothermic than monomeric adsorption, thus can be suppressed by increase the temperature or decreasing the coverage of NO.

List of Tables

3.1 Vibrational frequencies (cm^{-1}) and their assignments for physisorbed and chemisorbed pyridazine on the Ge(100) surface. 105

4.1 Structural parameters of calculated c(4×2) and p(2×2) reconstructions of Ge(100). 113

4.2 Energies of 20 guessed adsorbing structures after geometric optimization. 114

4.3 Calculated structural parameters of CO adsorbed on Ge(100)-c(4×2). . 115

4.4 Adsorption and repulsive energy of CO molecules on Ge(100) surface at a coverage of 0.5. 117

5.1 Energies and bond lengths of non-dissociative NO adsorption products. . 136

5.2 Energy and bond lengths of dissociative NO adsorption products. 137

5.3 Estimated attempting frequencies (ν) of NO dissociative processes at different temperatures. 144

5.4 Bond lengths in optimized geometries of 20 proposed dimeric NO adsorption products.[a] 148

List of Figures

1.1 Ball and stick model of the Ge(100) surface. 5

1.2 Illustration of the surface reaction of ethylene with Ge(100)-2×1 leading to the formation of intradimer and interdimer products. 9

1.3 Three mechanisms of [2+2] cycloaddition of ethylene on Ge(100) dimer. . 14

1.4 Mechanism of organic molecules dissociation on Ge(100). 20

2.1 The energy level diagram of an STM tip and sample system with a bias. 44

2.2 STM working principle and set-up 46

2.3 The schematic diagram of high resolution electron energy loss spectroscopy system (LK3000). 59

2.4 The schematic illustration of specular and off-specular geometries in HREELS experimental methods. 60

2.5 LK3000 HREELS instrumentation. 62

2.6 Schematic diagram of the OMICRON VT STM. 65

2.7 Schematic diagram of the manipulator, sample heater stage with the electrical circuit connection for sample heating 66

2.8 The self-consistent field (SCF) procedure to solve the Kohn-Sham equation. 81

3.1 Constant current STM images of pyridazine adsorbed on a Ge(100) surface. 94

3.2 30×30 nm^2 STM images of pyridazine adsorbed on different terraces of Ge(100) with same orientation. 96

3.3 Theoretically predicted products and simulated STM images. 97

3.4 Simulated density of states (DOS) and orbitals of N-dative-B and NN-dative configurations. 102

3.5 HREELS spectra of pyridazine adsorbed on Ge(100) at liquid nitrogen temperature and 300K 103

4.1 Structural models of Ge(100) surfaces. 109

4.2 Eight possible adsorbing positions and four binding orientations of CO on the Ge(100)-c(4 × 2) surface. 111

4.3 Charge distributions on each layer of two slab models. 112

4.4 The stable structure of CO adsorbed on Ge(100)-c(4×2). 116

4.5 COHP curves of CO adsorbed on Ge(100)-c(4 × 2). 119

4.6 Molecular orbitals of CO. 120

4.7 Energy barriers of CO diffusing in different pathways. 124

4.8 the energy profile of CO adsorption versus C–Ge distance. 126

5.1 Possible adsorbing sites and orientations of NO on the Ge(100) surface. . 131

5.2 Possible configurations of NO dimers reacting on Ge(100). 132

5.3 Top and side views of stable structures of non-dissociative NO adsorption products on the Ge(100)-c(4×2) surface. 135

5.4 Structures of N-2fold dissociative products. 138

5.5 Structures of N-3fold and N-4fold dissociative products. 139

5.6 Energy variation of NO dissociation from N12–O3. 141

5.7 Energy variation of NO dissociation from N17–O. 142

5.8 Energy variation in elementary processes of NO dissociation from N1–O2. 143

5.9 Dimeric adsorption products of NO on the Ge(100) surface. 147

List of Publications

1. Unique geometric and electronic structure of CO adsorbed on Ge(100): A DFT study.

   He, J. H., Zhang, Y. P., Mao, W., Xu, G. Q. and Tok, E. S.

   Surface Science, **2012**, 606(9-10): 784-790.

2. Selective Attachment of 4-Bromostyrene on the Si(111)-(7×7) Surface.

   Zhang, Y. P., **He, J. H.**, Xu, G. Q. and Tok, E. S.

   Journal of Physical Chemistry C, **2011**, *115(31)*: 15496-15501.

3. Architecturing Covalently Bonded Organic Bilayers on the Si(111)-(7×7) Surface via in Situ Photoinduced Reaction.

   Zhang, Y. P., **He, J. H.**, and Xu, G. Q.

   Journal of Physical Chemistry C, **2012**, *116(16)*: 8943-8949.

4. Adsorption of O_2 and CO_2 on the Si(111)-7×7 surfaces.

   Shuai, Wang, **He, J. H.**, Zhang, Y. P., Xu G.Q.,

   Surface Science, **2012**, doi:10.1016/j.susc.2012.04.026.

5. Imaging molecular orbitals of pyridazine datively bonded on Ge(100) at room temperature

   He, J. H., Mao W., Zhang, Y. P., Wang, S., Xu, G. Q.,

   To be submitted.

6. Atomic processes of NO oxynitridation on Ge(100): a theoretical investigation

   He, J. H. Gao, J. K., Zhang, Y. P., Mao W., Xu, G. Q.

   In preparation.

7. Self-assembly of thiozole molecules on Ge(100) through double dative bonding.

   He, J. H. Mao W. Zhang, Y. P., Xu, G. Q.

   In preparation.

Chapter 1

Introduction

1.1 Motivation

Group IV semiconductor materials, including Si and Ge, play critical roles in modern technologies. Beside as the building material of integrated circuits in microelectronics, group IV semiconductors are also used in solar cells, microelectromechanical systems, chemical sensors and catalysts [1]. Si received much more fundamental and industrial attention because it dominates the microelectronics industry for more than 60 years. However, due to the limitation in Si-based microelectronics, relevant research focusing on Ge as an alternative of Si is shifting back. Meanwhile, Ge is also interesting to scientists due to wide applications in organic devices and catalysts.

The advantage of silicon over other semiconductors in microelectronics industry is owing to its native oxide (SiO_2), which serves to passivate the silicon and form a defect-free interface between Si and SiO_2. This naturally formed defect-free interface between Si and SiO_2 is critical to the transistors, as electrical properties of the device heavily rely on the quality of this interface. Microelectronics industry on Si-based integrated circuits has been rapidly growing for more than 60 years. The calculation speed as well as the number of transistors on an integrated circuit has been doubling approximately every two years. This rapid progression was predicted by the famous Moore's Law [2]. The scaling has been achieved by shrinking the dimension of transistors, including the thickness of dielectric SiO_2 layer . The dielectric layer was thinner than 1 nm in 32 nm

technology in 2010 [3]. For such thickness, leakage current due to tunneling effect through the dielectric layer is significant and becomes the main obstacle to the development of Si-based integrated circuit technologies. One solution of these technologies is to find an alternative dielectric material (also known as high-κ material) to reduce the leakage current. Once the dielectric layer is no longer restricted to SiO_2, other semiconductors such as Ge or GaAs become attractive. In fact, Ge used to be the material of the first transistor in microelectronics history. Ge has faster carrier mobility than Si, and some Ge based materials show better dielectric properties than that of silicon. The lower melting point of Ge also allows the fabrication at a lower temperature and easy treatment. Now, these advantages make Ge a shifting back as a promising candidate for next generation of semiconductors.

However, the main drawback to hinder the wide applications of Ge is the poor chemical stability of its native oxide layer towards atmosphere and water [4]. The noncompact structure of GeO_2 also allowed facile removal of the interface, and the external corrosives are also penetrable to inner semiconductor layer. In addition, GeO_2 forms a poor interface with Ge with high density of electronic defects, which deteriorate the device performance. Thus, an effective passivation technique of germanium surfaces is essential to the application of germanium in microelectronics industry. Reacting Ge surfaces with organic molecules or inorganic gas molecules is a possible method to offer a defect free interface with the dielectric layer.

Beside the passivation of Ge surfaces, reactions of organic molecules on Ge surfaces are also important in the fabrication of organic devices. By growing organic molecules on semiconductor surfaces with tunable properties such as size, shape, binding/space configurations, flexibility, hydrophobicity, chemical reactivities and conductivity, the de-

signed semiconductor devices show novel functionalities in the fields of optical, electronic, mechanical as well as chemical and biological applications. Extensive research has been focusing on organic functionalization of silicon surfaces, and their results provided an atomic understanding of surface chemistry of silicon surfaces. Such an understanding is necessary for incorporating molecular devices into silicon semiconductor technologies. Analogously, the study of organic molecules reacting with germanium surfaces is also highly important due to the potential coupling of molecular properties with germanium based semiconductor technologies.

Reactivities of inorganic gas molecules towards Ge surfaces are not only interesting for finding an effective passivation method of Ge, but also important in catalysis. Ge is considered as an additive in many metal-metal oxide catalysts used in selective oxidation of carbon monoxide, nitrogen oxide and other hydrogen carbon compounds. The germanium was reported to stabilize the transition metal clusters in catalysis and enhance the selectivity during reactions [5–10]. However, the reactivity of germanium itself toward those reactant gas molecules is yet to be discovered. Thus, the study of inorganic gas molecules on germanium surfaces is also important to understand the role of Ge in the catalatic process. It will offer useful information for the future development and design of Ge-containing catalysts.

Due to the importance in microelectronics, organic devices and catalysis, reactions of organic molecules and inorganic gas molecules on Ge surfaces will be introduced in details in following sections. The reconstructions of Ge(100) will be introduced firstly because of its technical importance. Then the reactions of organic molecules on Ge(100) will be reviewed in Section 1.3. The gas molecules reactions on Ge(100) are to be described in Section 1.4. Finally, Section 1.6 presents the objectives and scope of this thesis.

1.2 Ge(100) and its surface reconstruction

1.2.1 Dimer reconstruction of Ge(100)

Ge crystalizes in a diamond like structure in the same way as Si, except that the lattice constant (5.658Å) is 4% larger than Si (5.432Å). The electronic configuration of Ge is $1s^2 2s^2 2p^6 3s^2 3p^6 4d^{10} 4s^2 4p^2$, which has the same shell electronic configuration as C and Si. The 4s and three 4p shell orbitals are mixed linearly to produce four hybrid sp^3 orbitals. Four shell electrons fill in these hybrid orbitals, forming covalent bonds with four nearest neighboring Ge atoms in a tetrahedral configuration. When the lattice of Ge is cut along one of the geometrically equivalent planes: (100), (010) and (100), each surface Ge atom will be left with two broken bonds, namely dangling bonds with unpaired electrons of high energy. To minimize the surface energy, the surface atoms reconstruct to eliminate the dangling bonds as much as possible. Many models were proposed for the surface reconstruction of Si(100) and Ge(100). They are Haneman's raised row, [11] Phillips' missing row, [12] Harrison's missing row, [13] Seiwatz's conjugated chain, [14] Northrup's dimer chain and π-bonded defect model [15]. Finally, the dimerization model suggested by Schlier and Farnsworth [16] was widely accepted after Tromp et al. [17]and Hamers et al. [18] directly imaged the surface dimers by scanning tunneling microscopy (STM) in the 1980s. In this model, two neighboring surface Ge atoms along the dangling bond orientation dimerize via σ and π bonds, resulting a (2×1) reconstruction (Figure 1.1). The dimers align together to form the dimer rows in the same layer.

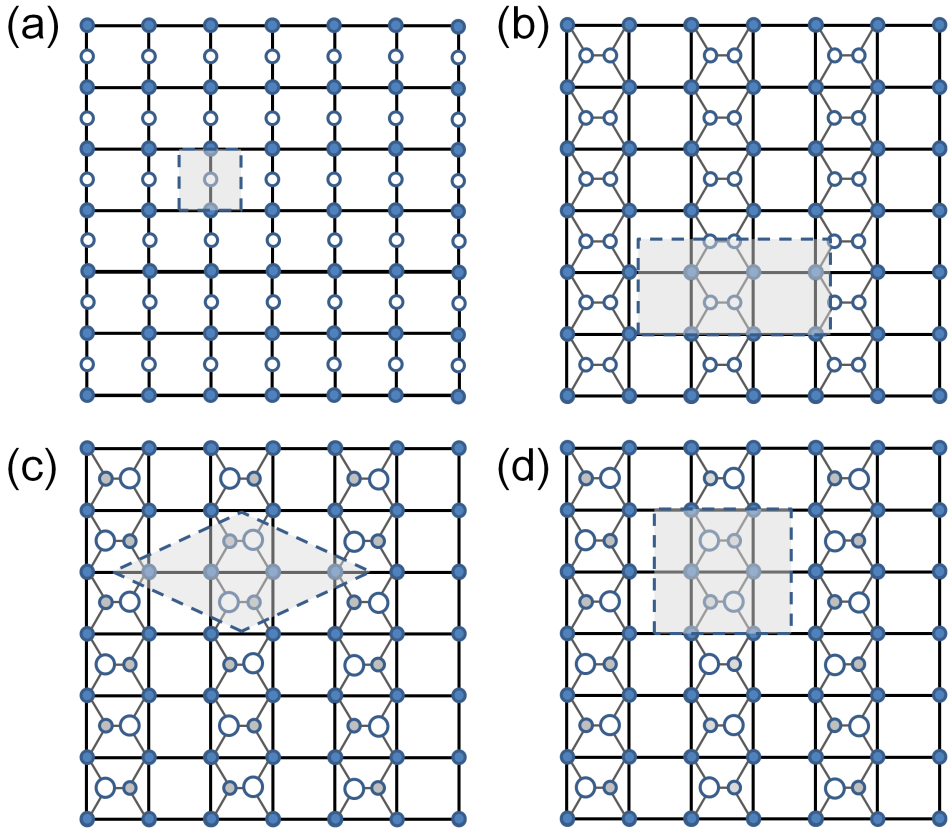

Figure 1.1: Ball and stick model of the Ge(100) surface. (a) (1×1); (b) p(2×1) dimer reconstruction; (c) c(4×2) dimer reconstruction; (d) p(2×2) dimer reconstruction. The shaded area refers to the primary unit cell for each reconstruction.

1.2.2 Buckling of dimers

The original idea of dimerization was that the two surface atoms form a symmetric dimer with the dimer bond totally parallel to the surface plane. However, Tromp et al. [17] and Hamers et al. [18] observed both symmetric and asymmetric dimers. The existence of asymmetric (buckled) dimers had been predicted by Chadi in 1979 [19]. Chadi performed a tight-binding calculation to optimize the dimerized surface without any symmetry constraints and found that the symmetric dimer is energetic unstable. The instability of unbuckled dimer towards buckled one was further confirmed by the calculations with a higher accuracy. The buckling energy of Ge, defined by the energy gain due to buckling a symmetric dimer was evaluated to be around 0.26 eV [20]. Although, the experimental STM results seemingly contradicted the theoretical prediction as both asymmetric and symmetric dimers appeare in STM images in close ratio, indicating these two configurations are roughly equal in energy. However, after several years' study, it was realized that the symmetric appearing dimers in STM image are actually asymmetric dimers with fast switching buckling directions.

1.2.3 Higher order reconstructions

The charge transfer between the lower and upper dimer atoms results in an array of dipoles on the Ge(100) surface. The neighboring dimers within a dimer row always buckle in opposite directions due to the repulsive dipole interaction. Two neighboring dimer rows may have in-phase and out-of-phase buckling directions, leading to two higher order reconstructions: p(2×2) and c(4 × 2), as shown in Figure 1.1. The DFT calculations showed that these two reconstructions have nearly equivalent energies. Although c(4×2) is slightly favorable, the two reconstructions are always simultaneously imaged by STM.

In addition, the transition between them can be triggered by applying a higher bias of the STM tips during scanning. This technique has been used to "write" on Ge(100), showing its potential application in nanodevices and information storage. As these three phases are indistinguishable in most other spectra, such as HREELS, IRAIS, XPS, the clean Ge(100) surface can be simply described by Ge(100)-2×1 regardless the dimer buckling.

1.3 Reaction mechanisms of organic molecules on Ge(100)

Functionalization of the Ge(100) surface for passivation or fabrication of molecular devices needs a good understanding of reaction mechanisms of organic functional groups on Ge(100). The π bonding and zwitterionic properties of Ge(100) buckled dimers grant the diversity of reaction pathways of organic molecules. Several reaction mechanisms including [4+2] cycloaddition, [2+2] cycloaddition, dative bonding and dissociation will be discussed in the following subsections.

1.3.1 Cycloadditions

Cycloadditions are a class of pericyclic reactions widely used in organic synthesis. Two unsaturated molecules with π bonds or conjugated π orbitals approach each other, the π bond of one molecules at the approaching site breaks or recombines to form new σ bonding with the other molecule, producing a new cyclic molecule. The reactions are named after its involved π electrons, like [2+2], [4+2] or [6+2]. On the Ge(100) surface, the Ge dimer serves as a double bond, accepting one double bond or conjugated double bonds to undergo [2+2] or [4+2] cycloaddition.

1.3.1.1 [2+2] cycloadditions

The reaction of ethylene on Ge(100) is an interesting case study of [2+2] cycloaddition because ethylene is the simplest alkene molecule. Using IR spectroscopy, Lai et al. [21] observed that the double bond of ethylene breaks and two new σ bonds to Ge atoms form. In addition, their TPD data showed that two major molecular desorption peaks, which are assigned to two binding states of ethylene on Ge(100). Another group attributed these two peaks to the adsorption terraces and at step edges rather [22]. Later, the STM results from Kim's group clearly showed two [2+2] adsorption features on the Ge(100) [23, 24]. One is assigned to ethylene binding on the single dimer, namely intradimer adduct; the other one, namely interdimer one, is the ethylene binding on a paired end-bridge between two neighboring Ge dimers within a dimer row (Figure 1.2). They also found that the interdimer adduct always appears in a paired configuration with another interdimer adduct, to fully eliminate the unreacted dangling bonds. The intradimer and interdimer adducts can be selectively desorbed by applying different pulsed biases to STM tip [25]. This selectivity has the potential application in nanoscale lithography. Beside the experimental studies, theoretical calculations were also carried out to investigate the ethylene adsorption on Ge(100) [26–29]. The total energies of these two configurations calculated by Lu et al. [26] suggested that the intradimer binding is thermodynamically favorable over the interdimer adduct. Fan et al. reinvestigated the adsorption configuration [27, 29], and found that the stability of intradimer and interdimer is temperature and coverage dependent. Their calculations showed that the paired interdimer structure is the most stable under low temperature, whereas at high temperature both intradimer and interdimer products are favourable. The lower coverage thermodynamically favors the intradimer adduct, whereas at coverage of 1, the interdimer product is both thermodynamically and kinetically favorable.

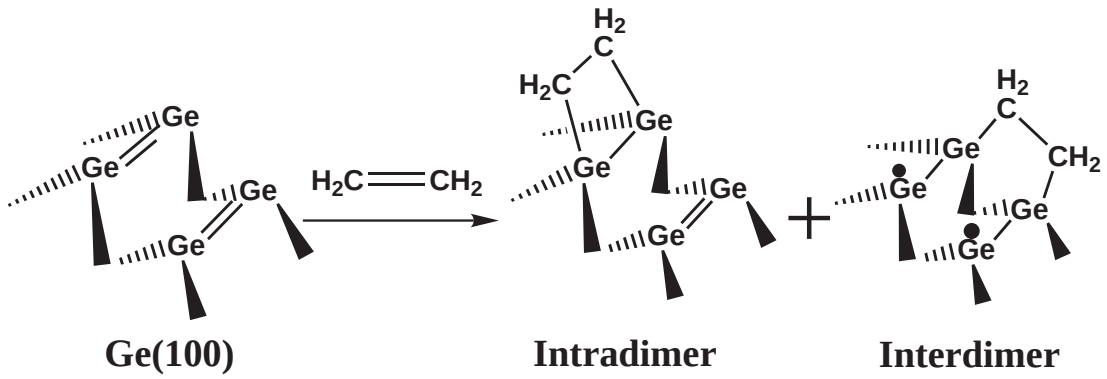

Figure 1.2: Illustration of the surface reaction of ethylene with Ge(100)-2×1 leading to the formation of intradimer and interdimer products.

Beside ethylene, cyclopentene [30–33], cyclohexene [31], 1,5-cycloocatadiene [30, 34], Norbornadiene [35] and styrene [36–39] have also been studied with PES, IR, STM, TPD as well as theoretical calculations. These alkenes of isolated double bond react under the similar pathway as ethylene, producing the [2+2] interdimer or intradimer adduct. If the adsorbed alkene is asymmetrically substituted, for example styrene, the interdimer adduct further splits to trans- and cis configurations regarding the arrangement of the phenyl ring [36]. In addition, the α carbon of styrene also turns to be a chiral center due to the formation of Ge-C bond. This shows the possibility of using achiral molecules on achiral surfaces to create chiral patterns.

Acetylene, with a triple bond, has a circuitous researching history of reaction on Ge(100). Kim et al. first observed two adsorption features of acetylene on Ge(100) using STM and TPD techniques [40]. The authors assigned the two features to di-σ (intradimer) and tetra-σ adducts. The di-σ adduct is slightly energetically favorable than the tetra-σ binding according to the theoretical calculation by Miotto et al. [41] and Cho et al. [42]. The assigned tetra-σ adduct, however, was reinterpreted as the interdimer adduct involving one double bond [42]. The new interpretation is supported by recent

detailed STM image simulations [43] and Ultraviolet photoelectron spectroscopy (UPS) [44].

Unsaturated organic molecules containing isolated C=O, C=N or C=S bonds also react with Ge(100)-2×1 via a similar [2+2] cycloaddition. Loscutoff et al. studied reactions of isocyanates (R-N=C=O) on Ge(100). The [2+2] cycloaddition of C=N bonds is the minor reaction path way in addition to the major dissociation of R-C bonds [45]. In contrast, for isothiocyanates (R-N=C=S), the authors found that [2+2] cycloaddition of C=S and C=N dominates the reaction, with a higher reactivity of C=S over C=N [46]. However, nitriles (R-C≡N) including acetonitrile, 2-propenenitrile, 3-butenenitrile and benzonitrile on Ge(100) do not react through the [2+2] cycloadditions at room temperature [47–49]. The DFT calculation showed that the energy gaining from formation of weak Ge-C and Ge-N bonds cannot compensate the energy cost for the C≡N bonds cleavage [47]. Aldehydes like formaldehyde were theoretically predicted to undergo the [2+2] cycloaddition via their C=O bonds with Ge dimers. [50] However, the IR measurement failed to find a conclusive evidence. [50] Ketones such as acetone do not react in a [2+2] cycloaddition. Instead, they undergo an ene-like reaction, which will be discussed in section 1.3.3.

1.3.1.2 [4+2] cycloadditions

Intensive studies have been focused on the reactions of dienes on Ge(100). Teplyakov et al. found that both 1,3-butadiene and 2,3-dimethyl-1,3-butadiene react with the Ge dimer to form [4+2] adducts [51]. However, in contrast to the irreversible [4+2] cycloadditions on Si(100), retro-Diels-Alder reactions which molecularly desorb dienes were observed when temperature rises. This is owing to the weak Ge-C bonding, demonstrated by Mui et al. with ab initio calculations [52].

Lee et al. found that other cyclic dienes like 1,3-cyclohexadiene [53, 54], also adsorb on Ge(100) via the exclusive [4+2] cycloaddition pathway using UPS and HREELS and TPD. In addition, Lu et al. predicted by calculations that diynes such as diacetylene may bind to Ge(100) via [4+2] and [2+2] cycloadditions [55]. The [4+2] product is a six-membered cyclic cumulene, which is scarcely reported on semiconductor surface. Bent's group found that the nitriles with conjugated C=C bonds like 2-propenenitrile mainly react with Ge(100) via a [4+2] mechanism [47, 48]. They also demonstrated that conjugated ketones, e.g. ethyl vinyl ketone (EVK) and 2-cyclohexen-1-one undergo a [4+2] process on Ge(100), in contrast to ene-like and C=O [2+2] cycloaddition on Si(100) [56].

Although aromatics have conjugated double bonds, the additions of aromatics on Ge(100) are energetic unfavorable due to the loss of resonance energies of aromatic rings. Nevertheless, the [4+2] cycloaddition of benzene is able to occur on Ge(100).

Benzene adsorbs on Ge(100) in a [4+2] cycloaddition mechanism, although the reaction is less exothermic than that of on Si(100). Fink et al. [57] found benzene adsorbs on a Ge dimer in a flat lying configuration via di-σ bonds based on angle-resolved ultraviolet photoemission spectroscopy (ARUPS). The TPD data showed two desorption peaks of benzene adsorbed on Ge(100) around 230 K and 250 K, which are remarkable lower than that of Si(100): 311 K and 369 K respectively. The much lower desorption temperature indicates that the adsorption of benzene on Ge(100) is quite weaker than that on Si(100), consistent with the case of [2+2] cycloadditions [57]. Valence band photoemission studies by Kadodwala and DFT calculations by Cho et al. also proved that benzene adsorbs on Ge(100) via a similar but weaker [4+2] cycloaddition compared to that on Si(100) [49, 58].

Conclusively, many conjugated unsaturated molecules undergo [4+2] cycloadditions on Ge(100). However, due to the weaker Ge-C bonding than Si-C, most of those [4+2] reactions are reversible, and the adsorbed molecules can desorb via a retro-Dies-Alder reaction at higher temperatures. The reversible adsorption makes the Ge(100) highly selective towards unsaturated molecules. The selectivity can be seen from the absolute priority of [4+2] over [2+2] from the reaction of 1,3-butadiene [52, 53, 59], 2-propenenitrile [47,48] and EVK [56] on Ge(100), whereas both [4+2] and [2+2] pathways are comparable in ratio on Si(100). This high selectivity suggests that Ge may be a superior semiconductor material for selective fabrication of organic compounds in application of molecular devices.

1.3.1.3 The mechanism of cycloadditions

Although a huge number of cycloadditions have been observed for unsaturated organic molecules on Ge and Si surfaces, their mechanisms are still in debate. Currently, there are three pathways proposed for the cycloadditions on Ge(100) surfaces: a stepwise pathway via a biradical intermediate, a stepwise reaction via a π complex precursor and a concerted mechanism.

The concerted mechanism for cycloadditions of organic molecules had been elucidated by Woodward and Hoffmann [60]. Based on their rule, in cycloadditions, the reacting wave functions (frontier orbitals) of two unsaturated molecules (occupied π for one molecule and unoccupied π^* for the other or vice versa) must match in symmetry, otherwise the reaction is forbidden. For two alkene molecules both in electronically ground state, the frontier orbitals π and π^* are always mismatched. Thus [2+2] cycloadditions are symmetry forbidden if they follow a concerted way under thermal excitation. In contrast, the [4+2] is symmetry allowed.

Based on the analogies between the Ge dimer and C=C, one would expect the Ge dimer react as the dienophile toward organic dienes in a [4+2] cycloaddition. Experimental study confirmed that a six member ring consisting of two Ge atoms from the Ge dimer and four carbon atom is produced after adsorption of butadiene or its derivatives on Ge(100) [51]. However, the symmetry-forbidden [2+2] cycloaddition also surprisingly occurs for other dienes and alkenes. Since the traditional [2+2] concerted cycloaddition mechanism cannot explain the facile [2+2] cycloadditions on Si(100) and Ge(100), a stepwise pathway involving a biradical intermediate was proposed [26, 32, 61–63]. As shown in Figure 1.3, the stepwise pathway starts with the π bond approaching the electrophilic (lower) Ge atom. Then the C-C π bond breaks and forms an intermediate in which the α carbon links to lower Ge atom, β carbon converts to the radical. In a second step, the β carbon radical binds to the left (upper) Ge atom, producing a four member ring. The two steps occur with small barriers, which explain the facile addition of double bonds on Ge(100). However, there remain strong evidences that cannot be explained by this stepwise biradical mechanism. For example, the [2+2] cycloadditions of trans- and cis-butadiene on Si(100) surfaces show high degree of stereo-selectivity. But any biradical intermediate mechanism would facilitate the rotation of the stereochemistry-defining αC-βC bond, quenching the stereo-selectivity. To explain such a high stereo-selectivity, a second mechanism assumes that an additional C-Ge bond forms and locks the rotation of αC-βC in the above intermediate, namely π-complex precursor. Although Nagao et al. detected the π complex of ethylene on Si(100) using HREELS, their DFT calculation failed to prove the stability of such an intermediate [64]. In addition, the π complex mechanism cannot explain another unexpected aspect of [2+2] cycloaddition on Si(100). The initial sticking coefficient of the adsorbate at lower coverage is near to 1, but the molecules failed to reach a coverage of 1 as the sticking probability drops dramatically

when the coverage is large than 0.5. Examples include large (1,3-cyclohexadiene [65] and 1,5 cyclooctadiene [66]) and small molecules (ethylene [67, 68, 68, 69]). Therefore the decrease in sticking probability cannot simply be explained in adsorbate mutual repulsion, as the adsorption energies do not vary significantly as a function of coverage [70, 71]. The above evidences seem to be also consistent with the π complex mechanism.

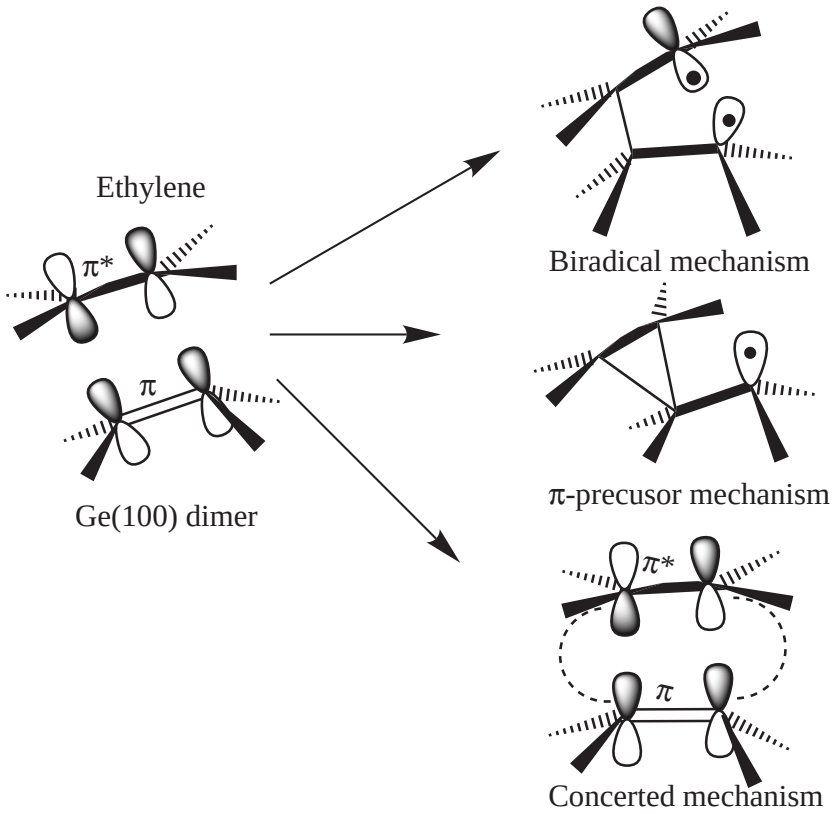

Figure 1.3: Three mechanisms of [2+2] cycloaddition of ethylene on Ge(100) dimer.

A new frontier orbital description of Si(100) was proposed by Ryan et al. to reinterpret the [2+2] addition in a concerted way [72]. Two Si $3p_z$ atomic orbitals in a dimer interact in phase and out of phase, forming π and π^* orbitals. In ethylene (or other organic molecules with double bonds), p orbitals compose the π and π^* in the same way. Thus all π orbitals in double bonds have the same symmetry, and are different from

those π^* orbitals. Woodward-Hoffmann rule requires that the HOME (pi)orbital of one molecule interact with LUMO (π^*) orbital of the other molecule. Therefore, a [2+2] cycloaddition based on HUMO(π)-LUMO(π^*) interaction is symmetry forbidden. Ryan et al. demonstrated that the above Woodward-Hoffmann rule is still valid to the surface cycloadditions. However, the frontier orbitals of surfaces should be described in the term of surface electronic states, namely the crystal wavefunctions (orbitals).

In an view of crystal orbitals, each Si $2p_z$ on the Si(100)-2×1 surface directly interacts with all neighboring orbitals differing in a phase factor $e^{i\vec{k}\vec{r}}$. The face factor $e^{i\vec{k}\vec{r}}$ is determined by separation of two orbitals $\vec{r}$ at different $\vec{k}$ points according to Bloch's theorem. Some occupied crystal orbitals (HOMO) at special $\vec{k}$ points have Si p_z orbitals in opposite phases on neighboring dimers. The symmetry of these orbital matches ethylene's π^* if the molecule undergoes interdimer cycloaddition. Further analysis on asymmetric reconstructions—c(4×2) and p(2×2) demonstrated that several crystal orbitals consist of two Si $2p_z$ of one dimer in opposite phases, which are responsible for the intra-dimer [4+2] cycloaddition. Using this technique, the authors successfully interpreted the endo and exo end-bridge products of 1,3-cylcohexadiene molecules reacting with Si(100) [73].

To date, the above rationalizations have only applied to the cycloadditions on Si(100) surfaces. Due to the similarities between Ge(100) and Si(100) in their structures, one would expect that the concerted cycloadditions on Ge(100) are also symmetry-allowed. Of course, more theoretical and experimental studies of the reaction mechanism of cycloadditions on Ge(100) are of high interest.

1.3.2 Dative bonding

Due to the zwitterionic property of asymmetric dimers, Ge(100) can serve as the electron donor or the acceptor in dative bonding with Lewis acids/bases.

1.3.2.1 Dative bonding of Lewis acids: Ge→B, Ge→Al

The upper dimer Ge atom is of negative charge, thus favors donating electrons to Lewis acids like BH_3 and $AlCl_3$. DFT calculations predicted that although BH_3 dissociates on Ge(100) dimers to form BH_2 and H species, strong interaction still exists between the as-formed BH_2 and H adspecies [74]. The interaction between B and Ge can be considered as the dative bonding. The adsorption of $AlCl_3$ was studied using STM and high-resolution core-level photoemission spectroscopy (HRCLPES) [75]. $AlCl_3$ was found to react with the Ge dimer via a "[2+2]" cycloaddition, which forms Ge-Cl and Ge-$AlCl_2$ without breaking any Al-Cl bond. This cycloaddition, differing from the alkene cycloaddition which involving π bonds, is driven by formation of two dative bonds: Ge(upper)→Al and Cl→Ge(lower).

1.3.2.2 Dative bonding of Lewis bases: N→Ge

The electronically positive lower dimer atom is able to accept lone electron pairs from N, P, S or O containing molecules, including NH_3, PH_3, hetero-aromatics. Bater et al. found that NH_3 molecularly adsorbs on Ge(100) at room temperature, and reversibly desorbs from Ge surfaces under thermal treatment [76, 77]. Mui et al. demonstrated via DFT calculation that NH_3 adsorbs on Ge(100) dimers via N→Ge bonds. Their calculation also indicated that the subsequent dissociation of N-H bond as well as insertion of

N into Ge-Ge bond are of high barriers, which is consistent with previous experimental results. N→Ge bonds were also observed in the adsorption of other alphatic amines like ethylamine [78, 79], allyamine [78–80], ethylenediamine [81], N,N-dimethylformamide, N,N-dimethylformamide-d7, 1-methyl-2-pyrrolidinone, N-methylcaprolactam [82], formamide, N-methylformamide, N-methylacetamide, N,N-dimethylacetamide [83], pyrrolidine [84], 3-pyrroline [84]. These molecules undergo subsequent dissociation of N-H bond when temperature rises. N-dative bonding is also one of reaction channels of amino acids reacting with Ge(100). Examples include alanine [85], arginine [85], serine [86], methionine [87], leucine [88], glycine [89, 90], histidine [91], valine [92] and S-proline [93].

Many heteroaromatics form dative bonds on Ge(100) without breaking the aromatic rings to reserve the resonance energies. Pyridine is a six member ring with one sp^2 N atom. Cho et al. found that pyridine adsorbs on the low dimer atom of Ge(100) via a N→Ge bond, forming a perfect c(4 × 2) pattern. The total energy calculations from two groups showed that dative bonding is the most thermodynamically favorable among all possible bonding manners [94, 95]. Kim et al. also demonstrated that the dative bonding on Ge(100) is the final stable state, different from the case on Si(100), where dative bonding is only an intermediate state [95]. The extra stability of dative bonding is attributable to the weaker Ge-C bond than Si-C, which make the conversion of N-dative bonding to any other Ge-C bonded structure (thus of high energy) unfavorable.

If multiple heteroatoms are contained in a molecule, it is possible that multiple dative bonds form between the molecule and Ge(100). Pyrimidine contains two N atoms, and it forms double dative bonds to two lower atoms of the neighboring Ge(100) dimers without loss of aromaticity [96]. The STM result showed c(4 × 2) patterns of oval protrusions, which are the pyrimidine rings tilted on every other dimer by 40° with respect to the

surface plane. Under continuous exposure, the c(4 × 2) patterns transit to p(2 × 2) with pyrimidine occupying every dimer and being imaged as the zig-zag chains in STM. Once the dosing stops, the p(2 × 2) releases back to c(4 × 2) due to large repulsion between adsorbed pyrimidine molecules. In addition to double dative bonding, purine which contains three N atoms, was reported to adsorb on Ge(100) in a compacted p(2×2) structure via the triple dative bonding [97].

1.3.2.3 Dative bonding of Lewis bases: S→Ge

Thiophene was first reported to undergo a [4+2] cycloaddition on Ge(100) from valance band photoemission spectra [49,98]. Then Jeon et al. detected other two reaction mechanisms using STM, HRPES and DFT calculations [99–101]. One of them is thiophene binding to the lower dimer atom via S→Ge. At a coverage of 0.25 monolayer, the datively bonded thiophene form one-dimensional molecular chains on Ge(100) [102–104].

Methionine is an amino acid with methylthiomethyl, amido and carboxyl groups. This molecule adsorbs on Ge(100) in two models: "O-H dissocited-N-dative-S-dative-bonded" [87] and "O-H dissociated-S-dative-bonded" structures. The S-dative bonding involves in both configurations, suggesting its important role in the attachment of S-containing molecules on Ge(100).

1.3.2.4 Dative bonding of Lewis bases: O→Ge

Oxygen dative bonding on Ge(100) was scarcely reported. O→Ge appearers in the precursor state in the stepwise reaction during dissociative processes, such as in the reaction of propylene oxide [61] and H_2O [105]. Acetone was also reported to datively bond to Ge(100) under 115 K, and the binding energy is as low as 12 kcal/mol [106].

The O→Ge bond energy was found to be weaker than S→Ge bond by 5.9 kcal/mol [107]. Kachian et al. reported that during adsorption of glycine, only N→Ge but not O→Ge forms [90].

Dative bonding is a wide class of surface reactions. Formation of dative bonds is often barrierless. Thus the dative bonding facilely occurs under low temperature with a higher stick probability, which grantee the capability of creating ordered patterns. The stability of dative bonding is in the order of N→Ge>S→Ge>O→Ge, attributable to the different dative bond energy [108]. The electronic properties of adsorbed molecules are not strongly disturbed by the dative bonding, in contrast to the cycloadditions, where the π bonds of adsorbates break. These advantages grantee the possibility of fabrication of organic molecules with high coverage, ordered pattern and controllable geometric and electronic structures. When the temperature increases, the dative bonding may transfer to other thermodynamic stable cycloaddition or dissociative bonding [102, 109].

1.3.3 Dissociation

Organic molecules of X-H bonds (X=O, S, N) are facile to dissociate on Ge(100). Most of dissociative processes start from the lone pair of electrons on X donating to the electrophilic lower dimer atom, forming the dative bonding precursor (in Figure 1.4). A four member ring consisting of two Ge dimer atoms (intradimer or interdimer), H and X appears as the transition state when the H atom approaches the upper dimer atom. Finally the X-H bond breaks, and the new Ge-H bond forms simultaneously as well as the X→Ge dative-bond converts to the covalent bond.

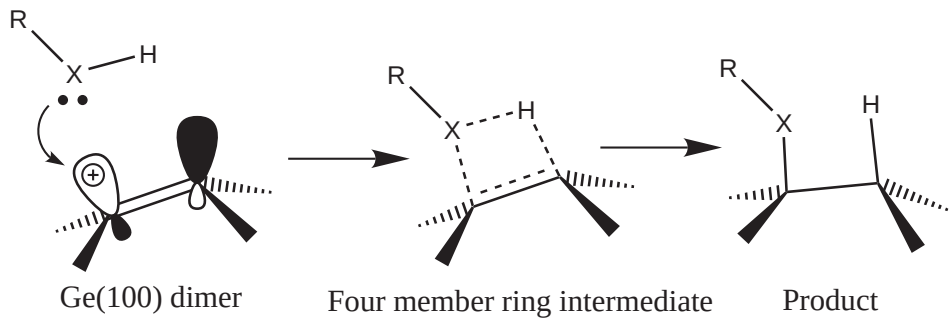

Figure 1.4: Mechanism of organic molecules dissociation on Ge(100). X=O, S, N.

1.3.3.1 N-H dissociation

Dissociation of N-H bonds on Ge surfaces has attracted much attention because the simultaneous formation of Ge-N bond is important in the synthesis of germanium nitride, which is used as the dielectric gate and diffusion barrier in microelectronics. NH_3 molecules do not dissociate on Ge(100) because the desorption barrier is much lower than the dissociative barrier as we mentioned in Subsection 1.3.2.2. When the hydrogen atoms in NH_3 are substituted by alkyl groups, the electron donating effect of alkyl groups makes the N atom more electronically negative. Thus the dative bond is enhanced. The increased stability of dative bonding depresses the desorption rate and promotes the dissociation rate indirectly. Thus primary and secondary amines readily undergo dissociation of N-H bond on Ge(100) at room temperature, although most of them form dative bonds at low temperature or coverage similar to NH_3. Examples include ethylamine [78, 79], allyamine [78–80], ethylenediamine [81], N,N-dimethylformamide, N,N-dimethylformamide-d7, 1-methyl-2-pyrrolidinone, N-methylcaprolactam [82], formamide, N-methylformamide, N-methylacetamide, N,N-dimethylacetamide [83], pyrrolidine [84] 3-pyrroline [84]. Tertiary amines are physisorbed on Ge(100), indicating that the Ge-C bond is too strong to be cleaved [82, 83].

The N-H bond of pyrrole dissociates via a different intermediate rather than dative bonding precursor [110–112]. Because the lone electron pair of N atom is delocalized on the aromatic ring, the N→Ge is weaker than that of aliphatic amines. Instead, the neighboring carbon binds to Ge atom, and the H atom from the N-H group approaches another Ge atom, forming a five member ring transition state [84]. This α-carbon dative bonding mechanism of N-H dissociation has been demonstrated on the Si(111) surface by DFT calculations [113].

1.3.3.2 O-H dissociation

Water is the simplest molecule containing O-H bonds. Papagno et al. observed the adsorption of water on Ge(100) at different temperatures using HREELS [114]. Water does not directly adsorb on Ge(100) at room temperature. At 100 K, it mainly adsorbes in a molecular state as well as a minor dissociative state. However, the adsorbed water molecules at 100 K dissociate completely to Ge-H and Ge-OH moieties when the surface temperature rises up to 300 K. Papagno et al. further demonstrated that when the temperature is higher than 450 K, the Ge-OH begins to decompose. Larsson and Flodstroem obtained similar results using valence band photoemission spectroscopy [115–117]. The DFT calculations conducted by Cho et al. found a dissociation barrier for water molecules of 0.49 eV, higher than the desorption barrier 0.33 eV [118]. Foeraker and Doren performed similar simulations and found the presence of an activation barrier in dissociation of water on Ge surfaces [119]. These barriers are different from the case on Si(100), where water dissociates at very low temperatures due to a small barrier of 0.15 eV [120, 121].

Beside water, other simple alcohols like methanol [122–124], ethanol [125], ally alcohol [126] were also investigated and found to undergo O-H dissociative reactions on Ge

surfaces. Carboxylic acids also cleave their O-H bonds to form new Ge-H bonds. The carboxylate moieties bind to the surface with one oxygen atom or two oxygen atoms, forming the monodentate or bidentate structure [127, 128]. The bidentate structure has two types: end-bridge(interdimer) and on-top(intradimer). The monodentate and two bidentate structures have been both identified by STM, in agreement with the theoretical calculations performed by Kim et al [129].

1.3.3.3 S-H dissociation

H_2S is used to effectively passivate the interface between Ge and the gate dielectrics in Ge-based CMOS [130]. Teng et al. observed that the dissociation of S-H bond readily occurs at 110 K , in contrast to molecular adsorption of water at this temperature [131]. The calculations showed that H_2S dissociates with a negligible barrier (0.02 eV) compared to the larger barrier (0.28 eV) for H_2O dissociation. The much smaller barrier originates from the weaker S-H bonds than O-H as well as the stronger S-Ge bond than O-Ge. Kachian and Bent proved that S-H dissociation is both kinetically and thermodynamically favored over O-H dissociation [107]. In addition, the substitution of bulky groups increases the strength of S→Ge bond, further promoting the dissociation. Ethanethiol [107, 125], 1-octadecanethiolate [132–134], phenylthiol [134] undergo the similar S-H bond dissociations. Due to the strong S-Ge bond, Ge-S-H moiety further decomposes into Ge-S-Ge and H_2 when temperature increases [135].

1.3.3.4 C-H dissociation: ene-like reaction

Beside dissociations of N-H, S-H and O-H bonds, the ene-like reactions involving cleavage of αC-H bond of some highly polar function groups were also found on Ge(100). Wang and Bent firstly reported the ene-like reaction of acetone on the Ge(100)-2×1 sur-

face at room temperature [106]. The increased acidity of αC-H induced by the highly polarized $^{\delta+}C =^{\delta-} O$ group allows the abstraction of α-H by upper dimer atom. Similarly, the strong electronic drawing ability of αN-H of imine group also promotes the cleavage of α-H, which was predicted for arginine by Ardalan et al [85].

Kachian et al. rationalized the dissociation trends of X-H (X=O, N, S) in a thermodynamical view by considering the changes in bond energies obtained in DFT calculations [108]. The S-H dissociation is ∼7 kcal/mol more exothermic than the corresponding O-H cleavage, due to the weakness of S-H bonds relative to O-H bonds. As the smaller Pauling electronegativity of N (3.04) than O (3.44), N can donate electrons more effectively to form dative bond than O. Thus N→Ge bonds are S-H, N-H and O-H (related to the unreacted system) dissociations differ by less than 2 kcal/mol, extra stability of N-Ge dative bonding precursor over O-Ge one makes the dissociation of O-H via dative state thermodynamically favored. In short, a dissociation sequence of X-H on Ge(100) surface is S-H > O-H > N-H.

1.3.4 Reactions of multifunctional molecules

After the basic principles of monofunctional organic molecules reactions on Ge(100) were well established, further interests were extended to reactions of multifunction molecules. The fabrication of multifuctional molecular layers requires anchoring the molecules to semiconductor surfaces by selectively binding to Ge surfaces with some function group(s), leaving other groups intact. These groups can further react with monolayers of external molecules, forming a second layer. This technique is called layer-by-layer growth, which has been proved to be an effective passivation method [136]. In addition, these groups may also serve as the sensors to detect foreign gas molecules via reactions, of potential

applications in organic devices.

On the other hand, the multiple functional groups also increase the complexity of reactions. As we introduced above, each function group may have multiple binding pathways, and each mechanism may apply to different reaction sites(intra-dimer, inter-dimer or cross-dimer). Herein, we enumerate some case studies of multifunctional molecules on Ge(100), to highlight some reaction trends.

Exclusive bonding Due to the reversibility of cycloadditions on Ge(100), competition between [4+2] and [2+2] is thermodynamically controlled. The dominant products are [4+2] adducts due to unfavorable strain of four member ring in [2+2] products. Evidences are from 1,3-butadiene [52, 53, 59] and EVK [56].

Competitive bonding 2-propenenitrile [47, 48] was found to undergo [4+2] as well as [2+2] cycloadditions, due to the low reactivity of nitrile groups in the [4+2] addition. Unsaturated alphatic amines react with Ge(100) in N-dative bonding, N-H dissociation or [2+2] cycloaddition [84]. However, allyamines only form dative bonding and N-H dissociation without [2+2] cycloadditions [80, 137]. This shows the complexity of reaction in competition between multiple reaction channels. The ratio of competitive products can be tuned by changing the temperature or coverage.

Metastable bonding Most of dissociative reactions on Ge(100) start from dative bonding precursors, which we have introduced in section 1.3.3.

Multidentate bonding Molecules with multiple function groups separated by long and loose chains can bind to Ge(100) by their groups concurrently. The α-amino acids have carbonyl and amino groups septated by two carbon atoms, these two groups

can arrange themselves in suitable space configuration matching the surface dimer atoms. An "intrarow O-H dissociated and N-dative bonded" structure has been reported for glycine [89, 90], valine [92], serine [86], alanine [85, 88], leucine [88], proline [93]. Histine binds to Ge(100) by the imino nitrogen in the imidazole ring and the carboxyl group in the glycine moiety [91]. Methionine even has three anchoring groups, forming the "O-H dissociated, N-dative and S dative-bonded" structures [87].

To summarize, due to the weakness of the Ge-C bond, the adsorption product on Ge(100) can either be thermodynamically and/or kinetically controlled. Reaction mechanisms of multifunctional molecules with Ge(100) are complicated due to multiple reaction mechanisms. Coverage and temperature also play important roles in altering the reaction pathways. To date, molecular functionalization of Ge(100) remains a challenge and needs more work in this field.

1.4 Reactions of gaseous molecules on Ge(100)

1.4.1 Reactions of oxygen

The study of O_2 adsorption on Ge surfaces started in 1950s. Law and Francois recorded the change in work functions of Ge surfaces after adsorption of O_2 [138, 139]. Madix et al. found that O_2 oxidizes Ge surfaces at 525°C to produce gaseous GeO [140]. Madix's results were soon supported by Schmeisser et al., who detected +1, +2 and +3 oxidative states of Ge after reacting with O_2 by high resolution photoelectron emission spectra (HRPES). Upon annealing, all states convert to the +2 state, in contrast to the case on Si(100), where Si converts to stable +4 state in form of SiO_2. This is in

agreement with the results from Madix et al [140].

To better understand the oxidative process, more surface techniques were employed. Using low energy loss spectra (LELS), Ludeke and Koma found that each O atom forms two bonds with Ge surfaces at room temperature [141]. In 1982, Surnev and Tikhov observed that O_2 dissociates on Ge(100) via a molecular precursor state [142]. However, using molecular beam scattering technique, Hansen and Hudson found two mechanisms: the molecular precursor mechanism and the direct dissociation mechanism [143, 144]. Later, two dissociative products were imaged in STM images. The major protrusions appear at the top of the dimer centers, and the minor ones sit on top of dimer atoms [145–147]. Although these two protrusions were independently observed by Fukuda et al. [145, 148] and Grassman et al. [147], they interpreted these features in different ways. Fukuda and Ogino attributed the major protrusions to a dissociative product with one O atom on top of the dimers. The minor bright spots on dimer atoms were speculated to be a metastable phase by inserting oxygen into back-bonds of Ge dimers [145, 148]. In contrast, Grassman et al. attributed the main protrusions to the Ge adatoms being pushed outward due to oxidation [147]. The minor bright spots were assigned as the oxygen inserting into either back-bonds or dimers. Since STM cannot directly reveal the bonding details, Soon et al. employed electron energy loss spectroscopy (EELS) and DFT calculations to study the adsorption. They found that all EELS peaks were from Ge-O rather than O-O bond vibrations, proving that there is no nondissociative molecules on Ge(100) at room temperature. Their calculations demonstrated that O_2 first barrierlessly inserts one O atom into a dimer bond, followed by the cleavage of O-O bond and inserts the other O atom into a back bond of the same dimer with a barrier of 0.8 eV [149]. Dissociation of O_2 involving two dimers in a dimer row is kinetically unfavorable than the above intra-dimer pathway.

Despite the intensive investigation of dissociative products both experimentally and theoretically, the nondissociative product had not been traced after Hansen and Hudson's reports [143, 144]. Fan et al. pointed out that the sticking probability of O_2 is too low [150], if there was only proposed barrierless dissociation [149]. They suggested to consider the triplet state of O_2 in calculations, which is the ground state in nature. In this way, they found three nondissociative products of O_2. They are O_2 binding to the lower dimer atom via a Ge-O dative bond, O_2 chelating to the lower dimer atom by two Ge-O dative bonds, and O_2 bridging a Ge dimer by each O atom linking to one dimer. Although both singlet and triplet O_2 can dissociate to these three products, the dissociation barriers are different. The previous calculations using singlet state O_2 of high energy artificially depressed the energy barriers. Therefore the previous barrierless dissociative processes would have a non-zero barrier, which can explain the mentioned low sticking probability of O_2. Although their calculations demonstrated the significance of considering triplet and singlet states, the nondissociative adsorption still lacks conclusive support from experiments.

1.4.2 Reactions of hydrogen

The adsorption of hydrogen on Si(100) has been well studied [151], but less is known about the adsorption behavior of hydrogen on Ge(100). Hydrogen can react with Ge(100), producing three types of hydrides according to the occupation of dimer atoms by different number of H atoms. Dihydride consists of each dimer Ge atom occupied by two H atoms. Correspondingly, monohydride refers to each Ge dimer atom binding with one H atom. Hemihydride stands for each dimer bonded by one H atom.

1.4.2.1 Monohydride and dihydride

The stick probability of molecular hydrogen on Ge(100) is extremely low. The dissociation of H_2 needs to be thermally activated by a hot W filament during dosing. In 1978, Applelbaum et al. suggested that Ge(100)-2×1 retains its dimer after dosing [152]. Surnev and Tikhov surveyed the change in work function, surface conductivity and electron energy loss spectra as a function of relative hydrogen coverage on Ge surfaces [153]. Zhidomirov et al. attempted to calculate the band structure of Ge(100) after adsorption of hydrogen [154]. The above results contributed to early studies of hydrogen adsorption on Ge surface.

In 1986, Chabal investigated hydrogen saturated Ge(100) by High-resolution Infrared-spectroscopy(IR) and low-energy electron diffraction (LEED) [155]. The dominant 2×1 LEED pattern indicated that the H-saturated Ge(100) only consists of monohydride, when the dosage is lower than 450 L (1 Langmuir(L)=1×10^6 Torr·sec). The same conclusion was drawn by Lewis et al. according to the TPD and laser induced desorption(LID) spectra [156]. The monohydride begins to dissociate at 190°C to release hydrogen [157].

Using EELS, Papagno et al. observed the vibrations belonging to the dihydride when the dosage increases to 500∼4000 L [158]. The presence of dihydride was confirmed by Eggeling et al. via a detailed study of vibrational excitation mechanisms of hydrogen on Ge(100) [159]. The TPD spectra from Shimokawa et al. is of two desorption peaks, which were assigned to the monohydride and dihydride [160]. Ekerdt and Gong detected the dihydride species upon adsorption of H_2 using HREELS [161]. Cho and Nemanich found that the hydrogen plasma can also produce monohydride and dihydride on Ge(100) [162]. The dihydride becomes unstable and gradually converts to monohydride when

temperature increases.

Beside the vibrational and desorption spectra tools, STM was also used to directly image the monohydride and dihydride. Maeng et al. investigated the complicated surface evolution of Ge(100) exposed to atomic hydrogen at 300 K [163]. After exposure, the surface quickly forms 2×1 reconstruction with an average coverage of 1. However, despite the majority of the $2{\times}1$ phase, small fraction of unsaturated dangling bonding and dihydride were also imaged.

The desorption of hydrides was intensively studied because of the "*barrier puzzle*" existing both on Si(100) and Ge(100) [164]. The "*barrier puzzle*" refers to the contradiction between the lower sticking probability of hydrogen molecules on Ge(100) and the low desorption barrier [165]. Okamoto et al. showed that the electronic correlation effect plays an important role in estimation of desorption barrier [164]. The desorption of H_2 from Ge(100) in an interdimer way has the smaller reaction barrier than the intra dimer route. The desorbed H_2 from monohydride of Ge(100) has no kinetic energy, in agreement with the experimental facts. The combinational DFT calculation and statistics simulation by Mui et al. confirmed that the interdimer desorption model rather than the intradimer (pre-paring) one is more consistent with the desorption kinetics [166].

1.4.2.2 Hemihydrides

The hemihydride forms at the initial stage of hydrogenation of Ge(100). Radny et al. first predicted two hemihydrides: H on a lower dimer atom and on an upper dimer atom [167, 168]. In other words, regardless of the initial adsorbing sites, the dimer in hemihydride is antiparallel or parallel to the neighboring dimers in the same dimer row. The antiparallel configuration is more stable than the parallel one by 0.04 eV [168]. The

antiparallel one appears as the V-shape protrusion on the zig-zag chain of dimer rows in filled state STM images, because not only the unoccupied upper Ge atom, but also two neighboring upper Ge atoms are highlighted. The brightening was first explained by the surface charging induced by the biased STM tip according to their simulation STM image from a six-layers slab model with an external electric field [168]. Later Yan et al. demonstrated that a slab model thicker than seven layers is necessary to correctly reflect the electronic structures of hemihydride of Ge(100) [168, 169]. The V-shape protrusion is reinterpreted as the charge delocalization due to electrons transfering from the Ge-H bond to neighboring dimers. On the other hand, Saedi et al. experimentally observed the parallel configuration on Ge(100) by STM [170].

Since the hemihydride is involved in many organic dissociative process, the above results are also useful to interpret the STM images of X-H dissociative reactions. In addition, the above results demonstrated that even as the simplest molecule, the dissociative processes are still complex due to the existence of multiple binding sites. In the aspect of theoretical works, many calculations of Ge(100) were performed on cluster models or thin layer models. However, the above calculations of hemihydride strongly indicates that although thin layer slab models are able to predict the stable adsorption structures. They are likely insufficient to correctly describe the electronic structures on Ge(100). Thus, the future slab models with the thicker layers ($\geqslant$7 layers) is necessary to simulate STM image of Ge(100).

1.4.3 Reactions of halogens and halides

Reactions of halogens on semiconductor surfaces are of both fundamental and industrial interest. In semiconductor industry, reaction of halogens is used to etch the

semiconductor surfaces, to remove unwanted surface impurities in the microfabrication process. Thus it is crucial to understand the microscopic mechanisms of this surface process. The diatomic halogens and hydrogen halides react with Ge(100) via a relative simple mechanism: they dissociate on a single dimer. The halogenation of Ge surfaces can be used as an effective passivation method [171], or the pretreatment for future passivation [172].

1.4.3.1 Reactions of halogens

The etching of Ge(100) by halogens has not been well studied, the early research mainly focused on adsorption of chlorine and iodine on Ge(111). Halogens dissociate to form GeX and GeX_2 (X=Cl and I) on Ge(111) [173–176]. Unlike on Ge(111), iodine and chlorine only form GeX on Ge(100), where each I or Cl saturates a dangling bond [177, 178]. Using PES and STM, they confirmed that at any coverage, I_2 saturates two dangling bonds of a dimer without breaking the dimer bond, forming a $c(2 \times 2)$ pattern. Further adsorbed I_2 molecules stack on the surface to form an extra $c(2 \times 2)$ layer. Annealing causes the breakage of the Ge-Ge dimer bond, producing gaseous GeI_2 species. This intradimer dissociative product was also supported by the DFT calculation as well as STM simulation [179]. Total energy calculations [180] indicated that Cl_2 dissociation on a dimer is energy favorable, which was also supported by the PES results [181].

The reactions of Br_2 and F_2 are less studied among the halogens. Pepinskii et al. investigated the etching of Ge surfaces by immersing the wafer in liquid bromine. $GeBr_4$ was found to be the major product. Using PES, Schnell et al. proposed that the Br-saturated asymmetric Ge dimer was the most possible product after adsorption of Br_2 [181]. The STM images of Br_2, and F_2 adsorbed on Ge(100) were simulated [182,183].

1.4.3.2 Reactions of hydrogen halides

Gaseous halides are very reactive on Ge(100), and the products vary from fluorides to bromides. There are a few studies concerning the adsorption of hydrogen halide on Ge(100). Yota and Burrows found that NH_4 and HF can corrode Ge and GeO_2 [184], forming hexafluoro metallates with GeF_6^{2-} ionic groups [185]. Dipping Ge wafers in diluted HF solution produces the hydrophobicity, which cannot be retained for a long period in water [186]. Sun et al. studied the etching of Ge in dilute HF and HCl solution by synchrotron radiation photoelectron spectroscopy (SR-PES) [187]. Park et al. used multiple internal reflection Fourier transform infrared spectroscopy (MIR FTIR) to study the above etching process [188]. Their results demonstrated that etching by HF produces hydrides, whereas etching by HCl leaves Cl-terminated surface. A DFT calculation from Sanchez-Castillo et al. suggested that HCl dissociate in an intra-dimer path way [180]. The desorption of HCl and HBr was investigated by TPD. The products include H_2, HCl/HBr and $GeCl_2$/$GeBr_2$.

1.4.4 Reactions of gaseous oxides

Reactions of gaseous oxides with Ge surfaces are of both fundamental and industrial importance. In catalysis, Ge is widely used as additives to transition metal/oxides catalysts, to catalyze the selective oxidation of gaseous oxides. These catalytic processes will be reviewed in section 1.5. In addition, nitrogen oxides are used to nitridaze the Ge surfaces in application of Ge based transistors. Carbon monoxide (CO) can bind to Ge surfaces to change their work functions, resistivity and electronic structures. Herein, the reactions of nitrogen oxides (N_2O, NO) and CO with the Ge(100) surface are reviewed.

1.4.4.1 Reactions of nitrogen oxides: NO and N_2O

Reactions of nitrogen oxides with Ge(100) surface is highly interesting because of the capability of creating defects-free interfaces between Ge substrate and other high-κ gate materials [189–196]. Mahata et al. demonstrated that the presence of an ultra thin lossy GeO_x interfacial layer between the gate dielectric and the Ge(100) substrate. The GeO_x layer results in frequency dependent capacitance-voltage (C-V) characteristics and high density of interface states [190]. This is due to the structural defects and trapped charge states existing in the GeO_x layer. Nitric oxide plasma can eliminate most of the trapped states and provide the better performance of transistors. By wet nitric oxide pretreatment of the Ge surfaces, Li et al. demonstrated that Ge MOSFETs with HfTiON as the high-κ gate dielectric can be fabricated on Ge substrate with high quality [189]. Xu et al. from the same group further showed that lower leakage current of interface can be achieved using this wet NO pretreatment. [191, 194, 196] The nitridation of the interface can also decrease the penetration of Ta/Y/Hf elements in the high-κ dielectric layer into Ge substrates. N_2O was also investigated. Although not as good as NO, N_2O can also improve the performance of those Ge MOSFETs in a similar mechanism. On the other hand, since nitrous oxide (NO_2) reacts with Ge to form GeO_2 [197, 198], it is not suitable in nitridation of Ge(100).

Although nitridation of Ge by NO and N_2O is important to improve the performance of Ge MOSFETs, an atomic understanding of the mechanism is yet to be established. Sander et al. first studied the adsorption of multiple layers of NO on Ge(100) at 110 K using TPD and electron stimulated desorption (ESD) [199, 200]. The TPD spectra indicated that NO nondissociatively adsorbs on Ge(100). Surprisingly, there is no N-O stretching mode detected in HREELS spectra. The absence of N-O vibration modes was

proposed to be the consequence of non-polar NO dimers formed upon adsorption. After stimulation by the 600 eV electron beam, N_2 and N_2O were found on the surface and in the desorption products. The XPS spectra also suggested the existence of nitride on surfaces after stimulation. To verify the source of desorbed N_2 and N_2O, Davies et al. studied the electron stimulated desorption of N_2O under the similar conditions [200].

1.4.4.2 Reactions of carbon oxides: CO and CO_2

Carbon oxides generally have lower reactivities toward Ge than nitrogen oxides. Law et al. showed the sticking probability of CO on Ge was extremely low (1×10^{-3}) [138,139]. The sticking probability of CO_2 is so low that the adsorption of CO_2 can be neglected. The work functions of Ge surfaces are reduced after CO adsorption [201]. The adsorption of CO increases the conductivity of n-type Ge wafer, but decreases the conductivity of the p-type [202–206]. These phenomena clearly proved that CO adsorption causes strong band bending of Ge, indicating an electron-donation from CO to Ge surfaces. However, the electron-donating mechanism, in term of orbital interactions, is yet to be explored.

CO adsorption was mostly investigated on Ge(111) [207–209]. CO was reported to be trapped in a three-fold hollow site on Ge(111), indicated by UPS and ion-neutralization spectroscopy (INS) [209]. Lubezky et al. measured the IR spectrum of CO adsorbed on Ge powder [210]. Two C-O stretching modes at 2070 and 2132 cm^{-1} were attributed to chemisorbed and physisorbed molecules, respectively. By dosing high flux of CO via a hot tungsten filament, Kim et al. observed one dimensional chains of CO formed along dimer rows [211]. Their DFT calculation indicated that CO prefers to adsorb on the down dimer atom. However, up to now, many adsorption details such as the adsorption energy, adsorbate interaction and diffusion mechanism are to be explored.

1.5 Ge in catalysis

Ge has a variety of applications in catalysis. Beside the industrial application of Ge in polymerization, Ge was considered as an additive of catalysts in selective oxidation, dehydrogenation and electrocatalysis.

Krylov et al. first reported that Ge power can catalyze the oxidation of H_2 and CO [212]. CH_3OH dehydration catalyzed by Ge powder has a lower onset temperature at 150°C [212]. Similarly, isopropyl alcohol dehydrates at a temperature as low as 170°C. Other groups also investigated catalytic performance of Ge in these reactions as well as the work function variations of Ge during the catalytic process [8, 213]. Ge is able to decompose formic acid into H_2 and CO_2 [8, 50, 127, 213–216]. Among them, Filler et al. investigated this catalytic process by XPS, MIR-FTIR and DFT calculations. They found that the carboxylic group of formic acid forms a bidentate structure on Ge(100). It is this bidentate moiety that desorbs from the surface to produce CO_2 [216, 217]. On the other hand, formaldehyde first produces a C=O [2+2] cycloaddition precursor, followed by coupling with the neighboring C=O moieties to produce CO_2. Chiodo et al. demonstrated by DFT calculation that Ge is able to activate the reduction of NO_2 by CO [218].

Ge is also used as an additive to noble metal catalysts. Komastu et al. tested catalytic performance of Ge-Pt alloy in hydrogenation of butadiene [10]. The XPS results indicated that Ge transfers electrons to Pt, lower its reactivity. The hydrogenation of butadiene stops at the stage of 1-butene with extremely high selectivity. Serge et al. demonstrated that the Ge-Pt/Al_2O_3 catalyst with small amount of Ge reforms the hexane without fragments and aromatization, which is suffered in traditional Pt/Al_2O_3

catalyzed process [219]. The role of Ge in Ge-Pt/Al_2O_3, confirmed by Medellin et al., is to dilute the platinum conglomerates, to diminish surface density of Pt atoms and to inhibite the Pt hydrogenolysis [5].

Gyorffy et al. further demonstrated that higher selectivity can also be achieved in reforming methylcyclopentane and hexane using Ge-Pt/SiO_2 than Pt/SiO_2 [6]. This is because that in Ge-Pt/SiO_2 catalyst, Ge blocks contiguous Pt sites which cause the formation of coke. In another reaction, Hernan et al. found a high activity of Ge-Pt/SiO_2toward preferential oxidation of CO [220]. In this catalyst, the alloyed Ge and Pt are in close contact with each other. Ge was proposed to be the catalytic promoter, can adsorb oxygen and transfer oxygen to neighboring Pt atoms. On the other side, Ge modifies the electronic properties of Pt and lower the reactivity of Pt [221]. The electron donating from Ge was reported on Ge-Rh/Al_2O_3 catalyst for CO oxidation.

In electrocatalysis, Ge accelerates the electro-reduction of NO_3^- ions via modifying Pt|Pt electrodes [222]. The reductive products are also altered, from pure NH_3 in absence of Ge, to NH_2OH together with NH_3. Dima et al. proposed that the change of product is due to diluting effect of Ge. The adsorbed NO molecules lie flat on the surface. NO needs continuous Pt pairs to be reduced to NH_3. Ge dillutes the concentration of Pt pairs, thus depresses the formation of NH_3 [223]. Masahiro reported that modification of Rh and Ir electrodes by Ge can increase the oxidation rate of CO [224].

1.6 Objectives and scope

Although a great number of studies have focused on the surface chemistry of Ge(100) as reviewed above, a deeper and more thorough mechanistic understanding is still to be gained in various areas. Here we summarize several important research gaps of organic molecules and inorganic gas molecules on Ge(100):

- Adsorption of numerous multifuctional organic molecules on Ge(100) has been investigated. However, the rationalization of the reactions is difficult, due to the lack of comprehensive understanding of competitive reaction channels. More experimental and theoretical studies on the adsorption of multifuctional molecules are thus highly desirable.

- Especially, heterocycles with multiple heteroatoms such as S, N and O, are possible to attach to Ge(100) through dative bonding, [4+2], [2+2] cycloadditions and dissociation. The heterocycles may show novel reaction mechanisms or products. For example, pyrrole indirectly dissociates the N-H bond via αC dative bonding precursor. Thiophene adsorbs on Ge(100) dimer row via a S-Ge bonding to form one dimensional molecular chain. Thus, it is valuable to investigate the adsorption of other heterocycles due to possible novel adsorptional structures and reaction mechanisms.

- The fabrication of molecular devices on semiconductor surfaces needs a good understanding of the electronic properties of adsorbed organic molecules. Exploring the electronic structures, such as density of states and spacial distribution of orbitals of adsorbed molecules is essential to the design and application of organic device.

- The atomistic understanding of surface reactions of gaseous oxides on Ge(100) is important for the future design and development of Ge-containing catalysts.

The main aim of this thesis is to explore the surface reaction of heterocycles with two heteroatoms and important gaseous oxides on Ge(100) by a combination of STM, HREELS and DFT study. Specifically, 1,2-pyridazine, carbon monoxide, nitric oxide, were investigated. Our objectives and organization are listed as following:

- STM is powerful in providing information on the bonding sites and configurations of organic molecules on semiconductor surfaces. HREELS is sensitive to bond transformation of adsorbed molecules by measuring the vibrations of substrates and adsorbates. Calculation based on density functional theory is facile and robust to predict the stable adsorptional structure, the reaction barriers of multiple reaction channels. It is also useful to interpret HREELS and STM results via estimating vibrational frequencies, and simulating STM images for each possible adsorbed structures. To validate the characterization methods we employed, their principles and background theories are reviewed in Chapter 2.

- Pyridazine is a six-membered aromatic ring containing two neighboring N atoms. It has multiple possible binding mechanisms: [4+2] or [2+2] cycloadditions involving zero, one or two N atoms; C or N single dative bonding; double dative bonding. For each binding mechanism, the bonding site may be on top of lower dimer or upper dimer atom. In each of the above bidentate mechanisms, the bonding site could be intradimer, interdimer or crossdimer. These binding mechanisms and bonding sites convolute together to give a complicated reaction channel map. To explore which binding mechanism(s) is(are) most favorable, we employed STM, HREELS and

DFT calculations to study sub-monolayer of pyridazine on Ge(100). In addition, we attempt to image the orbitals of pyridazine on Ge(100) surface by STM. The results and discussion are presented in Chapter 3.

- Chapter 4 presents the investigation on the adsorption and binding mechanism of CO on Ge(100). We use DFT calculation to search the most stable adsorption sites. The bonding configuration is discussed by a crystal orbital Hamilton population(COHP) analysis. The adsorbate interaction and diffusion are also investigated.
- Adsorption of NO on Ge(100) was investigated by a periodic plane wave DFT calculation in Chapter 5. The monomeric and dimeric adsorption and the reaction barrier were calculated. Their electronic structures are also discussed.
- A conclusion was drawn in Chapter 6, where our findings were summarized and highlighted.

The results of this thesis may have significant impact on the surface chemistry of Ge(100). They may complement the current study of adsorption of heterocycles with multiple heteroatoms on Ge(100) and provide a new understanding of the reaction mechanisms. In addition, the study of CO adsorption on Ge(100) is helpful to understand the role of Ge in Ge-containing catalysts. The theoretical prediction of dissociation mechanisms of NO on Ge(100) will be useful to optimize the oxynitridation process of Ge.

Due to the time constraint, only a limited number of molecules has been studied in this thesis. Many other heterocycles, such as furan and 1,4-pyrazine are worthy of being

investigated but not included in this thesis. The study of other nitrogen oxides, such as N_2O and NO_2 is also interesting. It is hoped that they will be studied in future work.

Chapter 2

Experimental and computational methods

2.1 Principles of surface analytical techniques

To study the reactions on semiconductor surfaces, one needs to prepare clean semiconductor surfaces and retain them in a manageable period for conducting experiments. An ultra high vacuum (UHV) system is critical to achieve these goals. In addition, many surface techniques use electrons/ions as detecting beams. A UHV system can minimize the interference of electrons/ions from gas-phase scattering, and guarantee sufficient signals being detected. In this thesis, scanning tunneling microscopy (STM) and high resolution electron energy loss spectroscopy (HREELS) are used to provide the vibrational and electronic information of adsorbates on semiconductor surfaces. Beside the experimental tools, theoretical calculations based on density functional theory (DFT) are also employed to predict energetic, geometric and electronic properties of adsorption structures, to reveal the pathways of surface reactions and binding mechanisms. DFT calculations are also used to simulate the vibrational spectra and STM images. In following sections, UHV system, STM, HREELS and DFT calculation will be introduced.

2.2 Scanning tunneling microscopy (STM)

The first STM was invented in 1981 by Gerd Binnig and Heinrich Rohrer, who were awarded by the Nobel prize in 1986 [225]. Since then STM and its variants have become very powerful tools of atomic resolution in real space imaging to study the surface. Compared to other surface techniques, STM has distinct advantages such as:

- STM has extremely high atomic resolution (1 Å in lateral and 0.1 Å in depth). With this resolution, it is possible to resolve the atomic structures of surfaces. Many surface reconstruction models previously proposed by other techniques, for example, Si(111)-7 $\times$ 7 [225], are finally verified by STM. In addition, localized features disturbing the periodic structure such as vacancies, interstitials, impurity sites, steps, dislocations and grain boundaries, can be resolved by STM. STM is able to determine the adsorbing sites, configurations and even the binding mechanisms of adsorbates in the study of surface reactions.

- STM is capable of investigating geometric and electronic features. STM detects the convolution of geometric and electronic information of surfaces. By varying the operational condition, it is possible to reveal both the geometric and electronic structure of surfaces or surface adsorbates. For example it has been demonstrated that the orbitals of organic molecules on some substrates can be resolved by STM [226].

- STM can work not only in ultra-high vacuum, but also in air, water and other liquids. This guarantees the wider applications of STM compared to other electrons based surface tools. The working temperature also varies from a few Kelvin to hundreds of degrees Celsius.

- STM can work in scanning tunneling spectroscopy (STS) mode, which reveals the local density of states at specific location on surfaces (LDOS).
- STM can be used to manipulate the surface atoms and molecules.

2.2.1 Working principle

Figure 2.1 shows the energy diagram of the system comprising a tip and sample separated by a vacuum region. Without any bias, the vacuum level is the same everywhere. The Fermi levels of the tip and sample E_f lie below vacuum level by their work function ϕ, respectively. When the tip and sample approach each other close enough (typically 4∼7 Å in STM experiments), the electrons penetrate the vacuum and tunnel from sample to tip, or vice versa. The electrons in the tip and sample redistribute until the Fermi levels are aligned. Once the tip is applied by a positive bias whereas the sample is grounded, the Fermi level of the tip ($E_f(T)$) is lower than that of the sample. Electrons in the filled states of the sample will tunnel into the empty states of the tip. Reversely, if the tip is applied by a negative bias, electrons in the filled states of the tip will tunnel into the empty states of the sample. The intensity of tunneling current depends on the local electronic structures of the tip and sample, the distance between them, as well as the biases applied:

$$I_t = I(\vec{R}, d, V), \tag{2.1}$$

where $\vec{R}$ stands for the lateral position of the tunneling point on the sample, d is the distance between the tip and the sample, V is the bias. If the tip moves across the sample in the x-y plane, the changes in surface height and local density of states of the sample tune the tunneling current.

Based on Equation 2.1, STM has four working modes: constant current mode, con-

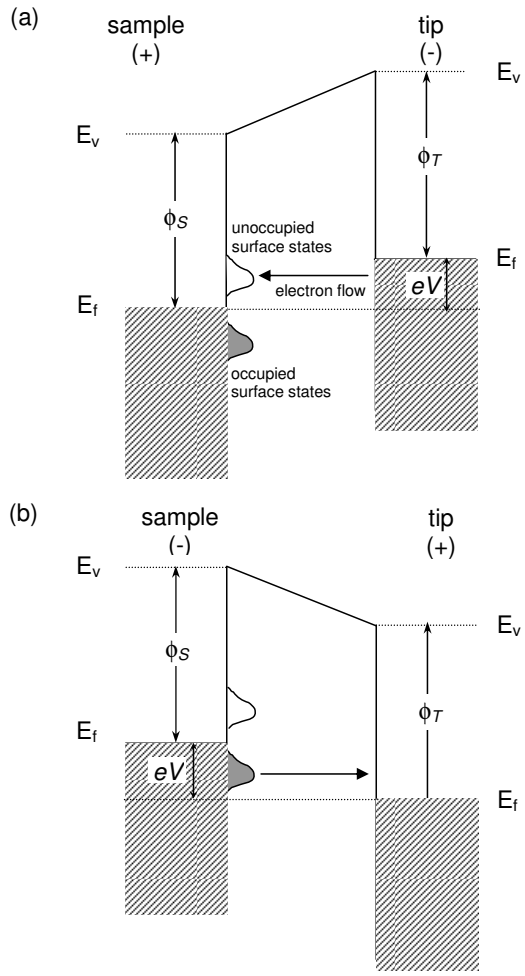

Figure 2.1: The energy level diagram of an STM tip and sample system with a bias. E_v and E_f represent the vacuum and Fermi level, whereas Φ_S and Φ_T are the work functions for the sample and the tip respectively. At (a) a positive sample bias, electrons tunnel from the tip to the unoccupied states in the sample and at (b) a negative sample bias, electrons tunnel in the opposite direction from the occupied states in the sample to the tip.

stant height mode, scanning tunneling spectroscopy mode and current imaging tunneling spectroscopy. In the first two scanning modes, usually the bias was kept as a constant. The constant current mode uses loop-feedback technique to adjust the distance d to keep the current constant. The height of the tip relative to the surface is recorded to directly reflect the morphology of the sample surface. The constant height mode fixes the height of tip during scanning, and the tunneling current varies as a result of change of the distance between the tip and surface. In addition to scanning across the sample, scanning tunneling spectroscopy (STS) maps the sample electronic structure at a specific location. The mapping is via sweeping the voltage and measuring the current when the lateral position $\vec{R}$ and distance d are fixed. Such measurements can be performed at a selected position, therefore revealing the I-V characteristics at that location. STS can also be performed during constant current/height scanning modes, which is the fourth mode—current imaging tunneling spectroscopy (CITS).

2.2.2 Instrumentation

Although STM is conceptually simple, implementing the idea to achieve atomic resolution requires a good mechanical design. STM comprises the scan translator, rough positioning unit and vibration isolation system. Figure 2.2 shows schematic diagram of typical components for a STM:

Sample The sample needs to be conductive to transport electrons. Metal and semiconductor are suitable for STM. In principle, STM can work on any conductive surfaces. To achieve good resolution and interpretable data, the surfaces are required to be clean and stable. Most of STMs ground the sample during scanning.

Tip The resolution of STM images is limited by the curvature radius of the tip. A sharp

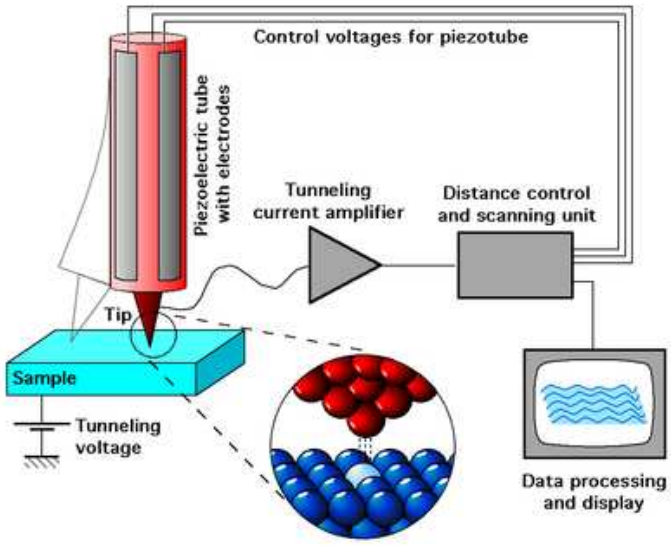

Figure 2.2: STM working principle and set-up

and stable tip is essential for atomic resolution. STM tips are usually made from chemically etched tungsten wires or mechanically sheared Pt/Ir alloy wires. The apex of tips consists of one or a few metal atoms. The tips can be further sharped in vacuum by ion bombardment or field emission.

Piezoelectric scanner The fine movement of the STM tip is implemented via operating the piezoelectric scanner, on which the tip is mechanically attahced. The scanning in x, y directions is via applying hundreds of volts on the gray piezoelectric bars (in Figure 2.2) so the scanning tube can blend at a specific direction. Combined with another piezoelectric rod in the center of the scanner, the scanning tube can approach or leave the surface in z direction. The alterative piezoelectric scanners can be tripod, bimorph or unimorph disk. The travel range of a piezotube is usually several micrometers.

Coarse motor The piezoelectric scanner is attached on a coarse motor, which is used to quickly approach to or withdrawn the scanner from the sample.

Vibration isolation system To achieve good resolution, the scanning system needs to be very stable and immune to mechanic instability. STM can be mechanically isolated from environment by hanging the system on springs. The eddy current damping system is used together to reduce the external vibrations.

Electronic control The tunneling current is usually a few picoamperes to nanoamperes. The current signal needs to be amplified before being fed into the control unit. The control unit supplies the voltages applied on the scanner tube, and decides whether to lock the tunneling current by varying the voltage on scanner, or lock the voltage on z direction piezoelectric rod. This unit also controls the x, y piezoelectric bars to manage the scanning directions, speed and range. The bias on the tip is also controlled by this unit. The unit externally connects to the computer, which collects the STM data and provides an user interface.

2.2.3 STM theory

2.2.3.1 Bardeen's approximation

Electron tunneling is the elementary quantum process that accounts for the operation of STM. Understanding the theory behind STM is essential to interpret and simulate the STM data. There are mainly four theoretical approaches to model the scanning tunneling current, proposed by Bardeen (the transfer Hamiltonian) [227], Tersoff-Hamman [228], Landauer-Bütticker (scattering) [229] and Keldysh (nonequilibrium Greens-function).

In Bardeen's model, the tunneling current based on the first order of perturbation theory is:

$$I = \frac{2\pi e}{\hbar} \sum_{S,T} f(E_T)[1 - f(E_s + eV)]|M_{TS}|^2 \delta(E_T - E_S), \tag{2.2}$$

where $f(E)$ is the Fermi-Dirac distribution function. Thus, $f(E_T)$ is the probability that a tip state at E_T is occupied, and $1 - f(E_s + eV)$ refers to the empty probability of sample state at $E_s + eV$. Equation (2.2) sums up all possible elastic hoppings from occupied tip states to the empty sample states. The transition matrix depends on the wavefunctions of the tip and sample in vacuum region by:

$$M_{TS} = \frac{\hbar^2}{2m} \int d\vec{A} \cdot (\Psi_T^* \vec{\nabla} \Psi_S - \Psi_S^* \vec{\nabla} \Psi_T), \tag{2.3}$$

where the integral is over any surface A lying entirely within the barrier region between the tip and the sample.

2.2.3.2 Tersoff-Hamman approximation

The above matrix is a convolution of the tip and sample wave functions. To extract the intrinsic electronic property of the surface, Tersoff and Hamann [228] assumed that the top of the tip is a hemisphere of a radius R, and the wavefunction is s-orbital type. At room temperature and lower bias condition (∼10 mV for metals), now the tunneling current can be estimated from (2.2) as:

$$I = V \cdot 32\pi^3 \hbar^{-1} e^2 \phi^2 D_T(E_f) \kappa^{-4} e^{2\kappa R} \sum |\Psi_s(\vec{r_0})|^2 \delta(E_s - E_f), \tag{2.4}$$

where $\vec{r_0}$ is the surface location, ϕ is the sample work function, D_T is the density of states per unit volume of the tip, E_f is the Fermi level, and κ is the inverse decay length for the sample wavefunction in vacuum with $\kappa = 2\sqrt{2m(\phi - E)}/\hbar$. Substituting typical metallic values into Equation (2.4), the tunneling conductance can be evaluated as

$$\sigma \equiv \frac{I}{V} \approx 0.1 R^2 e^{2\kappa R} \rho(\vec{r_0}, E_f). \tag{2.5}$$

It depends on the local density of states on the sample surface:

$$\rho(\vec{r_0}, E_s) \equiv \sum |\Psi_s(\vec{r_0})|^2 \delta(E_s - E_f) \propto e^{-2\kappa(R+d)} \tag{2.6}$$

Considering Equations (2.1) and (2.6), the tunneling conductance decays exponentially versus the distance of tip and sample:

$$\sigma \propto e^{-2\kappa d}. \tag{2.7}$$

Thus the tunneling current is highly sensitive to the distance, this guarantees the high vertical resolution of STM. Given R (stands for the shape of tip) is not changing during scanning, one can lock the tunneling current, and vary the height of tip so the contribution from local density states at any surface location is the same. The constant current mode in fact presents the contour map of constant LDOS of the sample surface at Fermi level rather than the purely topographic image. The height of tip is a convolutional effect of surface geometric morphologies and surface electronic density. On metal and elemental semiconductor surfaces, the constant current images approximately reflect surface morphology. However, on some binary compound semiconductors surfaces, like TiO_2, the contribution from surface local charge density predominate over the geometric effect. Thus the constant current STM images may not correctly reflect the geometric morphologies of those surfaces.

2.2.3.3 Lang's approximation

Tersoff and Hamann's approximation assume the bias is around several millivolts during scanning metal surfaces. For other substrates with wide band gaps, the biases usually are in the scale of volts. The scanning images were usually voltage-dependent.

[230] In such case, the tunneling current may also comes from the electron/state density below/above the Fermi level [231, 232]:

$$I \propto \int_{E_f}^{E_f+eV} dE \rho_T(E - eV)\rho_s(\vec{r_T}, E), \tag{2.8}$$

where bias V refers to tip as zero, $\rho_[T](E)$ is the state density of tip apex,$\rho_s(\vec{r_T}, E)$ is the sample state density at tip position $\vec{r_t}$. Considering the exponential decaying of the electron density in vacuum, Lang roughly estimated: [231, 232]

$$\rho_s(\vec{r_T}, E) \propto \rho_S(E) e^{\frac{-2d\sqrt{2m(\Phi+E_f-E+1/2eV)}}{\hbar}}, \tag{2.9}$$

where $\rho_S(E)$ is the density of states associated with the sample, Φ is work function of the sample, and d is the tip-sample separation. Once the tip DOS is assumed to be constant, substitution of (2.9) into (2.8) will result in:

$$I \propto \int_{E_f}^{E_f+eV} dE \rho_s(E) e^{\frac{-2d\sqrt{2m(\Phi+E_f-E+1/2eV)}}{\hbar}}. \tag{2.10}$$

From 2.10, the tunneling current for large band gap materials is proportional to the integral of the sample electron/state density $\rho_s$within $[E_f, E_f + eV]$ with energy related weighing factor $e^{\frac{-2d\sqrt{2m(\Phi+E_f-E+1/2eV)}}{\hbar}}$. Given the work function terms Φ ($\geq$3 eV for most large-band-gap materials) is larger than the bias term (usually $\leq$ 1eV), this weighing factor can also be treated as constant. The modified Tersoff-Hamann approximation now reads:

$$I \propto \int_{E_f}^{E_f+eV} \rho_s(E) dE. \tag{2.11}$$

Thus STS can reveal the local electronic structure—the local density of states (LDOS) from above equation:

$$\frac{dI}{dV} \propto \rho_s(E + eV) \tag{2.12}$$

dI/dV is normalized by I/V to eliminate the voltage dependance [233]. Equation (2.12) also reveal molecular orbitals can be mapped if $\frac{dI}{dV}$ is scanned along the whole surface in CITS working mode, because the electron density at certain energy is the square of molecular orbital at the same level:

$$\rho(E) = \sum_l |\psi_l|^2 \delta(E_l - E), \tag{2.13}$$

In another way, if the bias is small enough to only cover one frontier molecular orbital, namely HOMO or LUMO, they are resolvable in normal constant current mode.

$$I \propto \int_{E_f}^{E_f+eV} \rho_s(E)dE = |\psi_l|^2,\ when\ E_f + eV < E_{LUMO+1}\ or E_f + eV > E_{HOMO-1} \tag{2.14}$$

2.2.4 Orbital resolution with STM

STM mainly measures the spacial distribution of local density of states near Fermi level, which reveals the geometric and electronic structure of the investigated substances. It has been a long-standing goal to obtain the resolution of STM and to image more geometric or electronic information. Although atomic resolution is routinely achieved by STM, clear orbital resolution, especially for organic molecules remains an immature field. Usually, the rough electron density profiles of molecules were observed during conventional STM scanning, resolving the internal electronic properties, such as bonds and molecular orbitals was scarcely reported. The orbital resolution in fact has broad appli-

cations such as to visualize intermolecular interactions [234] and investigate reversible bond formation [235]. It has potential impact in studying the molecular surface chemistry, catalysis [236], monomolecular electronics [237] and organic photovoltaics.

Although the theory of imaging molecular orbital is rather simple as introduced in 2.2.3.3, to achieve such a resolution experimentally is rather challenging. The STM tips, substrates and molecules should to be carefully designed to avoid unwanted interferences.

2.2.4.1 Substrate requirements

Imaging orbitals of molecules requires the electronically decoupling of the molecules from the substrate. Most of STM scanning were performed on metal/semicondutor surfaces with abundant states near the Fermi levels, which will likely interfere with the molecular frontier orbitals (HOMOs and LUMOs).

To screen the interference from metal substrates, insulating layers were grown on metal surfaces. The insulating layer will separate the adsorbed molecules and substrate, allowing the sole observation of molecule orbitals. Repp et al. first electronically decoupled the pentacene molecules from metal surface by growing ultrathin insulating NaCl films on Cu(100) [238]. The unperturbed molecular orbitals of the individual pentacene were imaged. The results were supported by the elastic scattering quantum chemistry calculations. Using this screening technique, they also directly imaged covalent bond formation between a gold atom and a pentacene molecule [235]. Similar reversible gold-molecule bond formation was captured in case of gold-perylene-3,4,9,10-tetracarboxylic dianhydride supported by the NaCl/metal system [239]. In the presence of NaCl, the tunneling electrons may be trapped in the molecule, leading to ionic state [240]. The charge distribution of the ionic gold-molecule complexes could be resolvable [239]. How-

ever, since the interaction between the molecules and NaCl insulating film is quite weak, the adsorbed molecules are mobile on insulating films unless a low temperature (5 to 10 K) was applied.

The metal single crystal surfaces with native oxidation layers are also good substrates for resolving molecular orbitals. Guo et al. grew cobalt phthalocyanine (CoPc) molecules on Cu(001) with well-ordered oxidized layers and successfully imaged the frontier molecular orbitals of CoPc [241]. Their differential conductance mapping images were in excellent match with the calculated LDOS at energy levels near Fermi level. When the molecules self-assembly on to form ordered monolayer, these layers could serve as the screen film. Cheng et al. demonstrated that the frontier orbitals of iron (II) Phthalocyanine (FePc) can be resolved when this molecule was separated by a monolayer of FePc from a metal substrate [242]. This indicated that the screening was effective even the insulating layer is as thin as one monolayer. Similarly, the graphene sheet, which was naturally grown with one atom in thickness from the single metal surface, can effectively separate molecules from the metal substrates beneath. Zhou et al. showed that the intrinsic molecular orbitals of perylene-3,4,9,10-tetracarboxylic dianhydride, pentacene, and C_{60} were visible upon adsorbed on graphene/metal substrate. Furthermore, the graphite could be considered as graphene/semimetal system to image molecular orbitals. Gyamfi et al. successfully imaged the atomic/molecular orbital of the Ni adatoms/trimers on graphite surface, confirmed by their first principle calculations and symmetry analysis [243]. Gilman found that even in aqueous solution, the molecular orbitals of 8-fluoroindolo[2,1-b]quinazolin-6,12-dione (8-fluorotryptanthrin) on graphite were observed with orbital lobes [244].

There are some drawbacks to employ the insulating films. The interaction between

insulating films and molecules is weak, thus low temperature is necessary to immobilize the molecules. The charged tip is also easy to drag the molecules weakly adsorbed on insulating film, making the measurement difficult. The long residence time of tunneling electron in the molecules may result in distorted energy levels of orbitals or even decomposition [245]. Give the flat and semi-metallic graphene could be used as the screening layer, the metal substrate may directly contact the molecules for orbital imaging. Soe et al. proved that the molecular orbitals of pentacene can be observed directly on bare a Au(111) surface [246]. More work about orbital imaging are expected to emerge in near future.

Compared to extensive study on metal substrate, orbitals resolution was scarcely reported on semiconductor surfaces. Semiconductor surfaces have strong localize states, namely dangling bonds, which would bind the molecules through covalent (inclusive of dative) bonds. However, as a double side sword, such the formation of covalent bonds would severely interfere with the original orbitals of molecules. For those planar and aromatic molecules, lying on semiconductor surfaces will facilitate covalent bond formation. This will destroy the distort the entire electronic structure of the molecules. An successful example came from H-saturated Si(001), where hydrogen is used to eliminate localized surface states of Si(001) rather than to separate molecules and semiconductor [247]. Bellec et al. observed the HOMO of pentacene adsorbed on H-saturated Si(001) surface at 10 K. For those surface the dangling bonds are hard to eliminate, the molecule need to carefully design to avoid the interference, as we introduced later.

2.2.4.2 Modifications of STM tips

STM tips are usually made of tungsten or other noble metal wires [**?**]. The STM images heavily rely on the sharpness of the tips. In experiments, it is reality that people

work with STM spent lots of time to prepare good STM tip. The tips can be sharpen by exchanging, heating or sputtering of tips, applying a pulse, or even crashing tip repeatedly until sanctified resolution is achieved. To achieve the orbital resolution, the STM tips should to be as sharp as possible. However, in most of case, the resolutions of experimental scanning are usually lower than the theoretically simulated STM images. Particularly, the conventional scanning cannot resolve the orbitals' nodal planes, which are characteristic feature of orbital imaging.

The Tersoff-Hamann approximation simply treated the tip apex as a hemisphere with s-orbital [228]. Such an assumption surprisingly explain most of the STM images. Their theoretical simulations under such new assumption recover the results of Tersoff-Hamann modeling in condition of hemisphere tip apex. Chen et al. pointed out that STM images with s-orbital tip approximately resemble the local density of states, whereas for p-wave tip states, STM images will show spatial derivatives of the sample wave functions [248,249]. From Bardeen's approach (2.2), the tunneling current depends both on the density of states of the tip and substrate [250]. Recently, Gaspari et al. extended the Tersoff-Hamann tip assumption to that the irregular tip apexes were composed of multiple atom with s-orbitals [251]. The simulations were also in excellent agreement with their experimental STM images. This indicates that the geometrical shape of the tip may not be the sole determining factor once it has been sharp enough. Indeed, besides the geometrical sharpness, the components of tip apexes (the wavefunctions of the tip apexes) also plays a critical role in orbitals imaging.

Unfortunately, components of tip apexes usually are unknown after exposure to various resident gas in vacuum for a long time as well as the sharpening procedures. The image quality, which depends on the tip apexes, is often unpredictable. Once way

to consistently improve the STM resolution is to modify the STM apex by external atoms/molecules. Such a modification will greatly change the geometrical shape and tip apex wavefunction in a predicable way.

Carbon monoxide is the molecule often used for tip modification. By transferring a CO molecule from sample surfaces to the tip apex, Ho's group imaged the bond formation and orbitals of molecules on Ag(110) at 13 K [252, 253]. Gross et al. investigated the individual pentacene and naphthalocyanine molecules adsorbed using a CO-modified tip on NaCl/Cu(111) substrate [254]. The frontier orbitals of molecules were imaged with improved lateral resolution compared to the bare W tip. Kichin et al. used a CO-adsorbed STM tip to resolve the inner structure of 3,4,9,10-perylene-tetracarboxylic-dianhydride (PTCDA) adsorbed on Au(111) [255]. In their experiments, methane and Xe atom were also adsorbed and condensed on the tip to achieve an orbital resolution. O_2 decorated STM tip was also able to resolve the Fe/Zn phthalocyanine's molecular orbital [256]. Cheng et al. showed that their STM images agreed well with the extended Huckel theory calculations.

STMs with hydrogen adsorbed tips have their unique name—STHM. In 2008, Temirov et al. demonstrated that high atomic resolution STM images of PTCDA molecules [257]. The hydrogen molecule was proposed to insert into the tunneling junction, changing its position owing to Pauli repulsion, resulting in a change of tunneling current [258]. Similar results were obtained recently by Martinez et al. [259], who found that the hydrogen is in atomic form on the tip apex. In STHM, the hydrogen has been confirmed to serves as a transducer. This mechanism may be applied to other decorative molecules.

For other organic molecules or atoms with high boiling points or high reactivity, they can be attached on the tips at room temperature. Therefore, in principle low

temperature is no longer necessary. Xu et al. first prepared a monolayer of sulfur and iodine on the apex of STM tips using an electrochemical technique [260]. The images acquired by S-modified tips could ascertain the structural detail of thiol groups of the adsorbed molecules. The more popular method to cover the tip by organic molecules is picking them up from the substrate in vacuum STM operation. Perylene [261, 262], ethylene [253] were picked up as the decorative molecules for orbital resolution. However, such operations need delicate and experienced control of biases, tunneling currents as well as tip-sample distance.

In summary, modification of STM tips can be conducted via attracting molecules adsorbed on substrate by applying a pulse to the tips, condensing small molecules from the vacuum under low temperature, or picking up molecules by gently indentating into the substrate. The tip apexes can be decorated by external atoms/molecules in these repeatable and control ways. In addition, chemical components of tip apexes after modification were usually predictable, allowing more elaborate theoretical simulations counting the tip effect. The drawback of these methods both need delicate and experienced STM operation, or ultra low temperature.

2.2.4.3 Choice of molecules

Up to now, the popular choices are the large, planar, and aromatic molecules, such as perylene derivates [239], pentacene [235,238], metal-Phthalocyanines. The aromaticity of these molecules increase the chemical stability, guarantee unreacted delocalized π molecular orbitals to be observed. Their large sizes and high density of states near the Fermi levels favor the spacial mapping of the orbitals. As lying on the substrate, these molecules were not spatially decoupled from the substrate surfaces. There exist a paradox between decoupling and binding strength. Metal surfaces have sufficient electronic decoupling

but insufficient interaction. Semiconductor surfaces binds the molecules strongly, but suffering from distortion of molecular orbital from reactive dangling bonds.

There are other non-planar molecules chosen for orbital imaging, such as Cyclophane [263], N,N'-bis(1-hexylheptyl)perylene-3,4,9,10-bis(dicarboximide) (DHH-PTCDI), C_{60} [264]. Those non-planar molecules chemically bind to the substrate, leaving the major part of molecules intact. Thus the part being observed is electronically "self-decoupled" from the substrate. This "self-decoupling" technique allows the molecules to be firmly anchored on the substrate, favoring the STM observation and manipulation. The low temperature is also no need for these systems. In addition, the substrate was no long limited to the metal surfaces. The only consideration is the binding mechanism between the molecule and substrate.

2.2.4.4 Issues of orbital imaging

As reviewed above, the orbital resolved STM imaging allows the observation of electronic properties in real space. This immature technique, has bright future and wide applications. Some critical issues of this technique should to be solved in future. The conductive substrates are expected to be used directly without any screen film. The modification of the STM tips needs to be conducted in a controllable and robust way. More divergent classes of molecules could to be observable which allow more broad application of this technique. To address these issues, we conducted some pioneering work in Chapter 3.

2.3 High resolution electron energy loss spectroscopy (HREELS)

High resolution electron energy loss spectroscopy (HREELS) is a surface tool to detect the inelastically scattered electrons from surfaces, to study electronic excitations or vibrational modes of the substrate and molecules adsorbed on the substrate [265]. Lucas et al. first proposed the dielectric theory to provide a quantitative description of the electron energy loss spectra obtained at the specular direction [266]. The theory was originally based on isotropic crystalline materials, then extended to anisotropic or more complex surfaces.

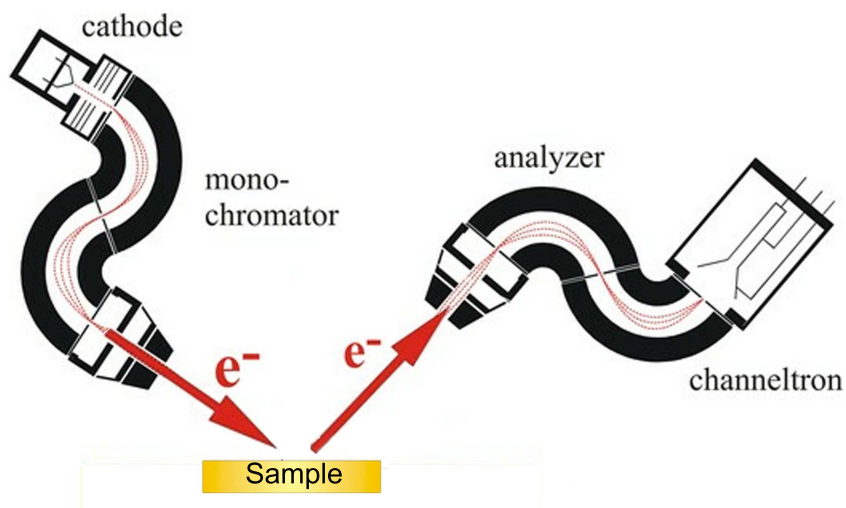

Figure 2.3: The schematic diagram of high resolution electron energy loss spectroscopy system (LK3000).

Generally, EELS bases on the energy loss of electrons in inelastic scattering processes, as shown in Figure 2.3. A highly monochromatic electron beam with energy E_0 impinges on the sample surface may excite a quantum state of $\hbar\omega$, and losses the equivalent energy.

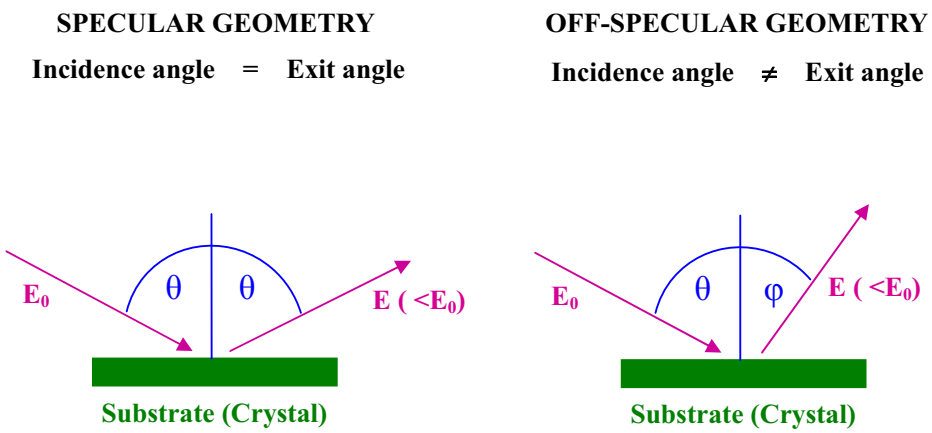

Figure 2.4: The schematic illustration of specular and off-specular geometries in HREELS experimental methods.

Two major scattering mechanisms, namely dipole scattering and impact scattering were proposed to interpret the electron interaction with surface vibrations. The dipole scattering mode is applied when the scattered beam is very close to the specular direction as shown in Figure 2.4. As the surface has asymmetric electron density distribution along the surface normal direction, thus an array of dipole moments exist. When a molecule is adsorbed on the surface, there is an dipole moment for the molecule. These two dipole moments cause a long range, time dependent potential in the vacuum region above the surface. The incident electrons inelastically interact with oscillating electric fields and excite the dipole active vibrations.

Let $\vec{k_i}$ and $\vec{k_s}$ be the wave vectors of incident and scattered electron beams. The cross section of inelastic scattering of electrons contains the scalar product of $\vec{k_s} - \vec{k_i}$ and the polarization of the normal model of the vibrations. Assume the electrons are sufficiently fast to sustain their horizontal velocity, $\vec{k_s} - \vec{k_i}$ is perpendicular to the surface. Therefore only those vibration modes which have vertical polarization projection can be excited by incident electrons. Considering the localized bond stretching, all vibrations parallel

to the surface cannot be excited by incident beams. The dipole scattering has sharp angular distribution along the specular direction.

In the "impact scattering" mechanism, the incident electrons are scattered by short range interaction, which is in the scale of Å. This short range scattering mechanism involves a much larger momentum transfer ($\vec{k_s} - \vec{k_i}$), and produces a broad angular distribution. The impact scattering results in "relaxation" of the surface selection rule so that all vibrations (both parallel and perpendicular to the surface) can be excited. Vibrations excited by impact scattering are best observed at off-specular direction(Figure 2.4). The impact scattering mechanism has the same selection rule as the dipole scattering.

A third mechanism "negative ion resonance scattering" is an extreme example of impact scattering. The incident electron is trapped into a temporary negative ion state by injecting electron into the unoccupied orbitals of molecules. This mechanism responses to particular impinging energy and has distinctive angular distribution related to the symmetry of the molecule and the negative ion state.

A typical HREELS instrumentation is shown in Figure 2.5, and the structural diagram is shown in Figure 2.3. The hot cathode made of LaB_6 emits electrons induced by an electric field. The electron beam is focused before entering into a two-stage 127° cylindrical deflector monochromator (CDM). After being monochromated by the CDM, the beam impinges the sample surface with an incident angle of 60°. The ejected electrons are collected at a specular or off-specular direction by a two-stage cylindrical deflector analyzer (CDA), finally amplified by a channeltron. The scanning of energy was performed via sweeping voltages applied on the analyzer.

Unlike photons, low energy electrons (<10 eV)do not penetrate into the bulk. They

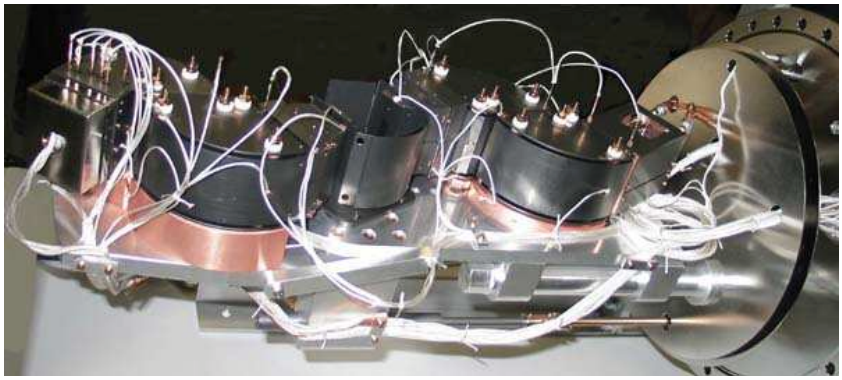

Figure 2.5: LK3000 HREELS instrumentation.

are only able to interact with the outermost one or two monolayers of the substrate. Thus HREELS is an intrinsically surface sensitive technique. Compared to fourier transform infrared spectroscopy (FTIR), which needs a background spectrum, HREELS can directly measure both clean and adsorbate covered surfaces. In addition, the measuring range of HREELS can cover the whole vibration region by varying the analyzer voltages, unlike IR which cannot measure the region <1000 cm^{-1} without specialized windows and detector technology. However, HREELS has some inherent disadvantages as an typical electron spectroscopy, such as the low resolution (10 cm^{-1}, compared to 0.8 $^{-1}$ for FTIR), and the requirement of UHV. Nevertheless, as a surface sensitive vibrational tool, HREELS plays an important role in the investigation of surface structures, catalytic processes, dispersion of surface phonons and epitaxial growths.

2.4 Experimental procedures

2.4.1 Ultra-high vacuum chamber (UHV)

Our experiments were performed in a ultra-high vacuum (UHV) chamber, which is locally designed and custom-made using type-304 stainless steel from MDC Corporation (USA). The chamber is pumped by two turbo molecular pumps (V310, V70, Varian), a sputter ion pump (Perkin Elmer) and a titanium sublimation pump (TSP, Perkin Elmer), retaining a base pressure of 2×10^{-10} Torr. The chamber is also equipped with an ion sputtering gun (PHI Model 04-161) for sample cleaning, two fine leak valves for chemical dosing. An XY-Z rotary manipulator (VG Omniax series) allows the sample motion along x, y, z directions as well as 360° rotation.

The chamber is equipped with HREELS (LK3000, LK Technologies, USA) to study the vibrational properties. An electron beam of 6.32 eV monochromated by a double-pass 127° cylindrical deflector analyzer impinges on the sample surface at an incident angle of 60 ° with respect to the surface normal. The scattered electrons were collected by two 127° cylindrical deflector analyzers, amplified by a channeltron. The signal is finally converted and analyzed by computer software ELS3000. A resolution of 6 to 8 meV (50 to 65 cm^{-1}, FWHM) was routinely achieved on clean germanium surfaces. All the EELS spectra were collected at liquid nitrogen temperature after annealing the sample to the desired temperatures.

A commercial STM chamber (OMICRON VT STM) is bolted to the main chamber via an 8” O.D. flanged port. As shown in Figure 2.6, the STM stage is suspended by four springs for isolating the vibration. The eddy current damping system surrounding

the STM stage further decreases the external vibration, to achieve sufficient stability for STM operation. When the STM stage is pushed up and locked by the the push-pull motion drive (PPM), the sample or tip plate can be handily exchanged by an pincer grip wobble stick. The STM is available for low temperature operation by sliding over a cooled clamping block on the backside of the sample plate. The sliding is manipulated by an UHV screw driver feedthrough on the top of the STM chamber (not shown in Figure 2.6). Through highly flexible copper braids, the clamping block is thermally coupled to a cryostat. The cryostat is further connected to a liquid nitrogen reservoir outside the vacuum via a cold finger at the base flange of STM chamber.

Our experiments require annealing the sample to 1000 K and cooling it to 110 K. The wide range of operational temperature of samples is implemented via attaching an OMICRON UHV standard sample heater stage to a home made, Dewar-type liquid nitrogen (N_2) cooled sample holder. When a direct heating sample plate (OMICRON SP VT DH) mounted with a germanium sample is inserted into the slot of sample stage, the sample can be annealed by passing a current through the germanium sample. The sample plate can also be radiatively degassed by passing a current (∼1.2 A) through a ceramic enclosed tungsten filament behind the sample plate. On the other hand, 110 K could be achieved by filling the sample holder with liquid nitrogen. The temperature is measured by a K-type (Goodfellow) thermocouple spot-welded to the screw on the sample stage (Figure 2.7). High temperature >550 °C is measured using an infrared pyrometer (TR-630, emissivity=0.55, Minolta), with a temperature resolution of ± 10 K below 1000 K. To avoid charging of the sample plate in HREELS experiments, the insulating ceramic cover of the direct heating sample plate was removed and replaced by two tantalum nuts.

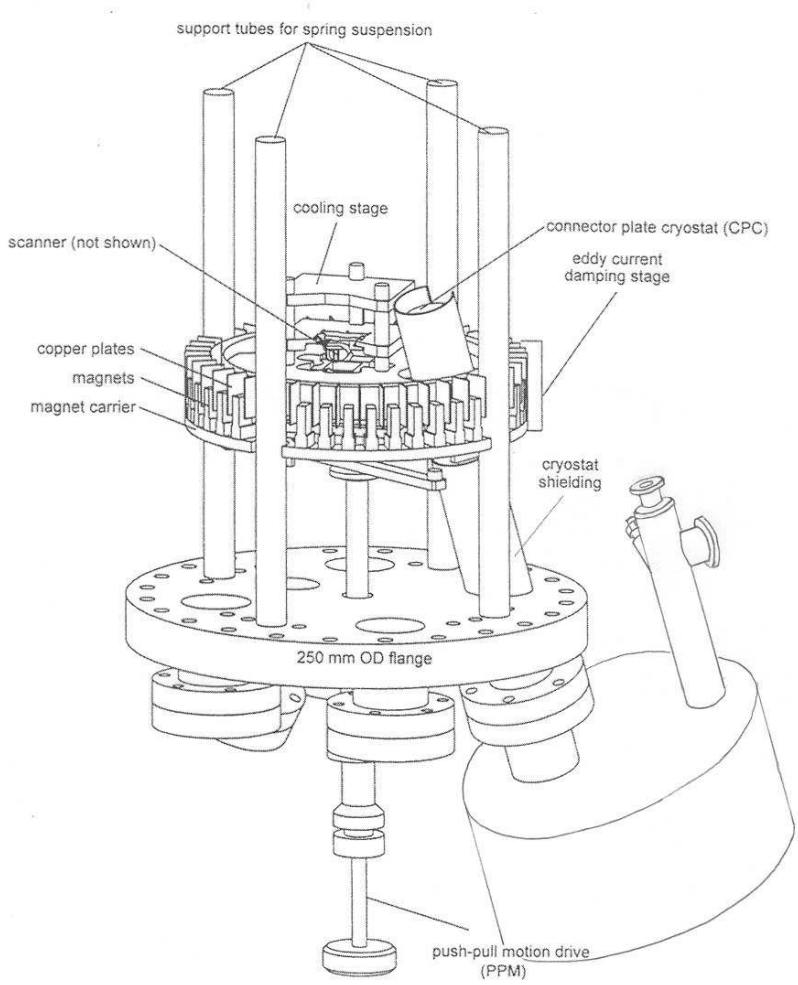

Figure 2.6: Schematic diagram of the OMICRON VT STM.

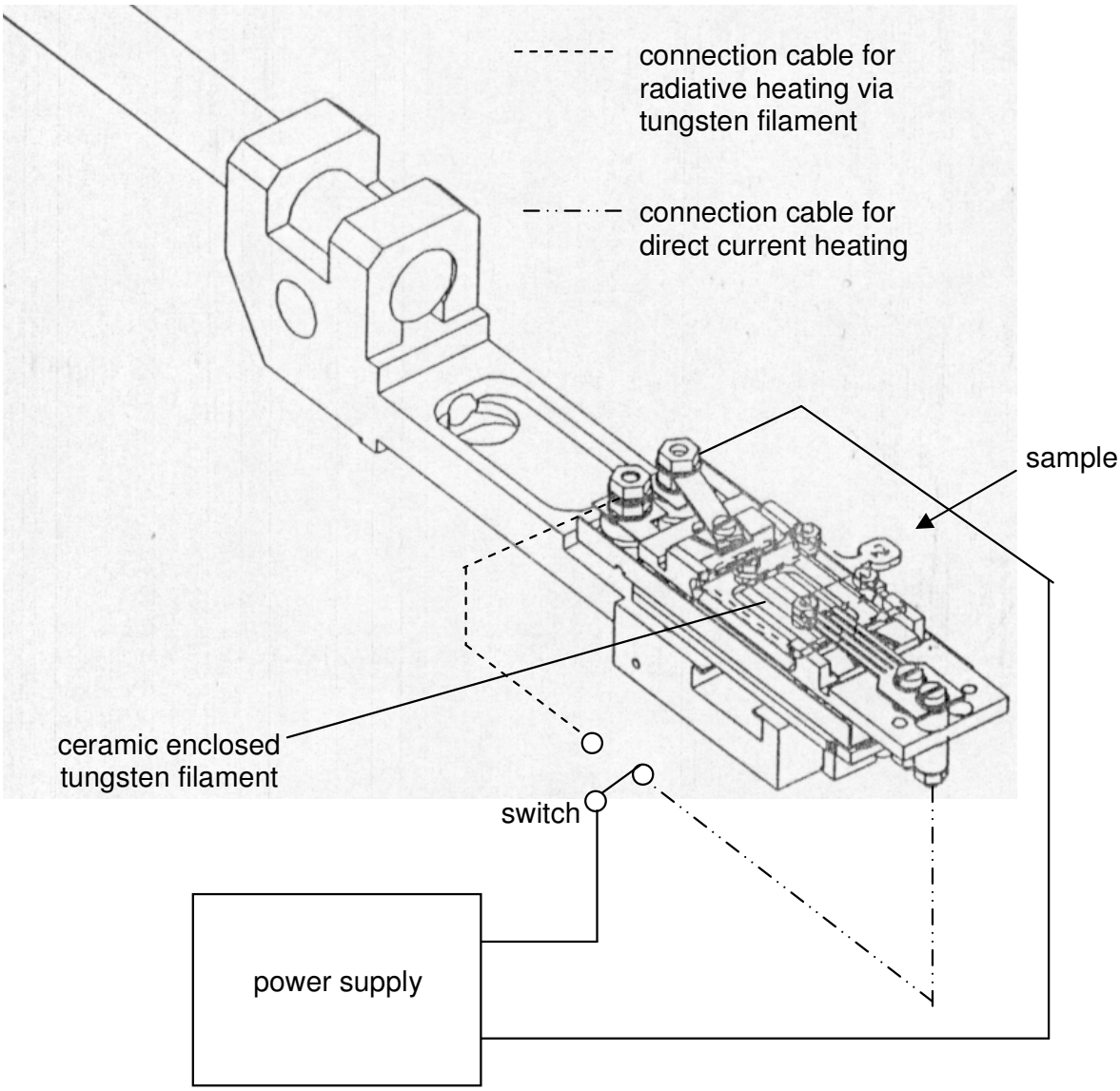

Figure 2.7: Schematic diagram of the manipulator, sample heater stage with the electrical circuit connection for sample heating

2.4.2 Sample preparation

The germanium samples (10 × 3 × 0.38 mm), cut from n-type Sb-doped germanium wafers (purity 99.999%, 0.1-10 Ω×cm, MTI), were ultrasonically cleaned in HPLC methanol to remove carbonaceous contaminants. After being mounted onto the sample plate, the sample was loaded into chamber. The sample plate was radiatively degassed at about 500 K for one day, followed by degassing the sample via directly heating at 600 K for 12 h. Such a degassing process minimizes the contamination of outgassed impurity surrounding the sample, critical to achieve an atomic clean surface. As the melting point of germanium 1210 K is too low to evaporate carbon impurities, Ar^+ bombardments were necessary to cleave the surface to remove carbon. The Ar^+ bombardment (1000 V, 30 minutes, sample current 5 to 10 μA·cm^{-2}) was performed at a background pressure of 3×10^{-5} Torr, followed by flashing the sample to 1000 K for 5 seconds. The sputtering/annealing procedures were repeated for several cycles until an atomic clean surface was observed under STM.

2.4.3 Organic molecules

All organic molecules were purchased from Sigma-Aldrich with high purity (> 99.9%). The molecules in liquid state at room temperature were allowed to evaporate from a glass bulb connected to a variable leak valve through a gas line, after being purified by several cycles of freeze-pump-thaw technique. The fine leak valve enables the precise control of the amount of molecules entering the chamber, as monitored by the background pressure. The dosing tube aims at the Ge sample with the dosing aperture 5 cm away from the sample plate in HREELS experiments. The exposure was calculated using the the dosing pressure and time. The in-situ dosing was conducted using the same doing facility during

STM scanning, the coverage was directly monitored by STM imaging.

2.5 Theoretical Calculations

2.5.1 Density functional theory

2.5.1.1 Schördinger equation

In solving the many-body electronic structure, the positions of nuclei in the treated system are frozen by Born-Oppenheimer approximation. They generate an external potential towards the moving N electrons, which can be described by a wavefuction $\Psi(\vec{r}_1, ..., \vec{r}_N)$ satisfying the time independent Schrödinger equation.

$$\hat{H}\Psi = \left[\hat{T} + \hat{V} + \hat{U}\right]\Psi = \left[\sum_i^N -\frac{\hbar^2}{2m}\nabla_i^2 + \sum_i^N V(\vec{r}_i) + \sum_{i<j}^N U(\vec{r}_i, \vec{r}_j)\right]\Psi = E\Psi \quad (2.15)$$

$$V(\vec{r}_i) = \sum_{A=1}^M \frac{-Z_A e^2}{\vec{r_i} - \vec{r_A}} + V_{ext}(\vec{r_i}) \quad (2.16)$$

Here $\hat{T}$ and $\hat{U}$ are universal operators of kinetic energy and electron-electron interaction energy independent of individual system. In contrast, $\hat{V}$ depends on the positions of nucleus and external electronic field ($V_{ext}(\vec{r_i} = 0$ as no external electronic field is not concerned in this project). The single electron approximation treating $\hat{U}$ as part of external potential is usually applied to obtain approximate solution of the N-electron wavefunction. Thus a single electron Schrödinger equation group could be written as:

$$\hat{H}\psi_l = \left\{-\frac{\hbar^2}{2m}\nabla_l^2 + V_s(\vec{r_i})\right\}\psi_l = E_l\psi_l \quad (l = 1 \cdots N) \quad (2.17)$$

The N solutions are eigenorbitals to be occupied by each electron. To fulfill the requirement of exchange symmetry of electrons, these single electron wave functions need to combined in the form of Slater determinant:

$$\Psi = \Psi(\vec{r_1}, \vec{r_2}, \cdots, \vec{r_N}) = \frac{1}{\sqrt{N!}} \begin{vmatrix} \psi_1(\vec{r_1}) & \psi_2(\vec{r_1}) & \cdots & \psi_N(\vec{r_1}) \\ \psi_1(\vec{r_2}) & \psi_2(\vec{r_2}) & \cdots & \psi_2(\vec{r_2}) \\ \vdots & \vdots & \ddots & \vdots \\ \psi_1(\vec{r_N}) & \psi_2(\vec{r_N}) & \cdots & \psi_N(\vec{r_N}) \end{vmatrix} \equiv |\psi_1\psi_2\cdots\psi_N| \quad (2.18)$$

2.5.1.2 Kohn-Sham equation

In Hartree-Fock method, $V_s(\vec{r_i})$ is calculated from three/four-centers-integrals between basis wave functions. Density functional theory starts from a different point. In 1964, Hohenberg and Kohn proved that the ground-state wavefunction of a system is solely determined by the electron density $n(\vec{r})$ (HK theorem 1) [267]:

$$\Psi = \Psi\left[n(\vec{r})\right] \quad (2.19)$$

Therefore the system energy and other derivatives from the energy can also be deduced from $n(\vec{r})$:

$$E = E\left[\Psi\right] = \left\langle \Psi\left[n(\vec{r})\right] \middle| \left[\hat{T} + \hat{V} + \hat{U}\right] \middle| \Psi\left[n(\vec{r})\right] \right\rangle, \quad (2.20)$$

where the potential contribution $\left\langle \Psi\left[n(\vec{r})\right] \middle| \hat{V} \middle| \Psi\left[n(\vec{r})\right] \right\rangle$ now can be written in terms of electron density:

$$V[n(\vec{r})] = \int V(\vec{r})n(\vec{r})d\vec{r}. \quad (2.21)$$

For the other two terms $\hat{T}$ and $\hat{U}$, there exists an energy functional F_{HK} with respect

to the electron density $n(\vec{r})$, from which the ground electronic state can be derived (HK theorem 2). The functional can be written as

$$F_{HK} = T[n(\vec{r})] + U[n(\vec{r})] \tag{2.22}$$

where $T[n(\vec{r})]$ and $U[n(\vec{r}))]$ are kinetic and potential terms respectively. If the exact form of F_{HK} could be resolved, the calculation of electronic structures would be much simpler, because the cost of calculation would be reduced to one single spatial vector $(\vec{r})$, rather than N vectors in Hartree-Fork equation.

Unfortunately, the exact form of F_{HK} is a mystery, even any tempt to find a local approximation of F_{HK} failed. In 1965, inspired by the success of Hartree-Fock method, Kohn and Sham suggested a practical way to solve the Hohenberg-Kohn theorem [268]. In their way, the F_{HK} is separated into three parts:

$$F[n(\vec{r})] = T_s[n(\vec{r})] + \frac{1}{2}\int d\vec{r}d\vec{r'}\frac{n(\vec{r})n(\vec{r'})}{|\vec{r}-\vec{r'}|} + E_{xc}[n(\vec{r})], \tag{2.23}$$

where $T_s[n(\vec{r})]$ is defined as the kinetic energy of a non-interacting gas with density $n(\vec{r})$, which is expected to be close to $T[n(\vec{r})]$. The second term is the classical electrostatic (Hartree) energy, and the final term $E_{xc}[n(\vec{r})]$ contains the non-classical electrostatic interaction energy and the difference between $T_s[n(\vec{r})]$ and $T_s[n(\vec{r})]$. Once we have any set of orthonormal Kohn-Sham molecular orbitals that can produce the electron density of non-interacting system:

$$n(\vec{r}) = \sum_{l=1}^{N} |\psi_l(\vec{r})|^2, \tag{2.24}$$

then the kinetically energy term can be accurately calculated as:

$$T_s[n(\vec{r})] = \sum_{l=1}^{N/2} \left\langle \psi_l^*(\vec{r}) \left| -\frac{\hbar^2}{2m}\nabla^2 \right| \psi_l(\vec{r}) \right\rangle . \tag{2.25}$$

The Khon-Sham energy of the system is obtained by substituting (2.21), (2.23), and (2.25) into (2.20):

$$E_{KS}[n] = T_s[n(\vec{r})] + \frac{1}{2}\int d\vec{r}d\vec{r'}\frac{n(\vec{r})n(\vec{r'})}{|\vec{r}-\vec{r'}|} + E_{xc}[n(\vec{r})] + \int V(\vec{r})n(\vec{r})d\vec{r} \tag{2.26}$$

In the above Kohn-Sham energy expression, the kinetic energy is the functional of the Kohn-Sham molecular orbitals. The rest terms in the functional of the exact interacting electron density, which is made up from the molecular orbitals of the non-interacting electrons. Therefor the energy finally is the functional of the Kohn-sham molecular orbitals. Following the variational principle, we minimize the energy with respect to the density, or to the molecular orbitals which produce the density. The following Lagrangian expression is minimize to ensure the orthonormality of the Kohn-Sham MOs:

$$\Omega_{KS}[n] = E_{KS}[n] - 2\sum_{i=1}^{N/2}\sum_{j=1}^{N/2}\epsilon_{ij}\left(\int \phi_i^*(\vec{r})\phi_j(\vec{r})d\vec{r} - \delta_{ij}\right). \tag{2.27}$$

The Khon-Sham MOs that minimize the energy satisfy the condition:

$$\frac{\delta\Omega_{KS}[n]}{\delta\phi_j^*(\vec{r})} = 0. \tag{2.28}$$

Using the chain rule, we have:

$$\frac{\delta\Omega_{KS}[n]}{\delta\phi_j^*(\vec{r})} = \frac{\delta\Omega_{KS}[n]}{\delta n(\vec{r})}\frac{\partial n(\vec{r})}{\partial\phi_j^*} = \frac{\delta\Omega_{KS}[n]}{\delta n(\vec{r})}2\phi_j(\vec{r})$$
$$= 2(-\frac{\hbar^2}{2m}\nabla^2\phi_j(\vec{r})) + 2\left(\frac{\delta E_H}{\delta n} + \frac{\delta V[n]}{\delta n} + \frac{\delta E_{xc}}{\delta n}\right)\phi_j(\vec{r}) - 2\sum_{i=1}^{N/2}\epsilon_{ij}\phi_j(\vec{r}) = 0. \tag{2.29}$$

The set of $\{\phi\}$ could be transformed to a new set of orbitals $\{\psi\}$ with the same electron density but a diagonal matrix of lagrange multipliers. Therefore we obtain a set of equations:

$$\left\{-\frac{\hbar^2}{2m}\nabla^2 + V_{KS}(\vec{r})\right\}\psi_j(\vec{r}) = \epsilon_j\psi_j(\vec{r}) \tag{2.30}$$

with

$$V_{KS}(\vec{r}) = \sum_{A=1}^{M}\frac{-Z_A e^2}{|\vec{r}-\vec{R_A}|} + V_{ext}(\vec{r}) + \int d\vec{r'}\frac{e^2 n(\vec{r'})}{|\vec{r}-\vec{r'}|} + \frac{\partial E_{XC}(n(\vec{r}))}{\partial n(\vec{r})}. \tag{2.31}$$

The Kohn-Sham orbitals are fictious and have no physical meaning. However, they are the to date the best one to describe orbital electron densities in experiments including STM scannings [269]. In (2.31), the Coulomb and exchange-correlation potentials depend on the electron density thus on Kohn-Sham MOs, which are exactly what we want to solve in the (2.30). A self-consistent filed (SCF) calculation, in an iterative procedure needs to be used to search those MOs, which will be described in **??**.

2.5.2 Exchange-correlation functionals

The key to solution of the equation (2.30) is to find a good approximation of E_{XC}. Currently the local density approximation (LDA) and generalized gradient approximation (GGA) have been widely used. Deduced from the uniform electron gas model, LDA assumes that the electron density varies slowly on an atomic scale. The XC energy

depends on the local electron density of a system:

$$E_{XC}^{LDA}(n(\vec{r})) = \int n(\vec{r})\varepsilon_{XC}n(\vec{r})d\vec{r}. \tag{2.32}$$

Here ε_{XC} is the exchange-correlation energy per particle of a uniform electron gas of density $n(\vec{r})$. ε_{XC} can be further split to the exchange and correlation contributions:

$$\varepsilon_{XC} = \varepsilon_X + \varepsilon_C. \tag{2.33}$$

The exchange part was derived by Bloch and Dirac:

$$\varepsilon_X = -\frac{3}{4}\sqrt[3]{\frac{3n(\vec{r})}{\pi}}. \tag{2.34}$$

However, the correlation part has no explicit form. It can be obtained from numerical quantum Monte-Carlo simulations of the homogeneous electron gas.

Considering the spin, local spin-density approximation (LSD) was developed. Another way to improve LDA is considering the inhomogeneity of electron gas which is natural in molecular systems. Generalized gradient approximations (GGA) considers the electron density at each point in space and its gradient as shown in (2.35):

$$E_{XC}^{GGA}(n(\vec{r})) = \int f\left(n(\vec{r}_\alpha), n(\vec{r}_\beta), \nabla n(\vec{r}_\alpha), \nabla n(\vec{r}_\beta)\right) d\vec{r} \tag{2.35}$$

, where α and β refer to up and down spins. A reduced density gradient for spin σ is used to evaluate the inhomogeneity of electron density:

$$s_\sigma(\vec{r}) = \frac{|\nabla n_\sigma(\vec{r})|}{n_\sigma^{4/3}(\vec{r})}. \tag{2.36}$$

The gradient $s_\sigma(\vec{r})$ is used to improve the LDA exchange functional:

$$E_X^{GGA}(n(\vec{r})) = E_X^{LDA}(n(\vec{r})) - \sum_\sigma \int F(s_\sigma) n_\sigma^{4/3}(\vec{r}) d\vec{r}. \tag{2.37}$$

Here different classes of $F(s_\sigma)$ have been empirically realized based on the results of rare gas atoms from He to Rn with known exchange energies.

The GGA correlation functionals have even complicated analytical forms far away from any physical reasons. Different exchange and correlation functionals combine together to give a good approximation to E_{XC}, such as PZ [270], PW92 [271], PBE [272] and LYP [273]. XC functionals are always embedded in DFT software packages.

2.5.3 SCF Solution of the KS equation

2.5.3.1 Variational principle

To solve the KS equation (2.30), one needs to know the exact form of single electron wavefunction. One more approximation is expanding the single electron wavefunction on a particular basis set. Let $\phi_i(\vec{r})_{i=1\cdots N}$ be the a finite basis set. Expanding the single eletron wave function $\psi(\vec{r})$ on this basis leads to

$$\psi(\vec{r}) = \sum_{i=1}^{N} C_i \phi_i(\vec{r}). \tag{2.38}$$

Then variational principle is applied to minimize the expected eigenvalue of Equation (2.30). This can be achieved by substituting (2.38) into (2.30), followed by diagonalizing

the following set of secular equations:

$$\sum_{i=1}^{N} \left(H_{ij} - ES_{ij}\right) C_i = 0 \; \forall j = 1, \ldots, N, \tag{2.39}$$

where $H_{ij} = \langle \phi_i(\vec{r}) \left| H \right| \phi_j(\vec{r}) \rangle$ and $S_{ij} = \langle \phi_i(\vec{r}) | \phi_j(\vec{r}) \rangle$ are Hamintonian and overlap matrix elements respectively.

2.5.3.2 Periodic systems and Bloch theorem

In Kohn-Sham equation, the eigenvalue depends on the potential term $V(\vec{r})$ as shown in (2.30). Different boundary conditions (BC) apply for crystals, slabs, one-dimension wires and clusters. Generally, a periodic potential is expressed by $V(\vec{r}) = V(\vec{r}+\vec{R})$, where $\vec{R}$ is a translation vector of lattice, Due to the translational invariance of Hamiltonian, Bloch theorem claims that any single electron wave function is a product of a plane wave with a wave vector $\vec{k}$ and a periodic wave function.

$$\psi_{\vec{k}}(\vec{r}) = e^{i\vec{k}\cdot\vec{r}} u_{\vec{k}}(\vec{r}) \tag{2.40}$$

$$u_{\vec{k}}(\vec{r} + \vec{R}) = u_{\vec{k}}(\vec{r}) \tag{2.41}$$

$\vec{k}$ is also a good quantum number as l, and the Bloch function $\psi_{\vec{k}l}$ satisfies the orthonormality condition:

$$\left\langle \psi_{\vec{k}l} | \hat{H} | \psi_{\vec{k}'l'} \right\rangle = E_{l,\vec{k}} \delta_{\vec{k}\vec{k}'} \delta_{\lambda\lambda'}, \tag{2.42}$$

$$\left\langle \vec{k}, l | \vec{k}', l' \right\rangle = \delta_{\vec{k},\vec{k}'} \delta_{l,l'}. \tag{2.43}$$

Then the secular equations (2.39) need to be solved on each $\vec{k}$ point, as we shown in Subsection 2.5.3.3 and 2.5.3.4. The energy eigenvalue $E_{\vec{k}l}$ of each level l changes smoothly

as a function of $\vec{k}$, forms a curve along any direction of $\vec{k}$ in E-$\vec{k}$ space. All these curves together form energy bands. The structure of the energy bands is called band structure, which could be used to predict many electron-related properties of periodic systems.

2.5.3.3 Basis set: plane waves

Use of plane waves as the basis set in DFT periodic calculation is a straightforward choice. A periodic potential $V(\vec{r}) = V(\vec{r} + \vec{R})$ on lattice has discrete components in reciprocal space.

$$V(\vec{r}) = \sum_{\vec{G}} \hat{V}_{\vec{G}} e^{i\vec{G}\cdot\vec{r}}, \tag{2.44}$$

where $\hat{V}_{\vec{G}} = \frac{1}{\Omega}\int_{cell} V(\vec{r})e^{-i\vec{G}\vec{r}}$, and $\vec{G}$ is any reciprocal lattice vector defined by $\vec{G}\cdot\vec{R} = 2n\pi$. For $V(\vec{r}) = 0$ in the case of free electron gas, the solutions of Schrödinger equation are plane waves $\phi_{\vec{k}}(\vec{r}) = e^{i\vec{k}\vec{r}}/\sqrt{\Omega}$. To compose a basis set, the plane waves need be modulated to fulfill the requirement of (2.40) and (2.41). Or other words, due to the periodity of $u_{\vec{k}(\vec{r})}$, it can be expanded in reciprocal space:

$$u_{\vec{k}}(\vec{r}) = \sum_{\vec{G}} c_{\vec{k},\vec{G}} e^{i\vec{G}\cdot\vec{r}}. \tag{2.45}$$

Substitute (2.45) into (2.40), one can use plane waves as the basis set:

$$\psi_{\vec{k}}(\vec{r}) = \sum_{\vec{G}} c_{\vec{k}+\vec{G}} e^{i(\vec{k}+\vec{G})\cdot\vec{r}}. \tag{2.46}$$

Therefore the Hamiltonian and overlap matrix elements in (2.39) are:

$$\begin{aligned}\left\langle \vec{k}+\vec{G}\left|\hat{H}\right|\vec{k'}+\vec{G'}\right\rangle &= \left\langle \vec{k}+\vec{G}\left|-\frac{\nabla^2}{2m}\right|\vec{k'}+\vec{G'}\right\rangle + \left\langle \vec{k}+\vec{G}\left|V(\vec{r})\right|\vec{k'}+\vec{G'}\right\rangle \\ &= \frac{|\vec{k'}+\vec{G'}|^2}{2m}\left\langle \vec{k}+\vec{G}|\vec{k'}+\vec{G'}\right\rangle + \delta_{\vec{k},\vec{k'}}\left\langle \vec{k}+\vec{G}|V(\vec{r})|\vec{k'}+\vec{G'}\right\rangle, \\ &= \delta_{\vec{k},\vec{k'}}\cdot\delta_{\vec{G},\vec{G'}}\frac{|\vec{k'}+\vec{G'}|^2}{2m} + \tilde{V}(\vec{r})_{\vec{G'}-\vec{G}}\end{aligned} \tag{2.47}$$

where $\tilde{V}$ is a Fourier transform of $V(\vec{r})$ in reciprocal space. The overlap matrix is an identity matrix due to the orthonormality of plane waves:

$$S_{\vec{k}+\vec{G},\vec{k'}+\vec{G'}} = \left\langle \vec{k}+\vec{G}|\vec{k'}+\vec{G'}\right\rangle = \delta_{\vec{k},\vec{k'}}\cdot\delta_{\vec{G},\vec{G'}} \tag{2.48}$$

In (2.46), the number of $\vec{G}$ is still infinite. In practice, the maximum value of the kinetic energy of $\frac{1}{2}G^2$ is limited to a "cut-off" energy. The higher of cut-off energy implies a higher cost of computing resource, but more accurate results can be obtained.

The naive plane wave expansion suffers from convergence of electronic states due to the large number of plane waves. The reason is that the core electrons need to be described by large part of high energy plane waves. To reduce the number of plane waves, the core electrons can be expressed by atomic orbitals in the mixing orbital scheme, or replaced by a pseudopotential. The "norm-conserving pseudopotential" is constructed in the way to have the same value as the true potential outside a cut-off radius r_c. The "ultra-soft pseudopotential" was proposed to keep the pseudo potential as smooth as possible in the core region to further reduce the number of plane waves.

The plane wave expansion has several advantages. The plane waves are inherent orthonormal, thus the calculations of matrix elements and Fourier transformation are

convienient. The basis set is independent of number of atoms, and of no basis error needs to be corrected in calculating the reaction energy. The accuracy of calculations can be consistently improved by increasing the number of plane waves, given sufficient computing resource. However, to calculate the non-periodic system, the super-cell approach needs to be applied. The cost of plane waves method is proportional to the system volume rather than the number of atoms, thus the use of vacuum layer is expensive.

2.5.3.4 Basis set: linear combination of atomic orbitals (LCAO)

Another popular class of basis sets used is *linear combination of atomic orbitals* (*LCAO*). To satisfy the Bloch theorem, the atomic orbitals in LCAO is in the following forms:

$$\phi_{\vec{k}}^{\alpha,\vec{\tau}}(\vec{r}) = \frac{1}{\sqrt{N}} \sum_{\vec{R}} e^{i\vec{k}\cdot\vec{R}} \chi_\alpha(\vec{r} - \vec{R} - \vec{\tau}) \tag{2.49}$$

where the function $\chi_\alpha(\vec{r}-\vec{R}-\vec{\tau})$ is an atomic-like orbital localized on the atomic position labeled $\vec{\tau}$ within the unit cell labeled by $\vec{R}$, and α is the atomic orbital index (s, p_x, p_y, $\mathrm{p}_z \ldots$). Then the Hamiltonian matrix in secular equation (2.39) is block-diagonal:

$$\begin{aligned}
\left\langle \phi_{\vec{k}}^{\alpha,\vec{\tau}}(\vec{r}) | H | \phi_{\vec{k}'}^{\alpha',\vec{\tau}'}(\vec{r}) \right\rangle &= \sum_{\vec{R},\vec{R}'} \frac{1}{N} e^{i\vec{k}\cdot\vec{R}} \cdot e^{i\vec{k}'\cdot\vec{R}'} \left\langle \chi_\alpha(\vec{r} - \vec{R} - \vec{\tau}) \, | H | \, \chi_\alpha(\vec{r} - \vec{R}' - \vec{\tau}') \right\rangle \\
&= \sum_{\vec{R},\vec{R}'} \frac{1}{N} e^{i\vec{k}\cdot\vec{R}} \cdot e^{i\vec{k}'\cdot\vec{R}'} f_{\alpha\tau,\alpha'\tau'}(\vec{R} - \vec{R}') \\
&= \sum_{\vec{R}} \frac{1}{N} e^{-i(\vec{k}-\vec{k}')\cdot\vec{R}} \sum_{\vec{R}''} e^{-i\vec{k}'\cdot\vec{R}''} f_{\alpha\tau,\alpha'\tau'}(\vec{R}'') \\
&= \delta_{\vec{k},\vec{k}'+\vec{G}} \sum_{\vec{R}''} e^{-i\vec{k}'\cdot\vec{R}''} f_{\alpha\tau,\alpha'\tau'}(\vec{R}'')
\end{aligned} \tag{2.50}$$

The first term $\delta_{\vec{k},\vec{k}'+\vec{G}}$ in the last line indicates the hamiltonian element is non zero only when two $\vec{k}$ points differ by any reprocipal $\vec{G}$ vector. According to (2.49), the LCAO basis functions are manifestly G-periodic. By constraining the $\vec{k}$ in first Brillouin Zone (FBZ), the calculation of Hamiltonian elements is $\vec{k}$-decoupled. The second term in the last line of Equation (2.50) shows that the Hamiltonian elements vary smoothly with respect to $\vec{k}$. One can choose a few discrete $\vec{k}$ points in FBZ to calculate haminotonian and overlap elements. The hopping integrals $f_{\alpha\tau,\alpha'\tau'}(\vec{R''})$ depends on the displacement vector $\vec{R''}$ and symmetry. Only a few of the summed terms are non-zero.

The atomic orbitals in the basis sets can be numerical orbitals, gaussian functions or slater orbitals. The advantage of using linearly combined atomic orbitals set is that these orbitals have finite cut-off radii, and the calculation cost of hoping integrals between orbitals is lower compared to plane wave methods. The cost of calculation is sensitive to the number of atoms, not the system dimension. The linear scale of calculation $\hat{O}(N)$ is able to be implemented by LCAO method. The all-electron and pseudopotentials calculation are both possible. However, due to the incompleteness of the basis sets, when the reaction energies are calculated, one needs to correct the basis set superposition error (BSSE).

2.5.3.5 Evaluation of the electron density and total energy

Once the eigenstates of secular equations have been solved, the ground state electron density is a sum over occupied bands:

$$n_0(\vec{r}) = \sum_{l}^{Occupied} \int_{\vec{k}\in lstFBZ} |\psi_{\vec{k}l}|^2, \tag{2.51}$$

where FBZ denotes the first Brillouin Zone. Since $\psi_{\vec{k},l}$ varies smoothly along $\vec{k}$, only discrete $\vec{k}$ points are needed to be sampled. Different special $\vec{k}$ point sampling methods were proposed by Chadi and Cohen [274], or Monkhorst and Pack [275].

The total energy of the atomic system can be calculated from:

$$E[n_0(\vec{r})] = \sum_{l}^{Occupied} E_{l,\vec{k}} - \frac{1}{2}\int\int \frac{n(\vec{r})n(\vec{r'})}{|\vec{r}-\vec{r'}|} - \int V_{XC}(\vec{r})n_0(\vec{r}) + E_{xc}[n_0(\vec{r})] \tag{2.52}$$

2.5.3.6 Self-consistent field procedure to solve the Kohn-Sham equation

As shown in (2.30), the Kohn-Sham potential operator and the Kohn-Sham MOs are mutually dependent. An iterative procedure, namely self-consistent field (SCF) procedure is used to search the orbitals in 2.8. An initial guess of electron density may comes from a linear combination of atomic core potentials or reading from a previous running. The Kohn-Sham potential is calculated based on the initial electron density. The Kohn-Sham MOs are expanded on different basis sets, then solved by diagonalizing the secular equations 2.39 at discrete k-points. The new electron density and energy are updated, then compared with the previous cycle of running. If the difference in electron density (energy) between the two sequential cycles is lower than the predefined threshold, then the MOs are founded. Otherwise, the updated electron density will be fed into SCF loop to calculate the new Kohn-Sham. The updated electron density, potential can be mixed with the older ones within several cycles to accelerate the convergence.

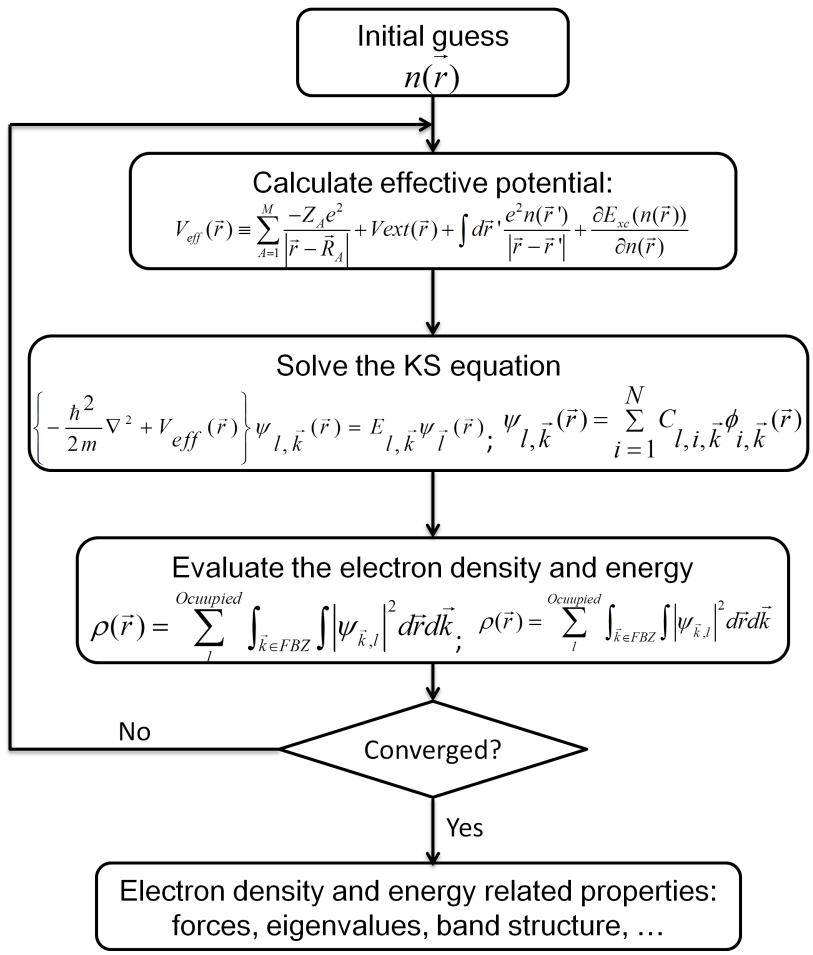

Figure 2.8: The self-consistent field (SCF) procedure to solve the Kohn-Sham equation.

2.5.4 Calculation of electron-related properties

Once the electronic structure of a system has been elucidated, one can perform other tasks to find the electron-related properties. Herein, we introduce three most important tasks in our project: transition state search, vibration frequencies calculation and STM image simulation.

2.5.4.1 Vibration frequencies calculation

In the energy range below 1 eV, vibrations are important components of optical or electron spectra. The incident beam includes photons or electrons, corresponding to infra-red/Raman spectrum or high resolution electron energy loss spectra, respectively. On metal surfaces, the absorption in this energy range is dominated by surface plasma belonging to electronic contribution. Whereas on semiconductors, the vibrations of lattice (phonons) and adsorbed molecules are responsible for the features in IR/Raman or HREELS spectra.

Applying harmonic oscillator approximation to the system, one can obtain harmonic vibrational frequencies from the matrix of Cartesian second derivatives of the system energy, namely Hessian matrix. For a cluster, the hessian matrix elements are:

$$H_{i,j} = \frac{\partial^2 E}{\partial q_i \partial q_j}, \tag{2.53}$$

where q_i is any Cartesian coordinate of a system with N atoms, $0 < i < 3N$. In periodic

systems, the infinite Hessian matrix can be Fourier transformed into:

$$H_{i,j}^{\vec{k}} = \frac{1}{\Omega} \sum_{\vec{R}} H_{i,j+\vec{R}e^{i\vec{k}\cdot\vec{R}}}. \tag{2.54}$$

In IR and many other spectra, the most important part is Hessian matrix at $\vec{k} = 0$ (Γ point). According to the harmonic approximation, the vibrational frequencies are square root eigenvalue of mass weighted Hessian matrix, and the normal modes are eigenvectors of mass weighted Hessian matrix:

$$F_{i,j} = \frac{H_{i,j}}{\sqrt{m_i m_j}}. \tag{2.55}$$

The vibration intensities are obtained from the atomic polar tensors, which are called by Born effective charges:

$$A_{i,j} = \frac{\delta E}{\delta q_i \delta \vec{\mu}_j}. \tag{2.56}$$

The intensity of any mode could be obtained from a square of all transition moments of this mode and expressed in terms of the A matrix and eigenvectors of the mass-weighted Hessian, F':

$$I_i = \left(\sum_{j,k} F'_{i,j} A_{j,k} \right)^2. \tag{2.57}$$

The incident electrons have different interaction mechanisms with the system compared to photons. When the molecules adsorbed on semiconductor surfaces, the broken symmetry and the induced dipoles also alter the intensities. Therefore, the calculated relative intensities of vibrational frequencies for a system may not perfectly match with the experimental HREELS data. However, the vibration frequencies are predictable with less errors, and can be used to interpret the binding mechanism and other properties.

2.5.4.2 STM image simulation

Simulation of STM images is usually straightforward in most of DFT calculation. The electron density are usually calculated and stored by DFT softwares to compute any other properties. As deduced in section 2.2.3, the constant current STM image presents the contour map of local density of states, which can be directly extracted from electronic density $\rho(\vec{r})$. One thing needs to know is that many DFT packages only calculate part of energy bands beyond the Fermi level. Thus the empty state STM images with large biases may be incorrect.

2.5.4.3 Transition state search

There are many methods to search transition states, including linear dragging, synchronous transit, nudged elastic band, string method, dimer method and others. The linear dragging and synchronous transit, which we employed in this project, are introduced in the following.

The linear dragging method relaxes a series of structures interpolated between the reactant and the product. By freezing one key structural parameter during relaxations, the transition state is assigned to the one with the highest energy after relaxation. This method can be manually performed by setting several geometric optimization tasks with constraints.

In CASTEP, the synchronous transit method (complete LST/QST) is used to find transition states [276]. From reactants to products, the synchronous transit method linearly interpolates a reaction pathway. The linear synchronous transit (LST) method first estimates a transition state by finding the highest point along this pathway like

linear dragging method. A constrained conjugated gradient method (constrained CG) is used to relax this highest point when retaining its internal coordinates. After relaxation, a new minima point is obtained as the intermediate point, and it gives an lower energetic bound of the real transition state. The quadratic synchronous transit (QST) method is employed to search for a highest point along a parabola connecting the reactant, the above intermediate point and the product. The new highest point gives an improved upper bound of transition state energy. This point can be fed into constrained CG/QST loops, until the upper and lower point overlap. The overlapping point is the transition state which we look for.

2.5.5 Calculation softwares

CASTEP [277] program packages and SIESTA (2.0.2 and 3.0) [278] were employed in the current project. Both methods are based on density functional theory (DFT) (section 2.5.1) despite their different methods of solving the KS equation and other implementations.

2.5.5.1 Siesta

Siesta is an open source tool for large-scale DFT calculations. Siesta stands for "Spanish Initiative for Electronic Simulations with Thousands of Atoms", and is "both a method and its computer program implementation, to perform electronic structure calculations and ab initio molecular dynamics simulations of molecules and solids [278]." Siesta uses linear combination of numerical atomic orbitals (LCAO). Using norm conserving pseudopotentials in fully nonlocal Kleinman-Bylander [279] form and multi-zeta atom-like orbitals, the eigenvalues could be solved by either Rayleigh-Ritz eigenstate

method or order-N method. The pseudopotentials, however not offered in package, need to be downloaded from web sites or generated using ab-initio program ATOM. The critical parameters of norm conserving are the cut-off radii for orbitals,. They need to be carefully tested, to ensure the good transferability and reproducibility in calculations. The electronic exchange-correlation (XC) effect is treated in LDA or GGA approximation. XC functionals include Perdew-Zunger (PZ) [270], Perdew-Wang (PW92) [271], Perdew-Burke-Ernzerhof (PBE) [272], revised PBE [272], Becke exchange [280] and Lee-Yang-Parr corelation (LYP) functionals [273]. The hybrid functionals can be manually fed by mixing the above functionals according to the reported portion.

Siesta automatically judges the input structures as the bulk, surface, one dimensional wires or cluster based on the spacial isolation between the super cells. Siesta can calculate routine properties like energy, atomic forces, electron density, Mulliken charge population and band structures. Siesta has several geometric relaxation method. The conjugated gradient method is used in our project. STM images can be simulated by applying Tersoff-Hamann approximations [228]. The vibrations of adsorbed molecules on surface is calculated at Γ point. The vibrational frequencies are calculated by diagnosing the force constant matrix obtained by a finite displacement method. Another useful utility in Siesta package is plotting COOP/COHP curves, which provides the detailed binding information between atoms or atomic fragments.

2.5.5.2 CASTEP

CASTEP is a DFT calculation program in Materials Studio (version 5.0.0.0) of Accelrys Inc [277]. CASTEP uses plane waves and norm-conserving/soft pseudopotentials. Like Siesta, CASTEP treats the XC effect with LDA or GGA approximations. Most of XC functionals are available in CASTEP. CASTEP is capable of calculating the energy,

electronic properties like density of states, band structures, elastic properties and charge population. Broyden-Fletcher-Goldfarb-Shanno method was used to relax the adsorption structures. CASTEP can also simulate STM images, vibrational frequencies (IR and Raman), NMR spectra, phonon spectra, elastic properties and others. With the visualizer in Materials Studio, it is convenient to create and visualize structural models and related spacial distributions.

2.5.6 Computational procedures

In this project, DFT calculations are employed to explore adsorption, diffusion and dissociation of CO and NO molecules on Ge(100), or to simulate the adsorption structures of heterocycles to interpret the STM and HREELS results. Here are some parameters we used in calculation.

Substrate model To simulate the Ge(100) surface, we use slab models, which consist of six or eight layers of Ge atoms. The six-layer model is sufficient to describe the energy and stable adsorption structure. However, to correctly describe the band structure of Ge(100), the slab should be thicker than seven layers [169]. The bottom most two layers are frozen, whereas other layers are allowed to relax during geometric optimization.

Lattice constant The lattice constant used in calculation was obtained according to relaxed bulk model under same calculation parameters (kinetic energy cut-off, density of k-grid, converging criteria, etc). Generally, a relative error of 1∼2% in lattice constants compared to experimental values was reported for GGA-PBE approximation.

Vacuum layer The vacuum layer should be sufficient to separate the interaction between slabs in z-direction, eliminating the dipole effect. In SIESTA, the vacuum can be as thick as possible due to fast decaying and infinite radii of used atomic orbitals. In contrast, CASTEP, which based on plane waves, has to consider dipole effect as well as the calculation cost. In our project, the thickness of vacuum layer was set to 15 Å after test.

Transition state search Transition state search was not implemented in SIESTA 2.0, a constrained minimization method can be manually used instead. In CASTEP, the LST/QST method was employed to find the transition states.

More details of calculations will described in computational sections in Chapter 3∼5.

Chapter 3

Imaging molecular orbitals of pyridazine datively bonded on Ge(100) at room temperature

3.1 Introduction

Directly imaging orbitals of individual organic molecules on particular surfaces by scanning tunneling microscope (STM) is essential for the design and application of molecular devices [237]. As STM relies on the tunneling current between tip apex and conductive substrate, the investigations were limited to molecules adsorbed on metal or semiconductor surfaces. Unfortunately, on these surfaces, the electronic properties of adsorbed molecules are perturbed by the surface states, failing to present their undistorted orbitals under STM. To resolve a molecular orbital, it is crucial to electronically decouple molecules from the substrate [226]. For example, Repp et al. demonstrated that by depositing several monolayers of insulating NaCl on Cu(111) and Cu(100) [235, 238], orbitals of pentacene can be resolved without perturbation from Cu substrate. Graphene [281] and iron(II) phthalocyanine [242] were also used as the screening layer to isolate the metal surfaces and adsorbed molecules.

However, as a double edged sword, these screening layers are chemically inert towards the adsorbed molecules. The adsorbates are usually highly mobile on the screening layers

due to the weak interaction, making further measurements and manipulations inconvenient. Thus low temperature and/or self-assembling techniques are usually required to immobilize the adsorbed molecules [236,238,242,246,247,282]. In addition, the residence time of tunneling electrons in the molecule and screening layer increases compared to that of bared metal surfaces. This induces dynamic charge distribution, which significantly alters the energy levels of molecular orbitals [245]. These problems could be solved if one finds a bonding system in which the molecules can be chemically bound on pristine substrate without insulating surface, at the same time the molecules could be electronically decoupled from from substrate.

Nevertheless, most of these orbital resolved STM images were recorded on metal surfaces covered by insulating layers. The substrate for imaging molecular orbitals by STM was not expanded to clean semiconductor surfaces, which are equally important considering the possibility of incorporating modern semiconductor microelectronic techniques into molecular devices. The strong surface states from dangling bonds on clean semiconductor surfaces could appear as background tunneling resonance, interfering the molecular feature. Successful examples were only found on SiC which has wide band gap [283] or hydrogen saturated Si(100) [247]. Lacking of effective methods to epitaxially grow insulating layers, resolving orbitals on other semiconductor surfaces remains a challenge. In addition, the surface atoms with dangling bonds from clean semiconductor surfaces are highly reactive. They could covalently binds the molecules, especially those planar molecules, significantly altering their electronic properties by destroying the pristine molecular orbitals. Thus, the binding mechanism of molecules need to be carefully designed, to avoid perturbation of orbitals of adsorbed molecules. Herein we demonstrate that datively bound aromatic heterocycles (pyridazine) on Ge(100) could be resolved due to its self-decoupling from surface states with a stand-up configuration.

The dative bonds on one hand, chemically anchor the molecules, facilitating the future manipulations. On the other hand, the dative bonds between N atom and surface Ge atom do not significantly affect the molecule orbitals.

Directly imaging orbitals of single molecules on semiconductor surfaces will also have a significant contribution in methodology of surface chemistry of semiconductors. Because reconstructed semiconductor surfaces have complex geometric and electronic structures, there may be multiple adsorbing sites and binding mechanisms when organic molecules are adsorbed on semiconductor surfaces. Based on limited resolution of traditional STM image, one can only deduce the binding mechanism by locating the adsorbing sites, capturing the rough profiles of molecules under different biases and/or comparing the images with theoretical simulations. But these deductions often lack certainties, suffering from a poor resolution of STM images. In fact, surface reactions like cycloaddition, dative bonding and dissociation involve the evolutions of molecular orbitals near Fermi level, such as elimination of π bonds or lone electron pairs. These evolutions can be directly monitored by STM, once orbitals or molecules could be resolved by STM. In assistance with theoretical simulation, this technique can reliably determine the adsorption products as well as the reaction mechanisms. In this study, we show orbital resolved STM technique can convincingly identify different adsorptional structures of pyridazine molecules on Ge(100). The STM results were in excellent agreement with high resolution electron energy loss spectroscopy (HREELS) data.

3.2 Experimental and Computational details

The STM and HREELS experiments were performed in an ultra high vacuum chamber with a base pressure of 1×10^{-8} Pa. The chamber is equipped with an Omicron

variable temperature STM and a high-resolution electron energy loss spectrometer (LK-3000, LK Technologies, Bloomington, IN). To resistively anneal the sample and cool it to 110 K, an OMICRON UHV standard sample heater stage was further mounted on a liquid nitrogen cooled Dewar type sample holder. The sample used in our experiments was cut from a n-doped, single-side polished Ge(100) wafer with a resistivity of 1-2 Ω·cm and a size of 12 mm×2 mm×0.5 mm. The clean Ge(100) surface was prepared by several cycles of 1000 V Ar^+ sputtering and flashing to 1000 K. Pyridazine (99%, Sigma-Aldrich Chemical) was purified via six freeze-pump-thaw cycles before being dosed onto the Ge(100) surface.

The STM tips were made from electrochemically etched tungsten wires. To achieve subatomic resolution, the tip apex was further sharpened by several times of Ar^+ sputtering and pulses, until a satisfied resolution was achieved. In STM experiments, the dosing was in-situ during STM scanning, and the coverage was directly monitored by STM. In HREELS experiments, an electron beam with an energy of 6.0 eV impinges on the Ge(100) surface at an incident angle of 60° with a resolution of 60 cm^{-1} (full width at half maximum). The sample was facing to the dosing tube and about 5 centimeters away from the tube aperture. The exposure was recorded in Langmuirs (1 Langmuir = 10^{-6} Torr·s) without calibration of ion gauge sensitivity.

The DFT calculations were performed using CASTEP in Materials Studio (Version 5.5) of Accelrys [277]. The Ge(100) surface was simulated by a c(4×2) slab model of six layers, including a surface layer with four dimers, three middle layers and two frozen bottom layers. The generalized gradient approximation (GGA) with Perdew-Burke-Ernzerhof (PBE) parameterizations [272] was used to estimate the exchange-correlation effect. Although GGA approximation systematically underestimates the band gap of

semiconductors, but for molecules in our discussion GGA still offers reliable PDOS. The kinetic energy cut-off was 330 eV. A 2×4×1 Monkhorst-Pack grid was used for Brillouin Zone sampling [275]. The same grid was used to calculate the density of states. The converge criteria for force in geometric optimization was 0.02 eV/Å. A thermal smearing of 0.01 eV was used to accelerate the SCF convergence. STM images were simulated by applying the Tersof-Hamann approximation [228], which is implemented in CASTEP code.

3.3 Results and discussion

Figures 3.1A-C show sequential STM images of pyridazine on Ge(100) during dosing. The straight stripes and zig-zag chains in Figure 3.1A refer to the (2×1), p(2×2) and c(4×2) reconstructions of Ge(100), respectively. A bright spot appearing at the top left corner of Figure 3.1A indicates an adsorbed pyridazine molecule. Further dosing of pyridazine on Ge(100) produces more similar spots in Figures 3.1B to C. Several spots that emerge in Figure 3.1B, but disappear in Figure 3.1C during the scanning. Figure 3.1B and 3.1C also display some incomplete features, indicating that pyridazine molecules undergo a mobile precursor state before being bound to Ge(100).

The majority type of adsorbed features observed in Figure 3.1A–C are marked by the yellow rectangle in Figure 3.1C. Unlike the simple protrusions usually appearing in conventional STM images, here molecules appear as “flowers” with three lobes. Two lobes are identical and larger than the third one, rendering the flower asymmetric. We used to image elliptical spot without any nodal planes at same scanning condition using a normal tungsten tip. The flower like features were obtained when tip apex is sharp enough.

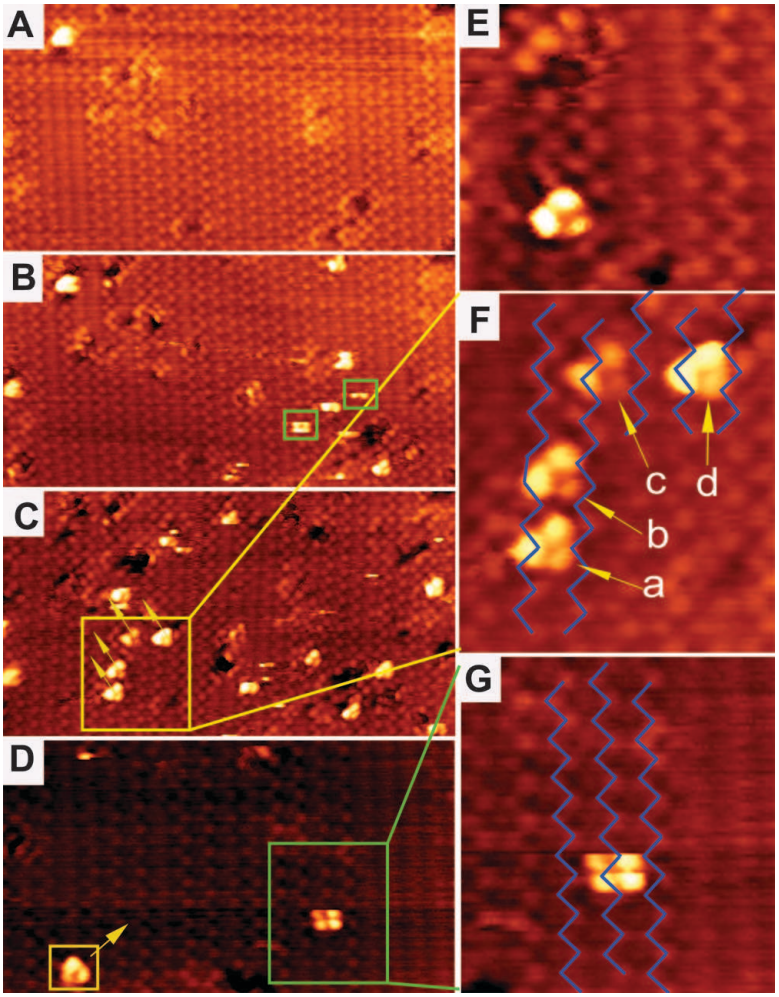

Figure 3.1: Constant current STM images of pyridazine adsorbed on a Ge(100) surface. (**A** to **C**) 25×20 nm^2 sequential STM images of pyridazine molecules adsorbed on the surface. Bias: -2.0 V, current: 300 pA. The yellow arrows mark the uniform orientation of adsorbing features. (**D**) 15×10 nm^2 STM image of other two features. The yellow rectangle and arrow refer to the similar features in Figure 3.1D but with different orientations. (**E**) Zooming-in of features in Figure 3.1C at a bias of -0.5 V. (**F**) Zooming-in of features in green rectangle in Figure 3.1C at a bias of -2.0 V. (**G**) Zooming-in of features in green rectangle in Figure 3.1D at a bias of -2.0 V. The blue zig-zag chains in (**F**) and (**G**) refer to upper dimer atoms of Ge(100).

These flowers have an uniform azimuth angle relative to dimer rows during the scanning (marked by yellow arrows in Figure 3.1C). After carefully checking the scanning conditions, it was found that this uniform orientation is independent of tip scanning direction, biases applied and dimer row direction of the substrate (in Figure 3.2). However, the orientation rotates by 90° in a different scanning area (yellow rectangle and arrow in Figure 3.1D). It is suspected that some impurity bulges or defects in nanoscale on surface accumulating charges might be responsible for inducing the orderly orientation of pyridazine. Further investigation is interesting and currently under way. Figure 3.1F presents a zoomed-in image of four adsorbed molecules in Figure 3.1C. By sketching the Ge(100) upper dimer atoms, the center of feature is located between two nearest dimer atoms in adjacent dimer rows as shown by the blue zig-zag chains. More specifically, molecule **a** in Figure 3.1F sits on between two upper dimer atoms, molecule **b** between an upper atom and an lower atom, and molecules **c** and **d** between two lower dimer atoms. These different locations indicate that the binding sites are insensitive to the dimer buckling direction. Figure 3.1E shows a filled state image at bias of -0.5 V, the flower-like feature is similar to that in Figure 3.1C, indicating that image may be insensitive to biases between -2 and 0 V.

Another binding feature is marked by the green rectangle in Figure 3.1D. This feature seems to be mobile and less stable on the surface, and we observed several incomplete ones marked by the green rectangles in Figures 3.1B and 3.1D. This feature has four symmetric lobes separated by a cross, clearly distinguishing itself from the three-lobes pattern. A zoomed-in of this feature in Figure 3.1G shows the center of the cross is on the bridge position of a dimer.

To interpret the STM images and gain insight into the binding mechanism, we per-

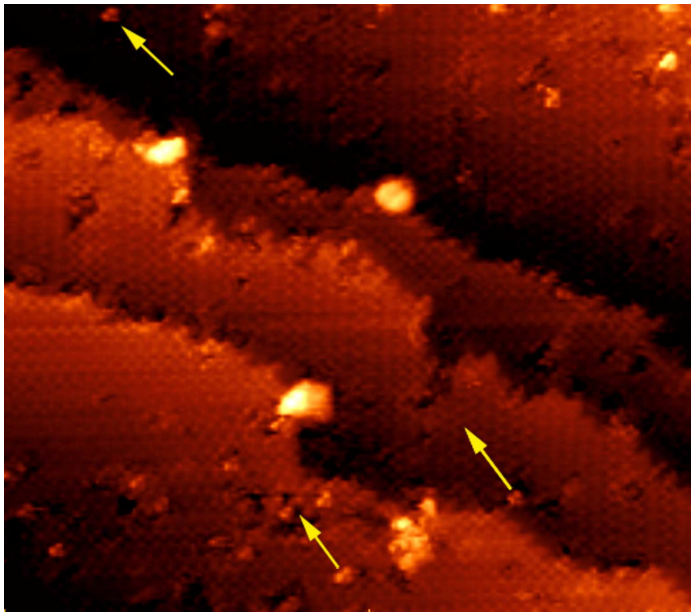

Figure 3.2: 30×30 nm^2 STM images of pyridazine adsorbed on different terraces of Ge(100) with same orientation. Bias: -2.0V; Current: 0.3 nA. The yellow arrows mark the pyridazine as well as their orientations

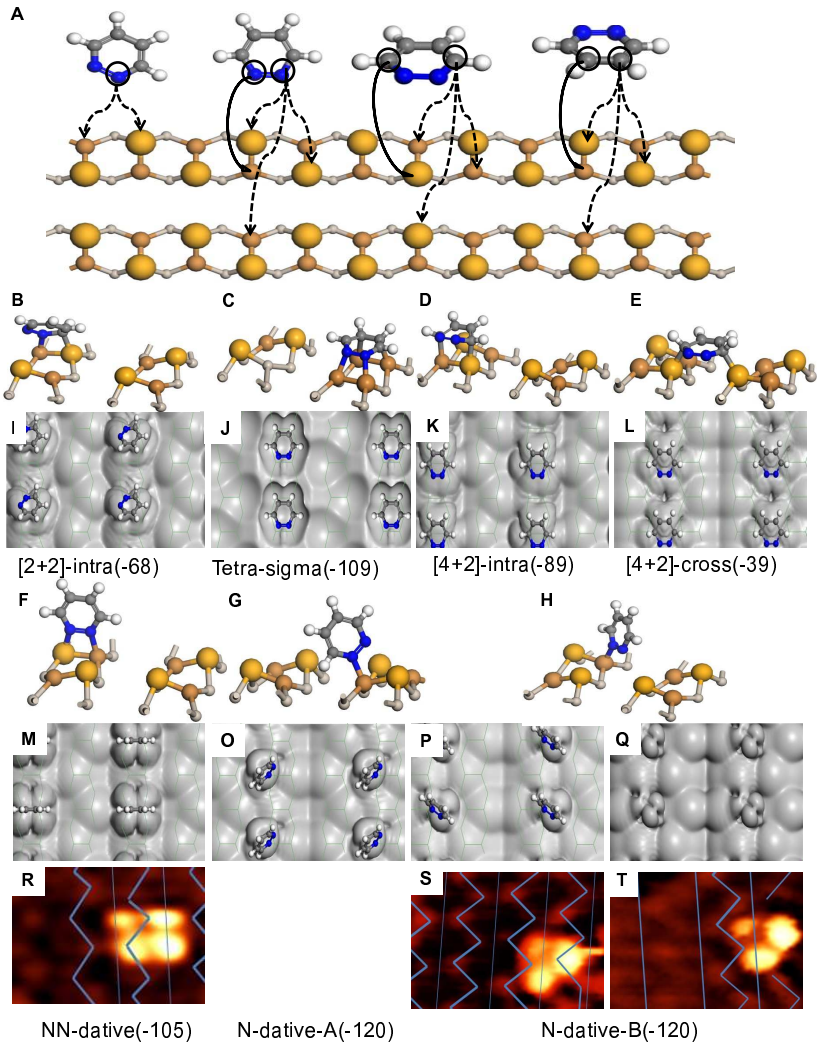

Figure 3.3: Theoretically predicted products and simulated STM images. (**A**) Possible bonding mechanisms, including N-dative, NN-double dative, [4+2] cycloaddition via two C=C bonds, [2+2] cycloaddition via C=C bond. (**B** to **H**) Stable adsorption structures after geometric optimization. Their simulated STM images (**I** to **P**, bias -2.0 V, isovalue 1×10^{-4}), model names and energies relative to the interaction free system are given below them respectively. (**Q**) Simulated STM image of structure **O** at a bias of -0.5V, isovalue:1×10^{-4}). (**R**, **S**, **T**) Experimental STM images at the biases of -2.0 V, -2.0 V and -0.5 V, adapted from Figure 3.1G, 3.1F, 3.1E, respectively. The blue zig-zag chains sketch the upper atom on each dimer. The straight lines presents the dimer troughs.

formed DFT calculations and STM simulations. Figure 3.3A shows the possible reaction pathways of pyridazine on Ge(100), including N-dative, NN-double dative, [4+2]-cycloadditions, [2+2]-cycloadditions. Pyridazine molecules may form single dative bonds with the upper or the lower dimer atom. For the bidentate bindings inclusive of NN-double dative, [4+2]-cycloadditions, [2+2]-cycloadditions, the bonding sites can be single dimer (intradimer), two dimer atoms from two neighboring dimers in a dimer row (interdimer) or two neighboring dimers from adjacent dimer rows (crossdimer). After geometric optimization, seven stable structures(Figure 3.3B-H) were obtained. The three most stable configurations are NN-dative (-105 kJ/mol, Figure 3.3F), N-dative-A/B(-120 kJ/mol, Figure 3.3G/H) and tetra-sigma (-106 kJ/mol, Figure 3.3C). The calculated formation energies indicate that the [2+2]-cycloaddition of C=C bond is energetically unfavorable. The binding strength of [4+2]-cycloadditions depending on the binding sites, varies from weak (-39 kJ/mol, Figure 3.3E) in the cross-dimer model to medium (-89 kJ/mol, Figure 3.3D) in intra-dimer model. In case of [4+2] interdimer adsorption, the product transits to the C,N-[2+2] intradimer cycloaddition (Figure 3.3B). In Figure 3.3E, four σ bonds on two dimers with large energy (-109kJ/mol).

In conventional STM images with low resolution, the binding mechanism is mainly proposed based on the location of adsorbate features. For example, the three-lobe features in Figure 3.1C might be assigned to either N-dative-A/B or a cross-dimer product (Figure 3.3E) because in these two configurations pyridazine is in the troughs between dimer rows. If lacking of orbital resolution, these two structures in STM would be indistinguishable due to similar profiles without nodal planes. It is also difficult to assign the four-lobe feature to any of on-dimer-row products (Figure 3.3B, 3.3C, 3.3D, 3.3F) only by judging from the adsorbing location. However, based on our molecular orbital resolved STM images, it is possible to convincingly identify the adsorption structures.

We find that only NN-dative model in Figure 3.3F can present the symmetric four-lobe feature in STM images. Although two [4+2]-products in Figure 3.3E and 3.3E may have four lobes, they are asymmetric and the orientation of their nodal cross differs from the experimental result by 45°. Similarly, only the simulated STM image (Figure 3.3P) from N-dative-B product (Figure 3.3H) can match the observed three-lobe feature (Figure 3.1C, 2Q), in shape, orientation and location. The high resolution also guarantees the discrimination between N-dative-A and N-dative-B even they only differ in the azimuth angle of pyridazine. Figure 3.3Q show the simulated STM image of N-dative-B at a bias of -0.5 eV, in good agreement with the experimental observation in Figure 3.3T. Thus, based on our STM images, we conclude that N-dative-B and NN-dative bonding are two stable adsorption configurations.

Since the transition between NN-dative and N-dative-B only involves an additional dative bonding formation/elimnation, such a conversion would be facile at room temperature. Thus N-dative-B in Figure 3.3H as the most stable configuration, is dominant in STM images. NN-dative in Figure 3.3F is less stable and captured as the four-lobe features by STM. It should also be noted that 3.3G and 3.3H are both N-dative bonding configurations, with the same azimuth angle relative to dimer rows direction. They differs from each other by a rotation of N-Ge bond by 180 °. Although these two states are degenerate (-120 kJ/mol), experimentally only type 3.3O was observed during STM scanning. Our calculations did not consider the tip-induced external electric field, which likely accounts for the preferability of 1H over 1G. Theoretical investigation of the stabilities of 3.3G and 3.3H under external electric field is interesting but beyond the scope of this study.

To understand which orbital(s) contribute to the observed STM features, we plotted

the density of states (DOS) curves of the pyridazine/substrate model. The black and red curves refer to DOS of pyridazine/slab model and partial DOS of pyridazine fragment, respectively. The states between -2 V and 0 V which contribute to filled state STM images, are mainly from the Ge(100) substrate. There are a few tiny ripples on pyridazine PDOS curves in this range. To resolve the contribution from pyridazine and to screen the dominating surface states, we employed another pyridazine/Ge_9H_{12} cluster model. The similar adsorption structure of N-dative-B is shown in Figure 3.4C. The PDOS curve of pyridazine of this cluster model (Figure 3.4A, blue curve) well reproduces that of slab model (red curve). By comparing the characteristic peaks in PDOS of the cluster model and DOS of free pyridazine (Figure 3.4A, cyan Curve), most orbitals of pyridazine are red-shifted by about 2.7 eV after adsorption. This is owing to the electron transfer from pyridazine to the substrate via dative bonding, decreasing the energy of molecular orbitals. The lowest unoccupied molecular orbital (LUMO) of free pyridazine (Figure 3.4O) at 3.8 eV, approaches the Fermi level after adsorption. Simultaneously, the highest occupied molecular orbital (HOMO, Figure 3.4N), consisting of lone electron pairs of N and delocalized π, falls below -2 V, is not responsible for the flower-like features in the filled state STM images. There are only six tiny peaks from the pyridazine in the range between -2 V and 0 V. These were confirmed by comparing the orbital profiles of the cluster model (3.4D-I) and free pyridazine (3.4M-P).

Figures 3.4D to 3.4I show that these six orbitals are analogous in shape. All of them have two larger lobes separated by the molecular ring plane, as well as another pair of smaller lobes. Compared with the orbitals of free pyridazine, these six orbitals look like the LUMO (Figure 3.4O) of free pyridazine, although the electron density at two C=C π bonds in the LUMO are inequivalent. The π bond connecting the binding N atom shrinks into one lobe near Fermi level, possibly due to the stronger electron transferring

to substrate than that of the further double bond from the binding N. Because of their similarity in shape, the STM images at biases of -2 V and -0.5 V are nearly the same, as shown in Figure 3.3S and 3.3T.

Similarly, Figure 3.4B shows DOS (black curve) and PDOS of pyridazine (red) of pyridazine/substrate system, PDOS of pyridazine (blue) in NN-dative cluster model in Figure 3.4J and DOS of free pyridazine (cyan). Comparison between PDOS curve of cluster model and DOS of free molecule demonstrates that the energy levels of pyridazine orbitals are generally lowered by 3.4 eV after adsorption. The larger shift than that of N-dative-B is attributable to the more effective electron transfer from pyridazine to the substrate via the double dative bonds. This shift brings the LUMO of pyridazine to the Fermi level after adsorption. On the other hand, the double dative bonds eliminate the surface dimer dangling bonds, thus preventing the possible coupling between molecular orbitals and surface states due to dangling bonds. Therefore, only one orbital (Figure 3.4K), previously as the LUMO of pyridazine, was found to produce the four-lobe features between -2 and 0 V. Indeed, we observed the excellent match between Figure 3.4K and Figure 3.4M, both in shape and orientation of nodal cross. Although we failed to obtain the STM images of NN-dative at any bias rather than -2.0 V due to its instability, we predict that the same four-lobe features likely appear at any other bias between -2 V between 0 V.

To validate the adsorption structures proposed from our orbital resolved STM images, high resolution EELS was employed to confirm the binding mechanisms. Figure 3.5 shows the EELS peaks of pyridazine adsorbed on Ge(100) at different coverage and temperature. The vibration frequencies and assignments are summerized in Table 3.1. The curve obtained after exposing 0.5 L (1 L = 1 Langmuir = 10^{-6} Torr·s) at 100 K

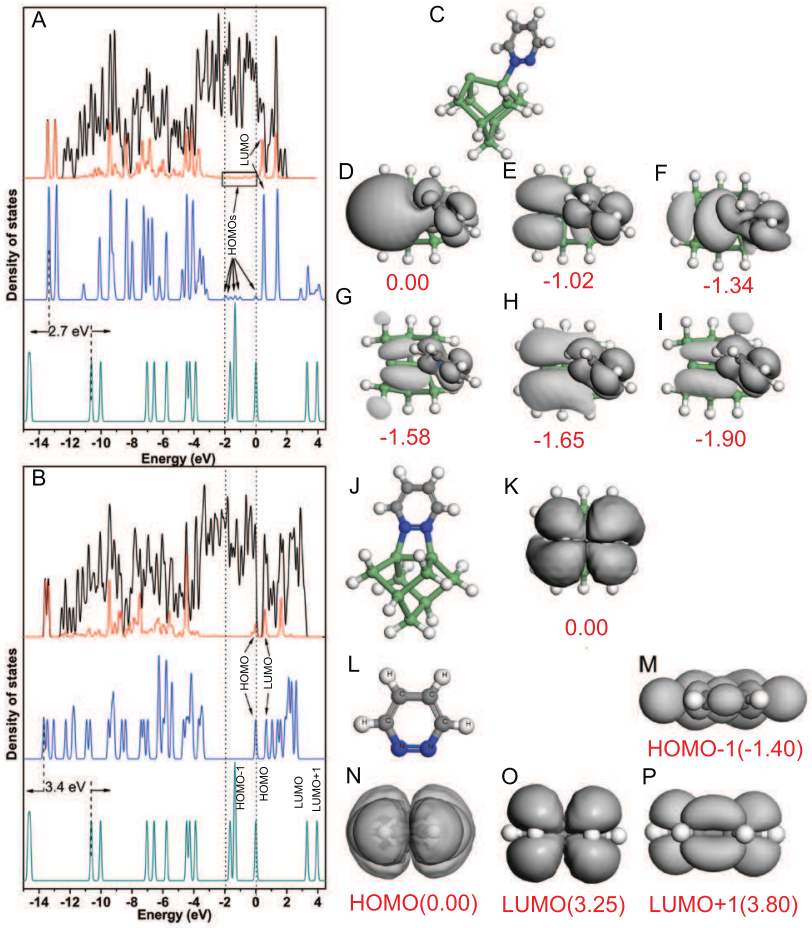

Figure 3.4: Simulated density of states (DOS) and orbitals of N-dative-B and NN-dative configurations. (**A**) Curves in N-dative-B configuration (from top to bottom). Black: DOS of the slab model; Red: Partial DOS (PDOS) of the pyridazine moiety in the slab model; Blue: PDOS of the pyridazine moiety in the cluster model in **C**; Cyan: PDOS of free pyridazine molecule. (**B**): Curves in NN-dative configuration (from top to bottom). Black: DOS of the slab model; Red: PDOS of the pyridazine moiety in the slab model; Blue: PDOS of the pyridazine moiety in the cluster model as shown in **J**; Cyan: DOS of the free pyridazine molecule. (**C**): Ge_9H_{12} cluster model of N-dative configuration, and its molecular orbitals between -2.0∼0 eV (**D**∼**I**). (**J**): Ge_9H_{12} cluster model of NN-dative configuration, and its molecular orbitals between -2.0∼0 eV (**K**). (**L**): Free pyridazine molecule, and its frontier orbitals (**M**∼**P**). The eigenvalues listed below these orbitals are in the unit of electron volts. All energies are relative to the Fermi level as zero. The isovalue to draw the orbitals is 1×10^{-4}.

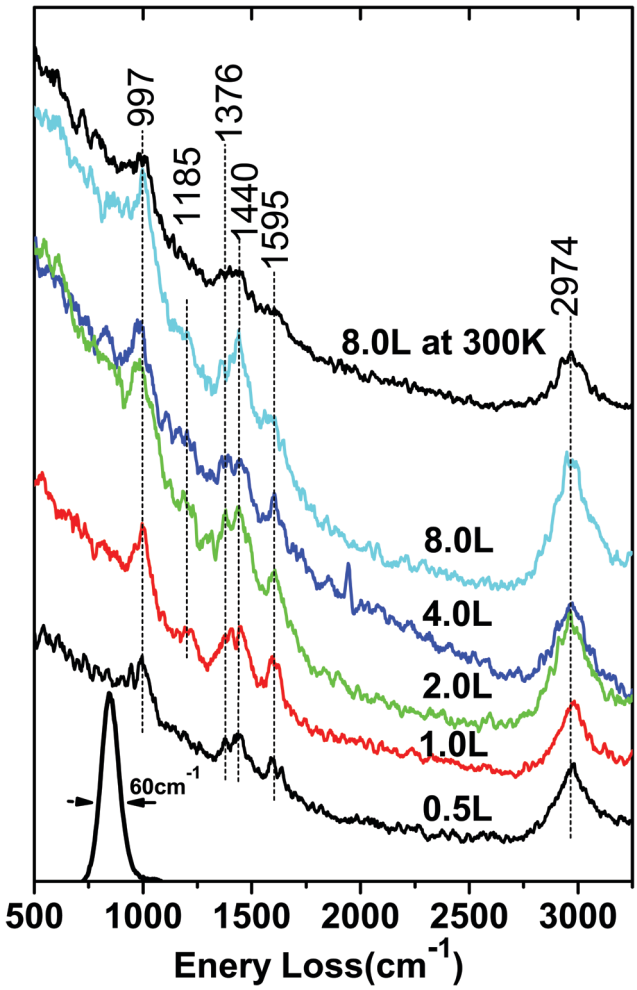

Figure 3.5: HREELS spectra of pyridazine adsorbed on Ge(100) at liquid nitrogen temperature and 300K. The full width at half maximum (FWHM) of the elastic peak is 60 cm^{-1}.

and 8 L at 300 K correspond to the chemisorption state, in which pyridazine is in the same binding states as we observed in STM images. Compared to the physisorption curves (1.0, 2.0, 4.0, 8.0 L), five distinct peaks are retained with little shift. Specifically, the peaks around 997 and 1595 cm^{-1} in these curves correspond to the C=C stretching, indicating that the C=C bonds are not reacted after adsorption. The single peak at 2974 cm^{-1} at 0.5 L suggests there is no sp^3 C-H bond. Otherwise it would produce an extra peak below 2960 cm^{-1}. Furthermore, the peak around 1376 cm^{-1} can be assigned to the sp^2 C-H scissoring mixed with CN stretching; the peak at 1440 cm^{-1} is related to sp^2 C-H scissoring. The last peak 1185 cm^{-1} assigned to C=N and C=C stretching, only appears in physisorption curves. This is in agreement with the previous study, which reported that this peak is enhanced for pyridazine molecules in condensed state, but disappears in monomolecular state in IR spectrum [284]. Due to the limited resolution, we did not assign any peak for N-Ge bonds which would have a stretching frequency below 1000 cm^{-1}. These six peaks exist only when the pyridazine aromatic ring is retained, thus the most likely binding mechanism are N-dative-A/B bonding or NN-double dative bonding. The EELS results firmly support the bonding structures identified from our STM images.

In conclusion, we demonstrated for the first time that orbitals of organic molecules on clean semiconductor surfaces can be directly imaged by STM. The surface states from the substrate do not strongly couple with molecules orbitals, due to a stand-up configuration of the molecules via dative bonding. The dative bonds also anchor pyridazine with good immobility and stability, avoiding the complex surface preparation or lower temperature technique to achieve the orbital resolution. This study demonstrated that the adsorption sites, binding configurations and the orientation of molecules can be reliably determined in orbital resolved STM images. Our work will inspire the applications of orbital resolved STM in molecular devices as well as in surface chemistry of semiconductors.

Table 3.1: Vibrational frequencies (cm^{-1}) and their assignments for physisorbed and chemisorbed pyridazine on the Ge(100) surface.

Vibration modes	Solid IR spectrum[a]	HREELS spectra		Calculated peaks	
		Physisorption	Chemisorption	Physisorption	Chemisorption
$\nu(C_4{=}C_5)+\delta(CH)_s+\nu(NN)$	1074	997	997	1058	1103
$\nu(CN)_s+\nu(CC)_s$	1160	1185		1168	
$\delta(CH)_{as}+\nu(CN)$	1415	1376	1376	1387	1433
$\delta(CH)_s+\nu(CC)+\nu(NN)$	1413	1440	1440	1427	1467
$\nu(C_4{=}C_5)+\delta(CH)_s$	1570	1595	1595	1554	1535
$\nu(CH)$	3057	2974	2974	3138	3075

[a] from reference [284].

Chapter 4

Unique geometric and electronic structure of CO adsorbed on Ge(100): A DFT study

4.1 Introduction

The study of CO adsorption on semiconductor surfaces, particularly on Ge surfaces, is of great importance in catalysis and future microelectronics. Ge is used as an additive to transition metal/metal oxide catalysts for CO oxidation [285], olefin reforming [5], n-hexane transformation [5, 219] and fuel cell catalysis [286, 287]. In these processes, the Ge additives effectively disperse and stabilize the metal clusters in catalysts [7, 288], tune the catalytic reactivity [5, 286, 289] and enhance the selectivity [5, 219, 289, 290]. To understand the roles of Ge, metal-Ge alloy surfaces were employed as the model catalysts, on which the adsorption of CO as the reactant or probing molecule was investigated. Compared to pure metal surfaces, reactivity and selectivity of the metal-Ge alloy surfaces towards CO were found to be different, due to the electronically tuning effect and diluting effect of Ge additives [291]. However, the adsorption of CO on pure Ge surfaces has not been well studied [206, 209, 210].

Ge surfaces were also shown to be the good templates for growing one-dimensional metal atomic chains [292], which could be used as the connections between nano or

molecular devices. By depositing submonolayer of Pt atoms on the clean Ge(100) surface and subsequently annealing at high temperature, atomic chains with hundreds of nanometres in length and one atom in cross section were observed using scanning tunneling microscopy (STM) [293]. To explore the geometric and electronic properties of these atomic chains, adsorption of CO on them was investigated by STM. Multiple adsorption sites, a large diffusion barrier as well as remarkable long-range repulsive interaction of CO were reported [294, 295]. However, since STM cannot directly provide information on chemical nature of these chains, their exact composition is yet to be resolved. Both Pt–Pt dimers and Ge–Ge dimers were proposed to form the atomic chains [296]. The knowledge about the interaction of CO with Ge–Ge dimers, which exist on the Ge(100) surface, may be helpful to deduce the chemical nature of these chains, complementing the STM results of CO adsorption behaviors. Thus, the study of adsorption sites, adsorbate interaction as well as diffusion barriers of CO on the Ge(100) surface is highly desirable to interpret the STM results of one-dimensional Pt chains on the Ge(100) surface.

CO adsorption on the Ge(100) surface, although highly important in catalysis and future electronics, is still yet to be understood compared to CO on Si surfaces. The CO adsorption on Si(111) and Si(100) surfaces were intensively investigated by STM [297], temperature programmed desorption (TPD) [298], electron energy loss spectroscopy (EELS) [299], ultraviolet photoelectron spectroscopy (UPS) [298], X-ray photoelectron spectroscopy (XPS) [298] and theoretical methods [300–302]. CO was reported to be adsorbed on the Si(100) surface with two configurations, namely symmetric and asymmetric modes [299]. Theoretical calculations were performed to explore adsorption and desorption pathways of these two states as well as the conversion between them. The results showed that adsorption of the asymmetric mode is barrierless, whereas the binding of symmetric one needs thermal activation [299]. Compared to these results on Si(100),

the adsorption of CO on the Ge(100) surface is rather scarce except for some earlier reports concerning the change of surface conductivity [206], IR vibration frequencies [210] and desorption energy [303]. Recently, one-dimensional CO molecular chains on Ge(100) surface were observed by STM [211]. To further understand the interaction between Ge and CO, we used density functional theory (DFT) to systematically study the adsorption, adsorbate interaction and diffusion of CO on the Ge(100) surface. A unique geometric and electronic structure of CO adsorbed on Ge(100) was found in our study.

4.2 Computational details

Our calculation was based on the density functional theory implemented in software package SIESTA [278]. The generalized gradient approximation (GGA) with Perdew-Burke-Ernzerhof (PBE) [272] parameterizations was used to estimate the exchange–correlation effect. We constructed the norm-conserving pseudopotential following Troullier and Martin's optimized scheme [304]. The cut-offs of Ge 4s and 4p orbitals are 2.06 Å and 2.85 Å respectively. Other pseudopotentials can be found at the SIESTA web site [305] and were used after testing. We used double zeta split valence basis sets with polarized orbitals, which were proven to offer reliable results in the simulation of semiconductor surfaces [278]. The STM image was simulated by applying the Tersoff-Hamann approximation [228]. The counterpoise method was employed to correct the basis set superposition error (BSSE) in the calculation of adsorption energy.

The Ge(100) surface was simulated by a periodic slab model with eight layers of Ge. The bottom layer was saturated by hydrogen atoms. There were eight Ge atoms in a bulk layer and four dimers on the surface in one unit cell (Figure 4.1). Two bottom Ge layers as well as the hydrogen layer were frozen whereas the other six Ge layers were

allowed to relax during geometric optimization using conjugated gradient method. To release the hydrostatic pressure, the lattice constant of Ge was set at 5.712 Å according to results of relaxed bulk crystal. This value is in good agreement with the experimental value of 5.658 Å with a relative error less than 1%. A k-grid cut-off length of 27 Å equivalent to a $2 \times 4 \times 1$ Monk horst-Pack [275] k-point grid was used for Brillouin Zone sampling with an estimated error less than 0.1 eV/supercell.

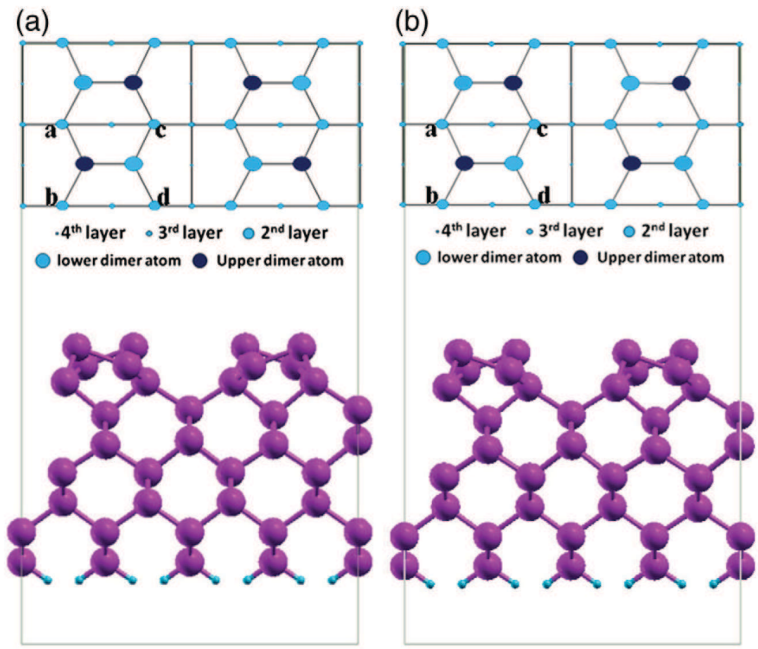

Figure 4.1: Structural models of Ge(100) surfaces. (a): Ge(100)-c(4×2); (b): Ge(100)-p(2×2). Purple balls: Ge atoms; Cyan balls: H atoms. Top inset: schematic top view of the structure. Detailed structural data are summarized in Table 4.1.

In many reported slab models, the bottom layer of substrate atoms was saturated by hydrogen. Since the electronegativity of H is larger than that of Ge (2.01), electrons transfer from bottom Ge atoms to hydrogen atoms in our model. To test how many layers this artificial effect spreads to, Mulliken charge distribution of a slab model with the bottom layer saturated by H (noted as H-slab) was analyzed and compared to another

slab model without H (noted as noH-slab).

To completely search the binding sites and configurations, we considered 20 adsorption structures for CO in various orientations in Figure 4.2. On the Ge(100)-c(4 × 2) surface, eight inequivalent positions were considered as initial adsorption sites. They include dimer atoms (1, 2), trough between dimers (3, 4) or between dimer rows (5, 6, 7), as well as the bridge of dimers (8). CO stands on each position with two possible orientations: C-attached vertically on surface (CT1–CT8) or O-attached (OT1–OT8). In addition, CO may be also bound parallel to upper–lower dimer atoms (intra-dimer: 1–2, or inter-dimer: 1–2') with C on an upper dimer Ge (C1O2, C1O2') or on a lower one (O1C2, O1C2'). The binding energy of each state is defined by the energy difference between the system after geometric optimization and the sum of free substrate and free CO molecule without BSSE correction.

The bonding analysis is based on crystal orbital Hamilton population (COHP) theory [306] implemented in SIESTA. The energy contribution of electrons filling in the crystal electronic orbitals was partitioned into the contributions from overlapping between atomic/fragment (molecular) orbital pairs. The information of overlapping between C, O and Ge atomic orbitals, as well as the overlapping between CO molecular orbitals and Ge atomic orbitals was abstracted and analyzed.

In the search of adsorption and diffusion barriers of CO on the Ge(100) surface, a constrained minimization method was used. In the adsorption process, the C–Ge distance was frozen at a series of values during optimization, while other atoms were allowed to relax to an energetic minimum. To study the diffusion barrier, the horizontal position of C was frozen at a series of values on the pathways linking two adsorption sites during geometric optimization, leaving other structural parameters to relax.

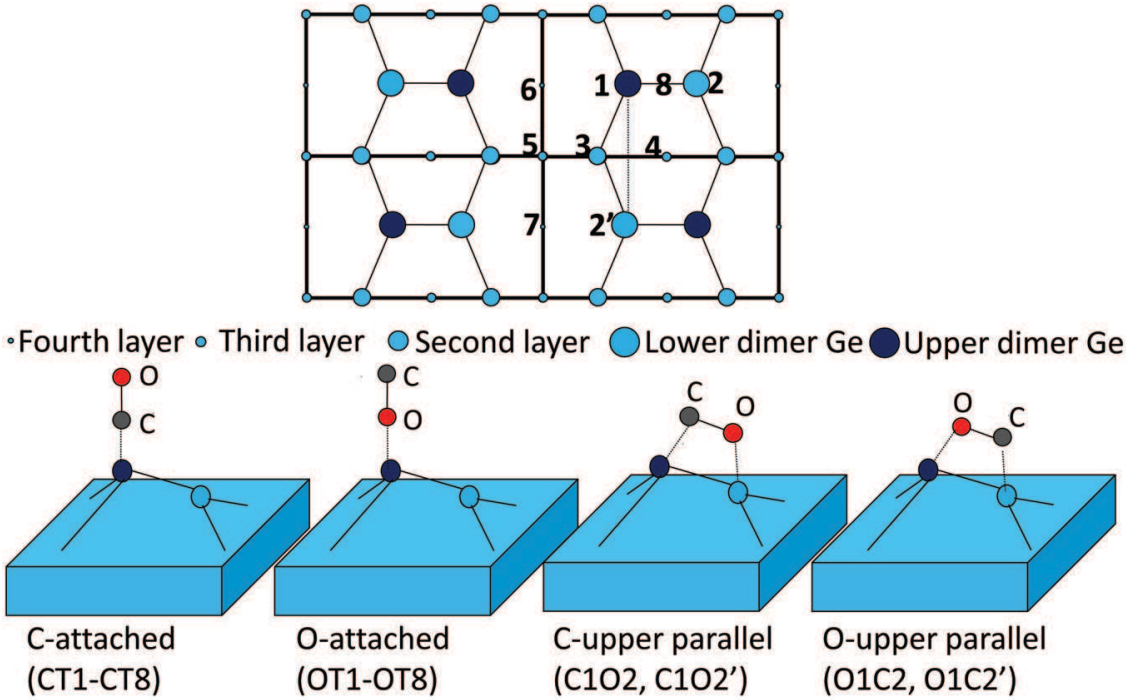

Figure 4.2: Eight possible adsorbing positions and four binding orientations of CO on the Ge(100)-c(4 × 2) surface. For Positions 1–8, CO is proposed to be adsorbed to Ge with C-attached (CT1–CT8) or O-attached (OT1–OT8) configurations. In addition, CO can also be adsorbed on the surface parallel to upper–lower dimer atom pairs (position 1 and 2, or position 1 and 2') with C (C1O2, C1O2') or O (O1C2, O1C2') binding to upper dimer Ge.

4.3 Results and discussion

4.3.1 Substrate geometries

On Ge(100), c(4×2), p(2×2) and 2×1 domains coexist in a wide temperature range. The former two are composed of asymmetric dimers, whereas the 2 × 1 reconstruction is also composed of asymmetric dimers with fast switching buckled directions [307]. Thus we simulated CO adsorption on c(4 × 2) and p(2 × 2). Figure 4.1 shows two stable

Ge(100) reconstructions c(4 × 2) and p(2 × 2) with tilted dimers. The tilt angle (19.9°) of the dimers is larger than the experimental value [308] but in good agreement with previous theoretical results [191]. Other structural parameters summarized in Table 1 are also consistent with reported experimental or theoretical data [191, 308]. The calculation shows that the energy difference between c(4 × 2) and p(2 × 2) is less than 0.04 eV/dimer, c(4 × 2) is the more stable reconstruction.

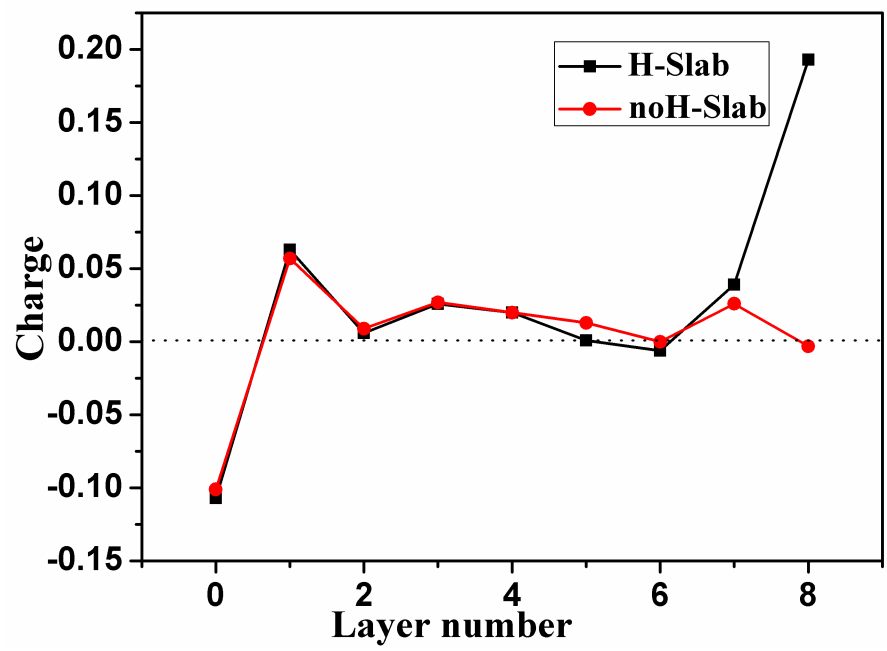

Figure 4.3: Charge distributions on each layer of two slab models. The layer number counts from surface to bulk. Layer 0: the upper dimer Ge atoms, Layer 1: lower dimer Ge atoms.

In order to test how far the influence of the bottom hydrogen layer on charge distribution spreads to, the Mulliken charge distributions of the slab models with and without bottom hydrogen layer are shown in Figure 4.3. The layers 0 and 1 are referred to the upper and lower Ge dimer atoms, which carry -0.107 and +0.065 charges respectively in two models. The charge distribution of next three layers (Layers 2–4) in two slab models are the same, indicating these layers are screened from the artificial charge effect induced

by the bottom hydrogen layer.

Table 4.1: Structural parameters of calculated c(4×2) and p(2×2) reconstructions of Ge(100).

Ge(100)	c(4 × 2)	p(2 × 2)	Other group results[a]	Experimental value[b]
Energy/eV	-0.1636	0	-	-
Tilt angle / (°)	19.9	19.9	19.5	15.6±0.5
$d_{Ge(upper)-Ge(lower)}$/ (Å)	2.58	2.59	2.55	2.55
$d_{Ge(upper)-Ge(a,b)}$[c] / (Å)	2.58, 2.58	2.57, 2.57	2.57	2.57
$d_{Ge(lower)-Ge(c,d)}$/ (Å)	2.50, 2.49	2.50, 2.49	2.46	2.46

[a] from ref [308].
[b] from ref [307].
[c] Ge atoms a, b, c, d were labeled in the inset of Figure 4.1.

The most distinct discrepancy between the two charge distribution curves emerges at the bottom Ge layer (Layer 8), where the Ge atoms carry +0.193 charges in H-slab model, but -0.03 in the noH-slab. This difference gradually diminishes when the layer number decreases, eventually disappearing at Layer 4. If the number of substrate layer is less than five, this artificial charge effect would spread to the surface layer, and distort the surface geometries and electronic properties. Thus, to obtain reliable and more accurate results from slab models, the number of substrate layers is suggested to be > 5. This is especially necessary when the bottom layer is saturated by the heteroatoms whose electronegativity differs much from the substrate atoms. In this paper, since an eight layer model is proved to be sufficient to screen the artificially induced charge effect, we used the conventional hydrogen saturated slab model for the convenience of comparison with previous studies.

4.3.2 Adsorbate configurations

Since c(4 × 2) is the more stable reconstruction of the Ge(100) surface, we simulated CO adsorption on this slab model as shown in Figure 4.1a. After geometric optimization, the energies of 20 possible adsorption states are listed in Table 2. The calculation results indicate that CO is unable to binds to Ge in O attached (OT1–OT8) configuration, in accordance with the case of CO on metal and silicon surfaces. This is supported by the failure in forming any substantial bonding between CO and Ge surface in these systems after geometric optimization. In C-attached configurations, many (CT1, CT3-8) are not energetically stable. Four parallel configurations were also found to be unfavorable, excluding the possibility of forming bridge configurations of CO on the Ge(100) surface. Among these 20 initial configurations, CT2, CT3, CT8, C1O2, C1O2' and O1C2' relax into the same stable configuration, which is of the lowest binding energy (-1.24 eV).

Table 4.2: Energies of 20 guessed adsorbing structures after geometric optimization.

C-attached	CT1	CT2	CT3	CT4	CT5	CT6	CT7	CT8
Energy[a] /eV	-0.31	-1.25	-1.22	-0.64	-0.68	-0.63	-0.65	-1.25
O-attached	OT1	OT2	OT3	OT4	OT5	OT6	OT7	OT8
Energy/eV	-0.2	-0.41	-0.44	-0.5	-0.67	-0.5	-0.55	-0.43
Parallel	C1O2	C1O2'	O1C2	O1C2'				
Energy/eV	-1.24	-1.24	-0.61	-1.24				

[a] The energies have not been BSSE corrected.

Figure 4.4 shows the structure of this stable configuration. CO is bound to the Ge(100)-c(4 × 2) surface with C attached on a lower dimer Ge atom. The C, O and the

Table 4.3: Calculated structural parameters of CO adsorbed on Ge(100)-c(4 × 2).

System	Adsorptional structure	Calculated free system
Tilt angle / (°)	16.4	19.9
$d_{Ge(up)-Ge(lower)}$/ (Å)	2.64	2.58
d_{C-O}(Å)	1.2	1.15
ν C-O(cm^{-1})	2012	2126
Charge(C)	0.015	-0.3
Charge(O)	0.335	0.3
Charge(Ge)[a]	-0.222	0.063

[a] Ge is referred to the binding Ge atom.

binding Ge dimer are in the same plane perpendicular to the Ge surface. CO is almost perpendicular to Ge dimer (92°) and the C–Ge bond length is 1.99 A. The simulated filled state STM image in top inset of Figure 4.4 shows an extra bright spot emerging at the vacancy of the pristine zigzag chain of the clean Ge(100)-c(4 × 2) surface. As listed in Table 3, the C–O bond length (1.20 Å) is slightly larger than that of the free CO molecule (1.15 Å), indicating that the CO bond is partially weakened due to the adsorption. This increase in CO bond length is similar to that of CO adsorbed on Si(100) [301]. Meanwhile, the Ge dimer bond length (2.64 Å) becomes longer than that on a clean surface (2.58 Å). The tilt angle is also reduced from 19.9° in a clean substrate model to 16.4° in adsorption state. The Mulliken charge distribution analysis shows that C transits from electronically negative to positive state and O becomes more positive. The positive lower dimer Ge turns negative after adsorption, indicating that electrons transfer from CO to the Ge surface. These changes in geometric and electronic properties

after the adsorption can be explained in C 2s or CO 3σ, 4σ-donation mechanism, which we will discuss in detail later.

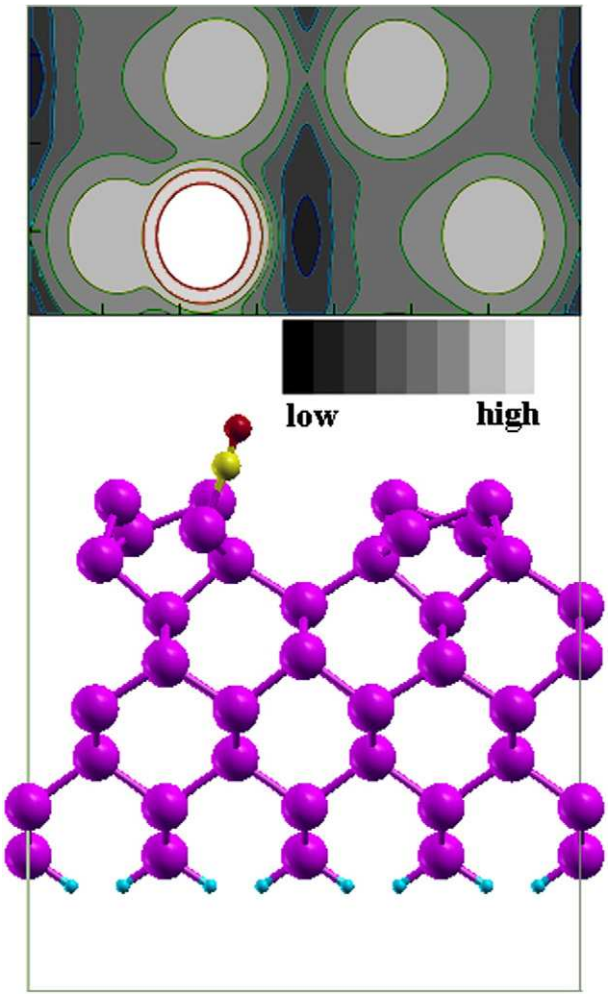

Figure 4.4: The stable structure of CO adsorbed on Ge(100)-c(4×2). The rectangle border refers to the boundary of the super cell. Top: the simulated filled state STM image. Purple balls: Ge atoms; Cyan balls: H atoms. Yellow: C. Red: O.

We noticed that single hydrogen atom also prefers to adsorb on the lower dimer atom of Ge(100), thus it is interesting to compare these two adsorptional structures. Both the tilt angles reduce upon adsorption, but for Ge(100):H, the tilt angle reduce significantly from 19° to about 5.8° [168]. In addition, in filled state STM images, CO

would appear as the brighter protrusion than the upper dimer atom, whereas H appear as a dimmer spot than the upper dimer atom in Ge(100): H [170]. This is because CO has larger geometric height with standing up configuration as well as larger density of states due to the existence of degenerated π electrons near Fermi level compared to H. The discrepancy in STM images will be helpful to discriminate CO on Ge(100) and H on Ge(100) experimentally. The calculated adsorption energy after BSSE correction

Table 4.4: Adsorption and repulsive energy of CO molecules on Ge(100) surface at a coverage of 0.5.

Adsorbing sites[a]	*A*	*AB*	*AC*	*AD*
E_{ads}/per CO (kcal/mol)	14.5	14.3	15.1	15.2
$E_{repulsive}$ (kcal/mol)[b]	0	0.2	-0.6	-0.7

[a] A, B, C, D were labeled in the inset of Figure 4.7.
[b] $E_{repulsive}$=E_{ads}(A)-E_{ads}(AB/AC/AD).

is 14.5 kcal/mol (Table 4), indicating that CO undergoes a weak chemisorption on the Ge surface. This value is comparable to the previous experimental result (26 kcal/mol) obtained using a desorption spectrometry method [303]. The value is similar to the calculated adsorption energy of CO on Si(100) (14.5 kcal/mol) [299, 301], but lower than the value of CO on transition metal surfaces, such as 34 kcal/mol on Pt(111). Another evidence of weak chemisorption and weakening of CO bond is that the C–O stretching frequency is red-shifted from 2126 cm^{-1} in gaseous state to 2012 cm^{-1} in the adsorbed structure. These two values agree well with reported 2132 cm^{-1} and 2070 cm^{-1} respectively in an IR measurement of CO adsorbing on Ge evaporated films in vacuum under 77 K [210].

4.3.3 Bonding analysis

To gain insight into the bonding mechanism of CO with the Ge surface, crystal orbital Hamilton population (COHP) [306] analysis was applied to the adsorption structure. Previous COHP studies showed that the substrate-CO bonding can be interpreted in a local binding site-CO bonding model [309]. Thus our discussion is mainly focused on the Ge–CO orbital interactions (Ge refers to the binding Ge atom hereafter). The energy resolved contributions of Ge–C Hamilton (overlapping between all valence orbitals of Ge and C) and Ge–O Hamilton were investigated and listed at the bottom of Figure 4.5a. The Ge–C curve shows that Ge and C have substantial bonding interactions (negative energy contribution) around -15 eV and -12 eV. In contrast, the Ge–O curve overlaps with zero base line below the Fermi level, indicating that Ge–O interaction is relatively negligible. This is attributable to the greater distance of Ge–O compared to Ge–C, preventing the effective orbital overlapping. Under the peaks of Ge–C curve around -15 eV and -12 eV, Ge–C 2s orbital interaction makes the major contribution to the Ge–C bonding, as the Ge–C 2s curve has the largest peak. In contrast to C 2s orbital, the O 2s orbital only has a small anti-bonding contribution with Ge around -15 eV, suggesting the involvement of CO σ^* molecular orbital in bonding. For atomic orbitals at higher levels, such as C $2p_z$ and O $2p_z$, they contribute less in Ge–C interaction. Both C $2p_x$ and O $2p_x$ have the least impact on Ge–C bonding, indicating that no π bond is formed between Ge and C.

To trace which orbital of Ge interacts most strongly with C 2s, the energy contribution of Ge–C 2s was further partitioned into the interactions between various Ge atomic orbitals (4s, $4p_x$, $4p_y$, $4p_z$, 4d) and C 2s. As shown at the top of Figure 4.5a, Ge 4s and $4p_z$ are two most important orbitals to the Ge–C 2s interaction. Ge $4p_z$ has two striking

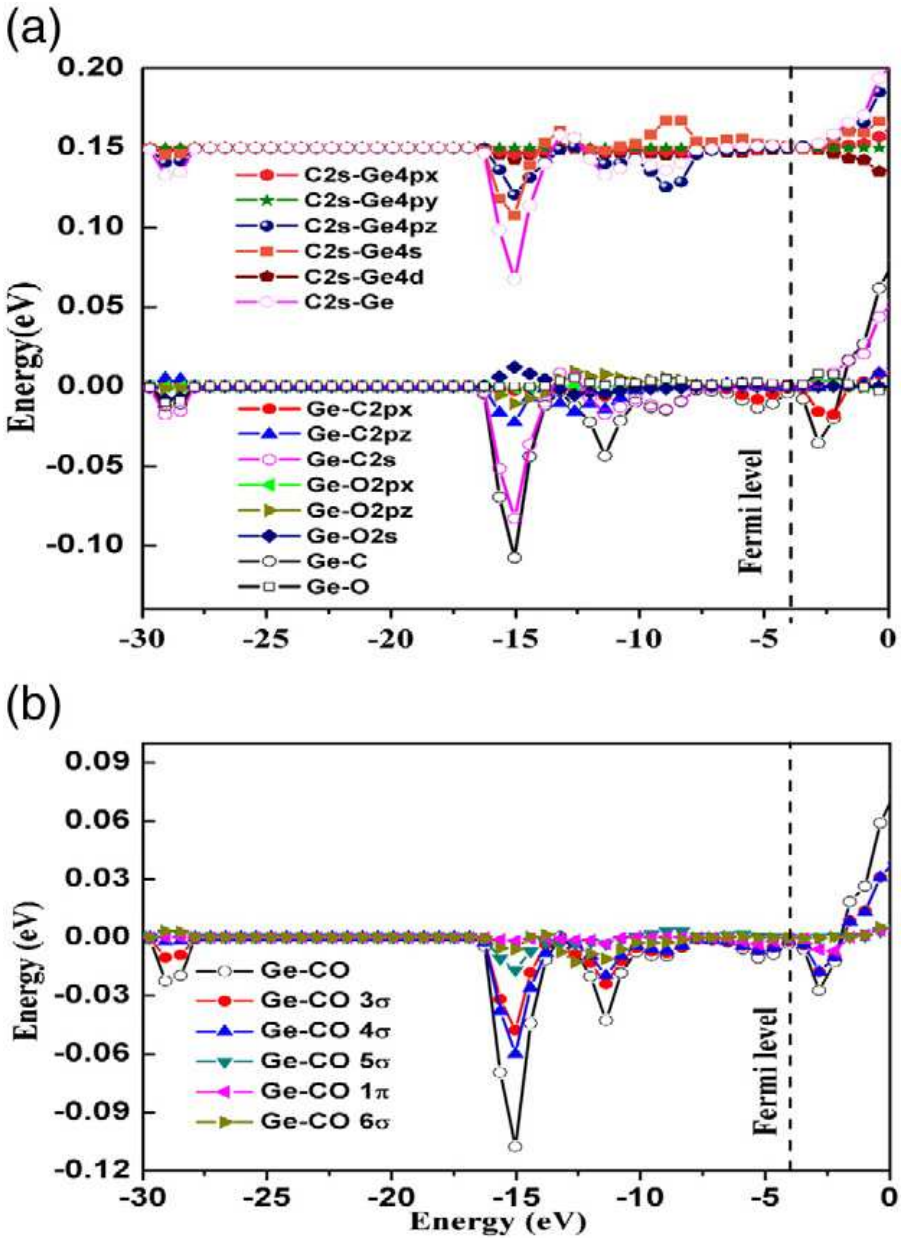

Figure 4.5: COHP curves of CO adsorbed on Ge(100)-c(4 × 2). Note "Ge" in the figure refers to the binding Ge atom. (a) Bottom: the energy-resolved contributions of C and O atomic orbitals to Ge–CO interaction; Top: the contributions of Ge atomic orbitals to Ge–C 2s interaction. (b) Contributions of CO molecular orbitals to Ge–CO interaction.

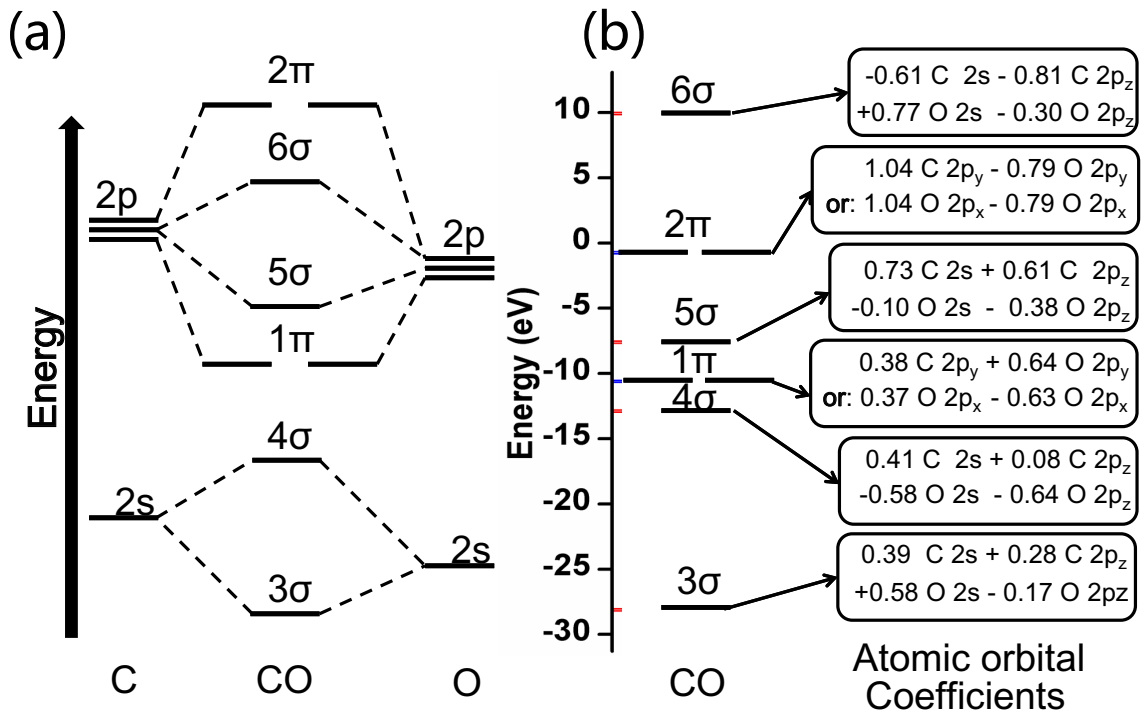

Figure 4.6: Molecular orbitals of CO. (a)Simple molecular orbital scheme of CO from a text book [310]. For each molecular orbital: $\psi = \frac{\sqrt{2}}{2}(\phi_C \pm \phi_O)$, $\phi = 2s, 2p_x, 2p_y, 2p_z$. (b) A more realistic orbital scheme of CO from our calculation.

bonding states with C 2s around -15 eV and -8 eV, making major contribution to the Ge–C 2s bonding. Ge 4s is also involved in bonding around -15 eV and anti-bonding around -8 eV. The latter cancels out the bonding contribution of the former around -15 eV. Thus Ge 4s contributes less in Ge–C 2s bonding compared to the Ge 4p$_z$. Since the Ge–C bond is nearly vertical to the Ge surface and parallel to axis of Ge 4p$_z$, the 4p$_z$ is approximately considered to be the major orbital of bonding, forming σ bond with C 2s with a head-to-head configuration. Other Ge orbitals like 4p$_x$, 4p$_y$ and 4d have less or no bonding contribution to the Ge–C 2s interaction due to the mismatches in symmetry or energy. In short, Ge–C bonding mechanism can be ascribed to the σ bond formed through overlapping between C 2s and Ge 4p$_z$.

The bonding mechanism can also be interpreted in the view of Ge atomic orbitals-CO molecular orbital interaction. In a traditional and simplified MO scheme shown in 4.6a [310], CO at electronic ground state has an orbital configuration of $(1\sigma)^2$ $(2\sigma)^2$ $(3\sigma)^2$ $(4\sigma)^2$ $(1\pi)^4$ $(5\sigma)^2$ $(2\pi)^0$ $(6\sigma)^0$. In this scheme, the 3σ and 4σ are produced from the combination of C 2s and O 2s, regardless of interatomic 2s-2p integrations. This simple diagram, among many other popular diagrams, surprisingly reflects the merit of 3σ and 4σ compared to the realistic orbital scheme from our DFT calculation (in 4.6b). Thus we use this simple scheme throughout our binding analysis. The energy contributions from the overlapping between them and Ge orbitals are shown in Figure 4.5b. 3σ and 4σ of CO have nearly equal contributions to the Ge–CO bonding. This is different from the case of CO on Si(100), where the bonding was mainly due to the sole donation of CO 4σ orbital to Ge orbital [297]. The equivalent contribution of 3σ and 4σ can be understood with COHP theory. According to the COHP theory, if a fragment orbital B is composed of two atomic orbitals B1 and B2, the energy contribution from the overlapping between any orbital A and this fragment orbital B can be linearly partitioned to the contributions from A–B1 and A–B2. 3σ and 4σ are mainly the combinations of C 2s and O 2s orbitals in the same or opposite phases, respectively. C 2s is the atomic orbital of major contribution to Ge–C bonding as shown in Figure 4.5a, whereas the bonding contribution from O 2s is almost negligible. The equality of contributions from CO 3σ and 4σ is in fact a reflection of major role of C 2s in bonding. Considering the electron transfer direction discussed above, we conclude that the interaction between CO and Ge(100) surface is mainly due to C 2s donation or CO 3σ and 4σ donation rather than the only 4σ donation. It is surprising at the first glance that C 2s donation contributes the major bonding, though C $2p_z$ is more diffuse that C 2s. However, since $3\sigma, 4\sigma and 5\sigma$ all have a major atomic component C 2s rather than C 2p as shown in 4.6. Thus the donations from these three

occupied molecular orbital resulting in the major donation of C 2s. Besides 3σ and 4σ, 5σ has a slight bonding component in the Ge–C interaction, other orbitals, such as 1π, 2π and 6σ are not involved. The emptiness of these anti-bonding orbitals 2π, 6σ well supports the fact that the bond length and stretching frequency of CO only experiences a small change after adsorption. This is in contrast to the case of CO on transition metal surfaces, where the d-π back-donation significantly elongates the CO bond and causes large red-shift of CO stretching frequency [311]. In the case of CO on Ge(100), Ge 3d orbitals are fully occupied and their energy levels are too low to donate electrons to CO 2π orbital.

4.3.4 Other possible adsorption structures

By extensive search for all possible adsorbing structures, we only found the above stable one. It was reported that CO has two adsorption configurations on Si(100), namely the asymmetric and symmetric models. The asymmetric state is similar to that of CO on Ge(100) we described above. The symmetric configuration, referred to CO standing at the bridge position of the symmetric (unbuckled) Si dimer with its C end [299–301], was not found on Ge(100). Geometry optimization of this symmetric model on Ge(100) finally led to divergence even after forcing the dimer to be unbuckled, indicating that such a symmetric structure may not exist on the Ge(100) surface.

The absence of symmetric configuration on Ge(100) is attributable to the loss of large buckling energy of the binding dimer. For CO on Si(100), the adsorption energy of the asymmetric and symmetric configurations are 14.5 kcal/mol and 8.3 kcal/mol respectively [299]. The difference of adsorption energy between these two configurations is from two parts. One part is the loss of buckling energy defined by the energy difference

between the buckled and unbuckled dimers, which was reported to be 1.4 kcal/mol for Si(100) in a theoretical study [20]. The other part is the loss of orbital interaction energy due to the change of bonding mechanism, from σ bonding in asymmetric model to π bonding in symmetric state. It is estimated to be 4.8 ($= 14.5 - 8.3 - 1.4$) kcal/mol using the above data. This part of energy loss on Ge(100) should be approximately 4.8 kcal/mol analogous to on Si(100). However, on the Ge(100) surface, the bulking energy is 6.9 kcal/mol [20]. It would finally reduce the adsorption energy of CO on Ge(100) in symmetric model to $14.5 - 4.8 - 6.9 = 2.8$ kcal/mol. This value suggests that such a model would be less energetically favorable compared to the asymmetric model.

After studying single CO on Ge(100), adsorption of multiple CO molecules were also investigated in order to survey the adsorbate interaction. Our calculations excluded the possibility of two CO molecules adsorbed on the same dimer, with each C attached to one Ge dimer atom. This is owing to the upper dimer Ge atom of negative charge, hindering the σ-donating bonding from CO. Once the first CO is adsorbed on the lower one, electrons transfer from CO to the dimer, making the upper Ge atom more electronically negative. Thus adsorption of second CO molecules is more energetically unfavorable. The second CO can only occupy the other three lower dimer Ge atoms in our slab model, marked as B, C and D in the inset of Figure 4.7. At a coverage of 0.5 monolayer, two CO molecules have three possible configurations: AB, AC and AD.

The interaction between two nearest adsorbed CO molecules was studied by comparing adsorption energies per CO molecule on Ge(100). In all three configurations (AB, AC, AD), the repulsive energies due to adsorbate interaction are less than 1 kcal/mol in Table 4. Even the interactions between other further CO pairs are neglected, the repulsive energies between nearest CO pairs are much smaller than that of CO on transition

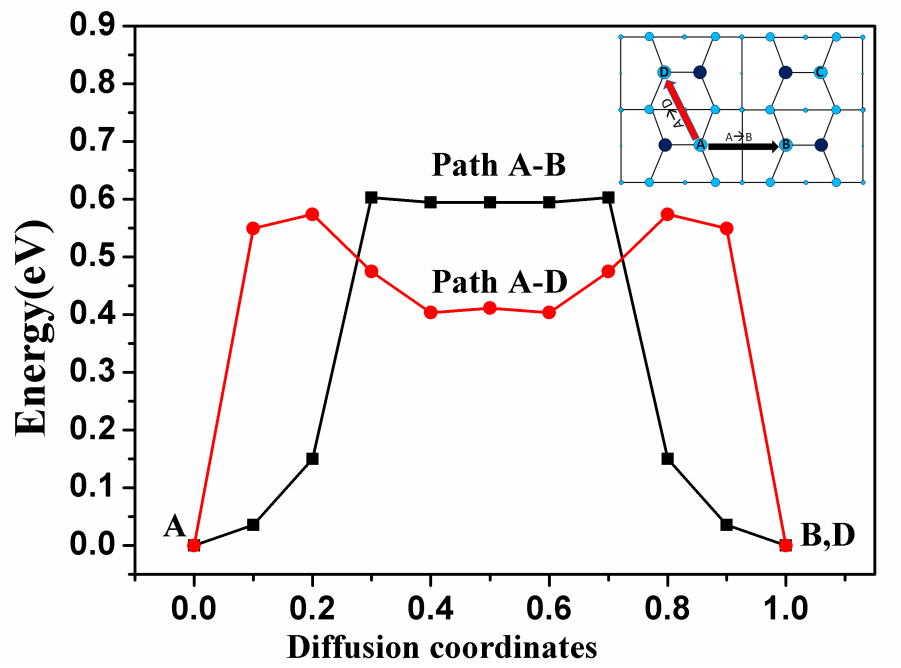

Figure 4.7: Energy barriers of CO diffusing in different pathways. The data of diffusion coordinates larger than 0.5 were duplicated according to the symmetry of the pathways

metal surfaces, where a typical value of 35 kcal/mol was reported for CO on Pt(111). The repulsive energy originates from two parts: the dipole interaction between two adsorbed CO and the change of surface electron density at the binding sites [312]. On Ge(100), the dimer are sparsely distributed, the minimum distance between two neighboring lower dimer atoms is 6 Å, larger than the distance between two neighboring Pt atoms (2.7 A) on Pt(111). Since the dipole interaction decays fast in an inverse proportion to the cube of the distance, it becomes much lower for CO molecules on Ge(100) compared to that of on Pt(111). In addition, the adsorption of the first CO perturbs the surface electron density at the binding site via a σ donation and/or π back-donation mechanism. On metal surfaces, with the help of delocalized conductive electrons, the perturbation of electronic density is able to spread to as far as the neighboring binding site, where the adsorption energy of a second CO is depleted. In contrast, On Ge(100), the covalent

bonds from saturated sub-layer connect two binding sites. The localized electrons in these covalent bonds screen the perturbation of electron density effectively. The electron density at the neighboring binding site is not significantly affected. Thus, the adsorption energy is almost retained.

4.3.5 Adsorption and diffusion pathways

To study the adsorption pathway of CO, we scanned the adsorbing process by varying the Ge–C distance from 1.49 Å to 3.49 Å in a step size of 0.1 Å (Figure 4.8). When CO is approaching Ge, the system energy gradually decreases, and reaching a minimum at the stable structure we describe above. After that, it sharply rises when the Ge–C distance is further reduces. There is no well defined transition state during adsorption, similar to CO adsorption on Si(100) [299], indicating this process is barrierless. For this asymmetric structure, the Ge dimer keeps buckled during adsorption, thus the adsorption energy is mainly proportional to the overlapping between C 2s and Ge $4p_z$. When the Ge–C distance depresses, these two orbitals overlaps more effectively, the system energy reduces continuously without any barrier.

The diffusion of CO from one lower dimer Ge to other neighboring binding sites was also investigated. The potential energy profiles of CO diffusing along A→B, or A→D were shown in Figure 4.7. Both routes have energy barriers around 14 kcal/mol. This value is almost the same as the adsorption energy. The coincidence could be understood from Ge–CO orbital interaction as we analyzed above. The adsorption energy is mainly attributable to the σ bond formation by Ge $4p_z$–C 2s, which is perpendicular to the surface. When CO diffuses horizontally from one site to another, the orbital overlapping drops sharply. The value of 14 kcal/mol indicates that CO almost loses all orbital

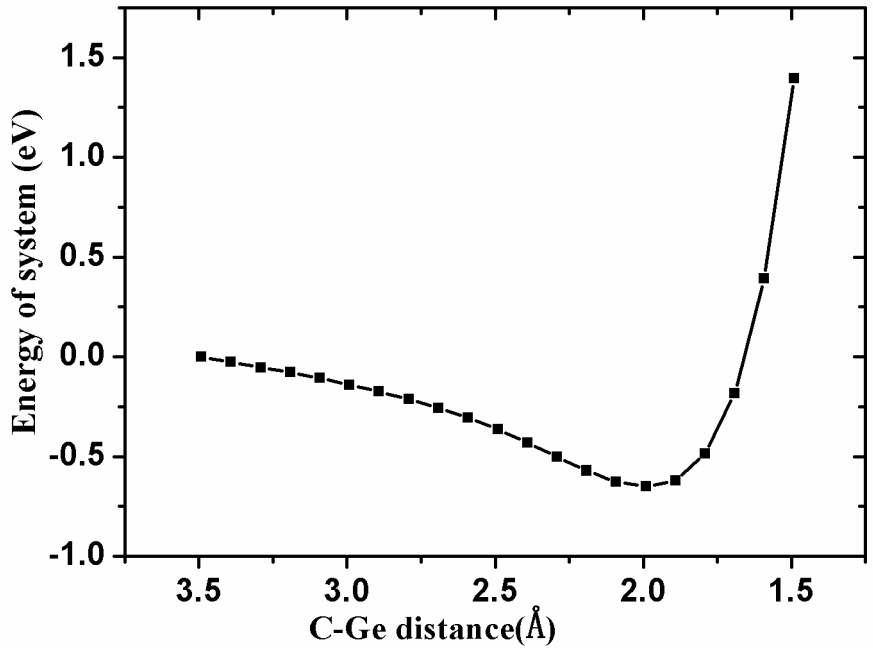

Figure 4.8: the energy profile of CO adsorption versus C–Ge distance.

bonding with Ge during the diffusion, undergoing desorption–adsorption transitions. We also noted that this value is lower than 20 kcal/mol, reported for CO diffusion on Pt-induce chains on Ge(100) surface [294], suggesting that those chains are not likely composed of Ge dimers as suggested by earlier theoretical studies [311].

4.4 Conclusion

Our study shows that CO is exclusively bound to the Ge(100) dimer in a standing configuration with C end attached to the lower dimer Ge atom. The adsorption is weak and the CO bond is partially elongated after adsorption. The orbital analysis indicates that the Ge–CO interaction is attributable to the Ge $4p_z$–C 2s σ bonding, or 3σ, 4σ of CO donation to Ge. The repulsive energy between neighboring adsorbed CO molecules is less than 1 kcal/mol. The energy profile of adsorption pathway demonstrates that the

adsorption is barrierless. The diffusion barrier of CO on Ge(100) surface is 14 kcal/mol. These results may be helpful to the study of Ge in catalysis as well as understanding the STM results of one-dimensional metal atomic chains on the Ge(100) surface.

Chapter 5

Atomic processes of NO oxynitridation on Ge(100): a theoretical investigation

5.1 Introduction

As the development of Si based complementary metal oxide semiconductors (CMOS) has been increasingly difficult through the conventional scaling technique, germanium has received renewed attentions due to its intrinsically high carrier mobility than that of Si [313, 314]. However, the native oxide of Ge, GeO_2 is of high water solubility, high density of defects and low thermal stability, and is not suitable to serve as the gate material. Finding an good gate material becomes a key step in fabrication of Ge-based circuits. Germanium oxynitride (GeO_xN_y) is a promising candidate [315] because it is able to improve the stability of Ge substrate against thermal and wet treatment [316,317], to suppress the diffusion of Ge into the high-κ metal-oxide layer and to reduce the leakage current. The simplest method to synthesize germanium oxynitride is to adsorb nitric oxide (NO) on Ge substrates, followed by the thermal treatment [189–196]. This method does not induce unwanted foreign elements, thus the synthesized germanium oxynitride is of high purity. However, compared to other oxynitridation gas such as NH_3, the nitridation efficiency, evaluated by N incorporation rate is still low. To enhance

the efficiency, it is necessary to understand the atomic processes of NO adsorption and dissociation on Ge(100).

Adsorption and desorption of nitric oxide on the Ge(100) surface was investigated using temperature-programmed desorption (TPD) [318]. The desorption of NO molecules increases after an onset dosage, producing a peak around 220 K. Beside this large molecular desorption peak, a small peak of N_2 was also found at 190 K, indicating minority of NO molecules undergoes dissociation. In the view of increasing the N incorporating ratio, the release of N_2 during adsorption process should be suppressed as much as possible. Electron-stimulated desorption (ESD) of NO and N_2O adsorbed on Ge(100) suggests the formation of NO dimers on Ge(100) during adsorption [199, 200]. Electron energy loss spectroscopy (EELS) surprisingly did not detect any NO stretching mode, suggesting that NO may dimerize to a dipole inactive configuration [318]. However, the existence of NO dimers is yet to be supported by more evidences, as this mechanism completely excludes the monomeric adsorption and dissociation. TPD results also showed that the reactivity of NO on Ge(100) is lower than that on Si(100), where NO molecules start to dissociate at as low as 20 K [319], and completely dissociate above 150 K [320]. Given the similarity between Ge(100) and Si(100), the discrepancy in reactivities of NO on them is interesting. Since the reaction mechanism of NO adsorption on Ge(100) is far yet to be understood, it is hard to explain the EELS puzzle and low reactivity of NO on Ge(100). A theoretical calculation is useful because it would reveal the reaction precursors and dissociation mechanisms. In this study, we investigated atomic processes in the initial stages of NO adsorption and dissociation on the Ge(100) surface using DFT calculations. Various non-dissociative and dissociative intermediate/products of NO were found, and the reaction pathways were also predicted by searching the transition states. We also surveyed dimeric adsorption on Ge(100). The exothermicity of ONNO chains binding on

various sites with different attaching atoms (OO, NN or NO) are surveyed and compared with monomeric adsorption.

5.2 Computational details

All calculations were performed using DFT software CASTEP in Materials Studio (version 5.5) of Accelrys [277]. The generalized gradient approximation (GGA) with Perdew-Burke-Ernzerhof (PBE) parameterizations [272] was used to estimate the exchange-correlation effect. The kinetic energy cut-off was 330 eV. A 2×4×1 Monkhorst-Pack grid was used for Brillouin Zone sampling [275]. The force convergence criteria of geometric optimization was 0.02 eV/Å. A thermal smearing of 0.025 eV was used to accelerate the SCF convergence.

The Ge(100) surface was simulated by a periodic slab model with six layers of Ge. Each layer consists of eight Ge atoms or four Ge dimers. Two bottom Ge layers were frozen during geometry optimization. The lattice constant of Ge was set at 5.712 Å according to the relaxation of bulk crystal. The Broyden-Fletcher-Goldfarb-Shanno (BFGS) method was used in geometry optimization, and a linear synchronous transit/quadratic synchronous transit (QST) method was used to find transition states.

To completely search non-dissociative adsorption products of NO on Ge(100), we considered 30 initial adsorption structures with NO in various orientations and sites in Figure 5.1. They include dimer atoms (1, 2), trough between dimers (3, 4) or between dimer rows (5, 6, 7), the bridge of dimers (8) or their back bonds(9,10). NO stands on each above position with two possible orientations: N-attached vertically on surface (NT1–NT10) or O-attached (OT1–OT10). NO may also be bound parallel to dimer

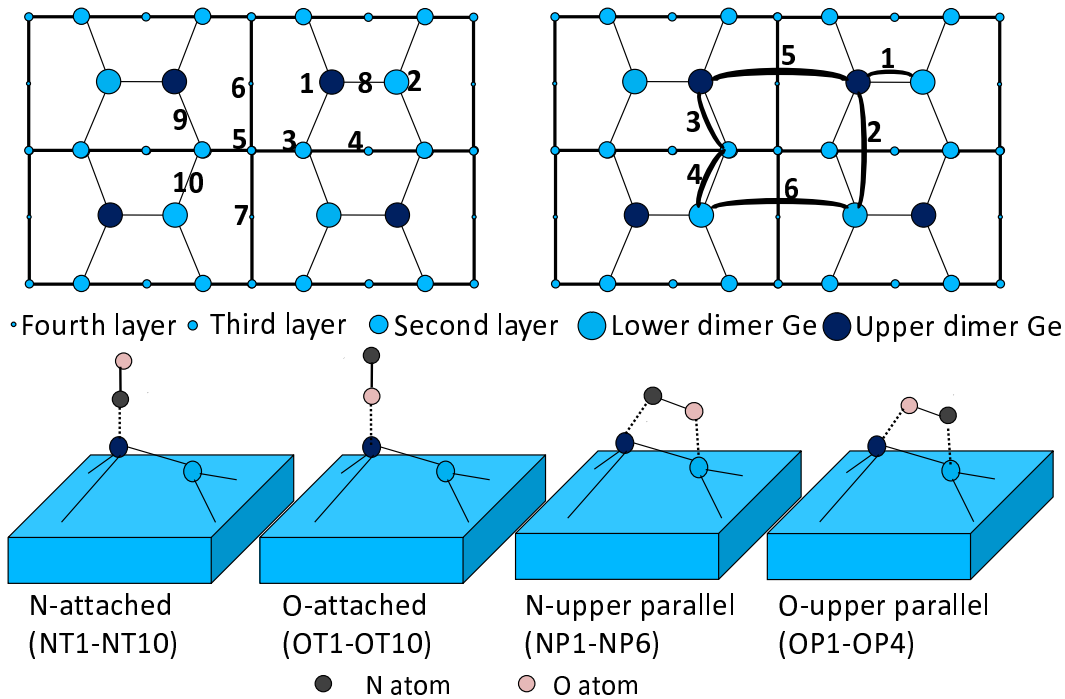

Figure 5.1: Possible adsorbing sites and orientations of NO on the Ge(100) surface. Top left: NO is vertically adsorbed to Ge with N-attached (NT1–CT10) or O-attached (OT1–OT10) configurations. Top right: NO is adsorbed parallel to the atom pairs with N (NP1–NP6) or O (OP1–OP4) at an upper position.

atom pairs, or back bonds with N (NP1–6) or O (OP1–4) at an upper position. After dissociation, N–O bond cleaves and the N and O atoms may bind one, two or three Ge atoms (only for N) respectively. 18 dissociative structures (not shown here) are investigated, the stable structures after geometric optimization are discussed. Two NO molecules may dimerize first in gas phase or physisorbed state, forming the trans- or cis- ONNO chain in Figure 5.2. The ONNO chain bridges a pair of Ge atoms (1 to 6) in Figure 5.2. The cis-ONNO chain can bind to the Ge surface with its two O atoms (OO1-OO6) or two N atoms (NN1-NN6), and the trans-chain is also able to bind on the surface with a N and an O atom (NO1-NO6).

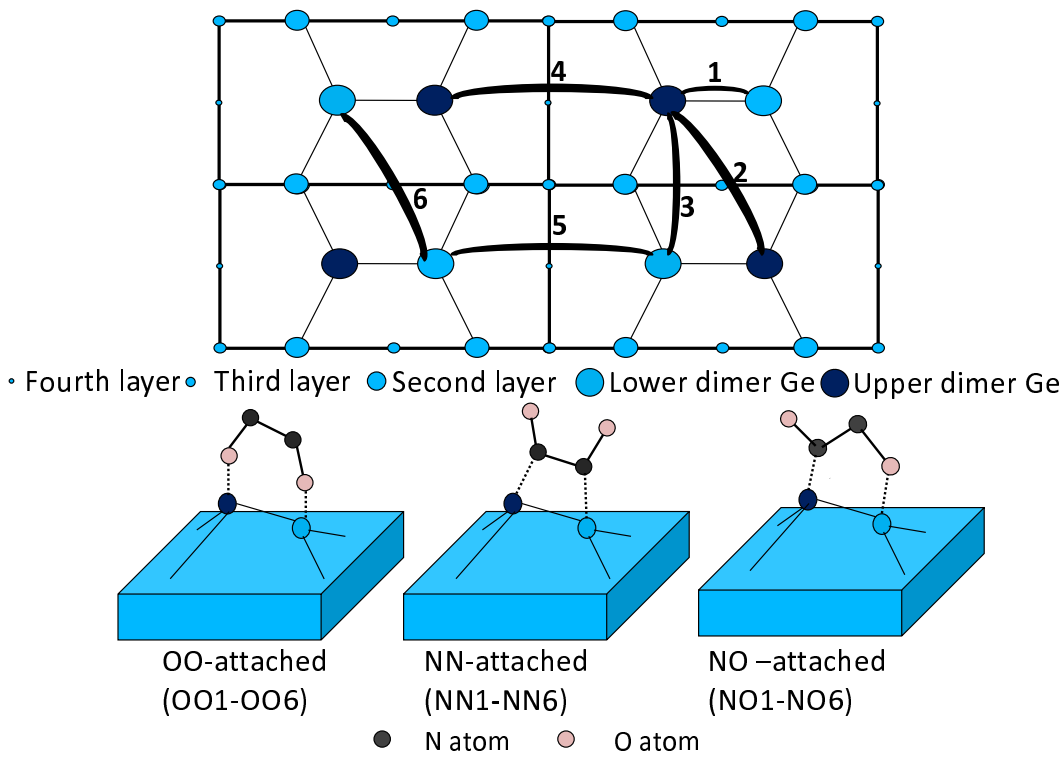

Figure 5.2: Possible configurations of NO dimers reacting on Ge(100). Top: six bridge positions of dimer atoms for NO dimer binding. Bottom: three types of binding configuration: OO, NN and NO attachments.

5.3 Results and discussion

5.3.1 Monomeric adsorption

5.3.1.1 Non-dissociative adsorption

First we performed extensive search of non-dissociative adsorption products of NO on the Ge(100)-c(4×2) surface. After geometric optimizations, six stable non-dissociative structures were found and shown in Figure 5.3. Their energies and structural parameters were listed in Table 5.1. In these six structures, the N–O bond lengths increase from

1.10 Å in free state to 1.33 ∼ 1.44 Å, indicating significant weakening of N–O. The adsorption energies vary from -0.08 to 1.01 eV, are relatively lower than that of NO on Si(100) in molecular adsorption states (1.67 ∼ 1.97 eV) by ∼1 eV. NO can insert into a dimer bond or a back bond with its N end, forming N12–O3 or N17–O. Although the corresponding N–O and N–Ge lengths are nearly the same in the two structures, they differ significantly in the binding energies. N12–O3 is more stable than the free system by 0.64 eV, whereas N17–O is slightly less stable than the free system by 0.08 eV. The higher binding energy of N12–O3 than that of N17–O is mainly attributable to formation of an extra O–Ge bond, which connects the O atom with neighboring dimer. The formation of the O–Ge bond further weakens the N–O bond from 1.33 Å in N17–O to 1.44 Å in N12–O3. However, the analogous structure of N12–O3 on Si(100) only appears as a transition state in the process of interdimer dissociation [321]. In addition, the configuration of NO vertically inserting into a dimer with the N end, reported on Si(100), was not found on Ge(100) surface. In Figures 5.3c and d, NO bridges a Ge dimer and a pair of ends of two neighboring dimers in a parallel configuration, respectively. The intradimer product N1–O2 has the highest binding energy among the six non-dissociative products (1.01 eV), larger than that of the interdimer binding N1–O3 (0.67 eV). Since the corresponding N–O, N–Ge and O–Ge bond lengths are nearly the same in these two models, the difference in energies rises from the binding sites. In N1–O2, NO adds to one dimer and eliminating two dangling bonds, leaving the other dimer intact. In contrast, in N1–O3, NO binds to two dimers, releasing two unreacted Ge dimer atoms, which are of higher energies than the pristine dimer atoms.

Figure 5.3e shows another intradimer product, in which NO is tilted and twisted on the dimer, no longer parallel to the dimer. Although in this structure, the coordination number of N becomes three and the N–Ge, O–Ge bond lengths are shorter than that of

N1–O2, the energy is the same as N1–O3. This structure is an important intermediate in the dissociative processes, which we will demonstrate later. Finally, Figure 5.3f is the only O-attached nondissociative adsorption configuration. The O-end of NO is unable to insert into any dimer bond or back bond due to the limited valence number of O. Although the adsorption energy is close to zero, N17–O cannot be simply considered as the physisorption state as the N–O bond is significantly elongated. The N-end may be activated and can accept another NO molecules.

We also searched the formation barriers for these non-dissociative products. N12–O3, N1–O3, N1–O2 directly form from the non-interactive system without any barriers. The system energies decrease gradually when the NO molecule approaches the Ge(100) surface. The other two, N17–O and N-O4 are also of lower barrier 0.10 eV and 0.12 eV, respectively. Because of the negative binding energies, they are easy to desorb from Ge(100) even at lower temperature. These two are trivial adsorption products compared to the other four in consideration of dissociative processes.

5.3.1.2 Dissociative products

After we searched the dissociative products, the meaningful structures can be divided into three groups: N-2fold, N-3fold, N-4fold, according to the coordination number of N. Figure 5.4 shows the characteristic structures of N-2fold dissociative products. When the N atom inserts into a dimer, the O atom can insert into the back bond (N12O48, N12O28) and dimer bond (N12O34). Once the N atom inserts into a back bond, the O atom can insert into the dimer (N17O12, N17O34). Among these five models, the most stable one is N12O28, in which N and O insert into a dimer and the adjacent back bond. Compared to N12O48, in which N and O insert into a dimer and an isolated back bond respectively, N12O28 is more stable by 0.15 eV. This promotive effect of inserted N in

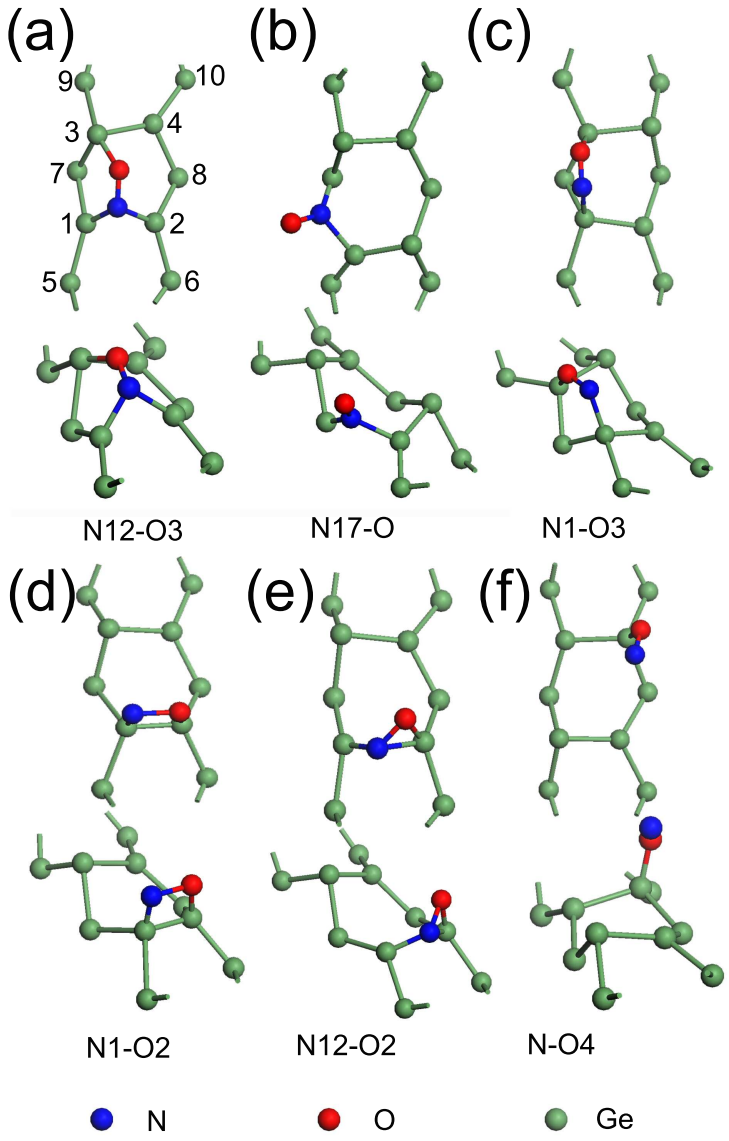

Figure 5.3: Top and side views of stable structures of non-dissociative NO adsorption products on the Ge(100)-c(4×2) surface. The products are named by: "N"+"the labels of N binding Ge atom"+"–"+"O"+"the labels of O binding Ge atoms". The top and bottom of each sub-figure refer to the top and side view of the product respectively. (a) N12–O3: N inserts into a dimer. The numbers 1–4 label four dimer atoms, and 5–10 label six sub-layer atoms. (b) N17–O: N inserts into a back bond. (d) N1–O3: NO connects each end of two dimers in a dimer row. (c) N1–O2: NO binds to a dimer in [2+2] cycloaddition. (d) N12–O2: NO binds to a dimer in a tilt configuration. (e) N–O4: O binds to a dimer atom. Blue balls: N atoms. Red balls: O atoms. Cyan balls: Ge atoms. Sub layers are not shown for clarity. The structural parameters are listed in Table 5.1.

Table 5.1: Energies and bond lengths of non-dissociative NO adsorption products.

Configurations	Binding Energy (eV)	Bond length (Å)		
		N–O	N–Ge	O–Ge
N12–O3	0.64	1.44	1.89[a] (1), 1.87 (2)	1.74 (3)
N17–O	-0.08	1.33	1.84 (1), 1.88(7)	
N1–O3	0.67	1.41	1.96 (1)	1.76 (2)
N1–O2	1.01	1.42	1.97 (1)	1.74 (2)
N12–O2	1.00	1.44	1.83(1), 1.91(2)	1.70(2)
N–O4	-0.05	1.38		1.72 (4)
Free NO		1.10		

[a] Numbers in parentheses indicate the bound Ge atom labeled in Figure 5.3a.

dimer to adsorption of O at adjacent back bond is similar to the case of on Si(100) [322]. One plausible explanation is that the inserted N expands the dimer Ge atom from sub-layer, lowering the stress generated due to the insertion of oxygen. Such a promotive effect can also be applied on the adsorption of second NO, which has been demonstrated on Si(100), thus we will not discuss it here. For other models in which the twofold N and O atoms are isolated from each other, their binding energies are around 2.6 $\sim$ 2.9 eV. The structures with N inserting into dimer (N12O34, N12O48) are slightly energetically favorable than those with N inserting into the back bond (N17O12, N17O34).

When the N atom is coordinated by three Ge atoms, the system can be further stabilized. As shown in Figure 5.5, the N atom can incorporate into the Ge surface and be surrounded by one dimer atom and two sub-layer atoms (N157O37, N157O2,

Table 5.2: Energy and bond lengths of dissociative NO adsorption products.

Configurations	Binding Energy (eV)	Bond length (Å)	
		N-Ge	O-Ge
N-2fold			
N12O34	2.89	1.74(1), 1.72(2)	1.69(3), 1.59(4)
N12O48	2.85	1.73(1), 1.75(2)	1.62(4), 1.66(8)
N12O28	3.01	1.74(1), 1.69(2)	1.60(2), 1.68(8)
N17O12	2.65	1.69(3), 1.78(8)	1.62(1), 1.67(2)
N17O34	2.70	1.60(1), 1.68(2)	1.71(4), 1.78(8)
N-3fold			
N127O2	1.61	1.75(1), 1.91(2), 1.88(7)	1.55(2)
N127O28	2.54	1.94(7), 1.81(2), 1.80(1)	1.63(2), 1.68(8)
N157O37	3.35	1.83(1), 1.88(7), 1.88(5)	1.66(3), 1.67(7)
N157O2	1.71	1.86(5), 1.82(1), 1.90(7)	1.55(2)
N157O28	2.20	1.92(5), 1.97(7), 1.79(1)	1.62(2), 1.66(8)
N157O12	3.29	1.88(5), 1.88(7), 1.83(1)	1.65(1), 1.62(2)
N-4fold			
N1257O12	3.50	1.96(1), 2.01(2), 2.05(5),2.06(7)	1.67(1), 1.64(2)

[a] Numbers in parentheses indicate the bound Ge atoms labeled in Figure 5.3a.

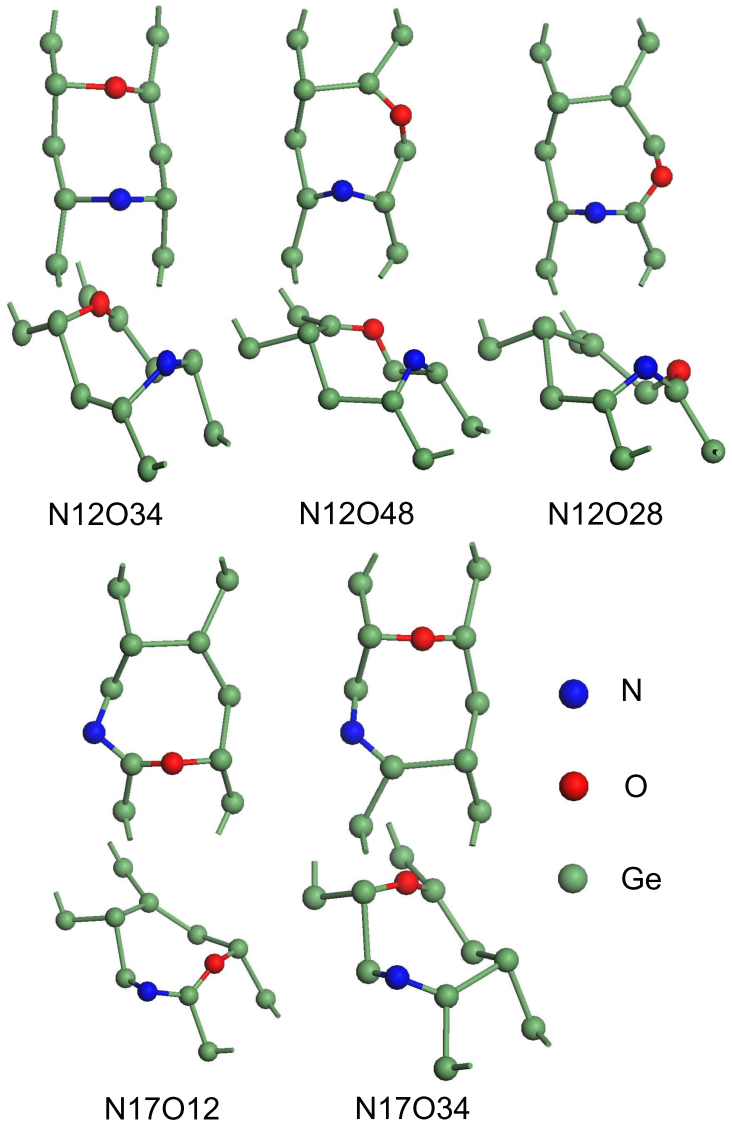

Figure 5.4: Structures of N-2fold dissociative products. Blue balls: N atoms. Red balls: O atoms. Cyan balls: Ge atoms. Sub layers are not shown for clarity. The structural parameters are listed in Table 5.2

.

N157O28 and N157O12), or two dimer atoms and one sub-layer atom (N127O2 and N127O28). The promotive effect of incorporated N to insertion of O appears again in these structures. As listed in Table 5.2, only the models with adjacent N-Ge and O-Ge

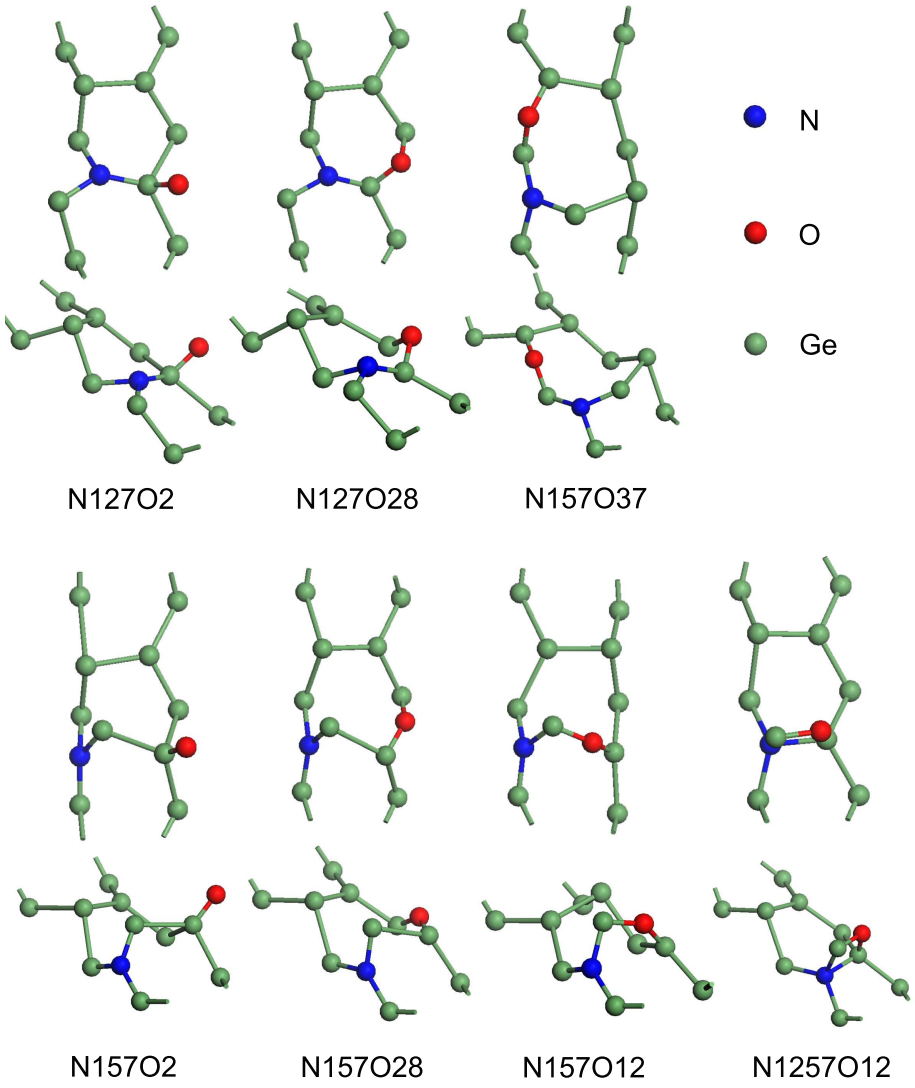

Figure 5.5: Structures of N-3fold and N-4fold dissociative products. Blue balls: N atoms. Red balls: O atoms. Cyan balls: Ge atoms. Sub layers are not shown for clarity. The structural parameters are listed in Table 5.2

.

bonds (N157O37 and N157O12) are of binding energies larger than 3 eV. There is only one exception—N127O28. It has adjacent N-Ge and O-Ge bonds, but the binding energy is less than 3 eV. Different from other N-3fold models, the joint Ge atom (2) is lower than N and O in N127O28. Because force of N-Ge and O-Ge two bonds is pushing the

joint Ge atom (2) inward rather than outward, the stress cannot be effective reduced as in other models.

Among the dissociative structures, the N-4fold model N1257O12 has the the highest binding energy. In this model, N incorporates into the subsurface, surrounding by a tetrahedron composed of two dimer atoms (1, 2) and two sub-layer atom (5, 7). Four N-Ge bonds are nearly equal in length (1.96 ∼2.06 Å), larger than that of N-2/3fold models. The top dimer atom (1) is pushed outward, producing a protrusion with the oxygen atom. The formation of fourfold coordinated nitrogen is abnormal because nitrogen is usually threefold coordinated in neutral molecule. The similar N-4fold structure has been theoretically predicted on Si(100), but its existence needs further support from experimental evidence.

5.3.1.3 Dissociation from N12–O3 and N17–O

After extensive search, we found several dissociative channels starting from nondissociative products: N12–O3, N1–O2 and N12–O2, producing the structures shown in Figure 5.4 and Figure 5.5. As shown in Figure 5.6, N12–O3 can dissociate to N12O48, N12O34 and N12O28. Although these dissociative products are highly exothermic (> 2.2 eV), their reaction barriers are relatively high (> 1 eV) to be surmounted at moderate temperature. These barriers are much higher than that of similar interdimer dissociation of NO on Si(100), where a barrier of 0.17 eV was reported [321]. In these transition states, the N–O bonds are already cleaved ($d_{N-O} \geq 1.75$ Å) before O being well bound by Ge, as indicated by at least one O–Ge bond length greater than 2.5 Å. Another non-dissociative structure N17–O may dissociate to N17O12, N17O34 and N157O34. However, these three channels have large energy barriers ($0.71 \sim 1.02$ eV) as well. Since the desorption of N17–O is almost barrierless and exothermic (binding energy: -0.08 eV),

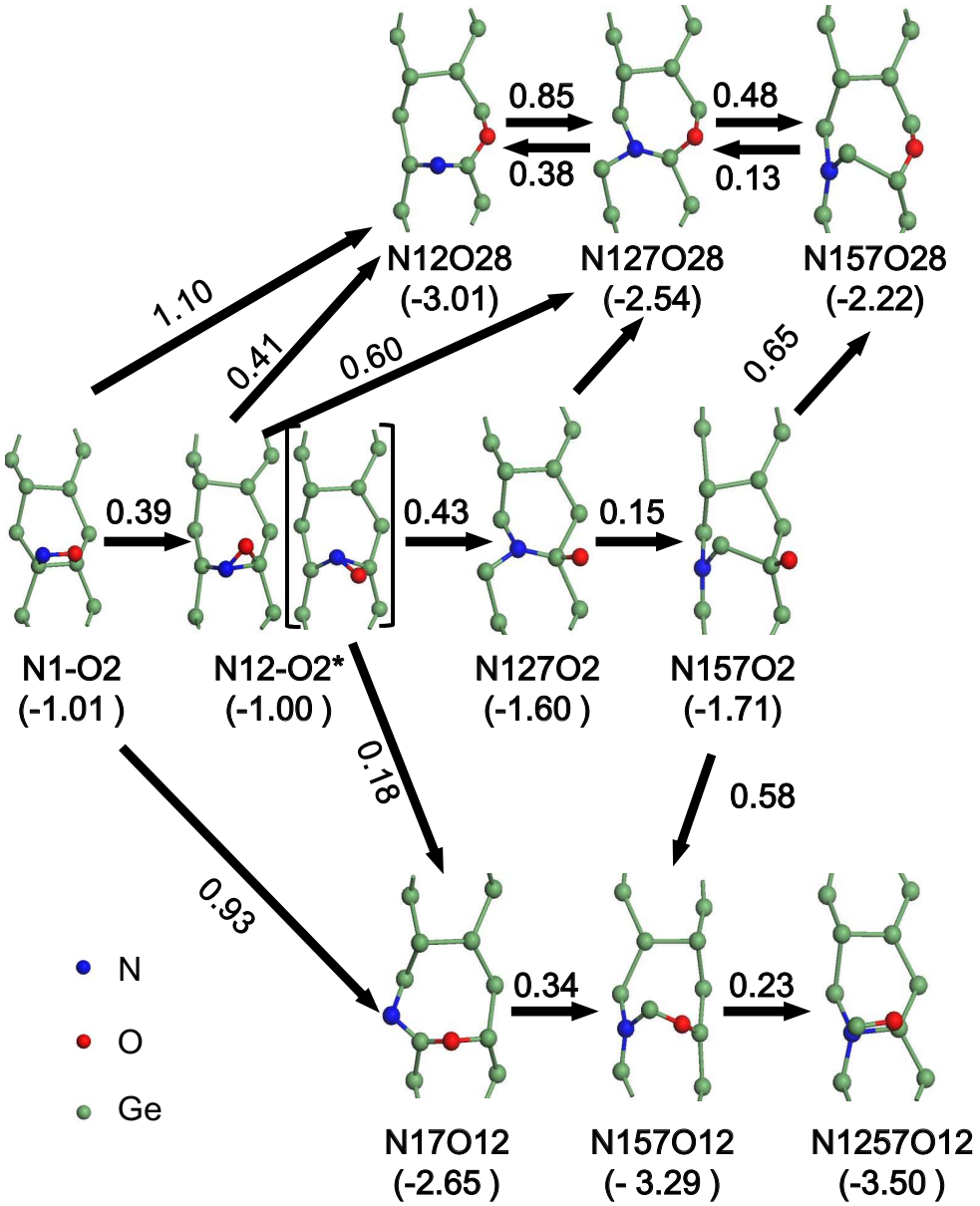

Figure 5.6: Energy variation of NO dissociation from N12–O3. The bond lengths are in the unit of Å. The energies are relative to N12–O3.

it is highly likely that NO in N17–O desorbs from the Ge surfaces before dissociation.

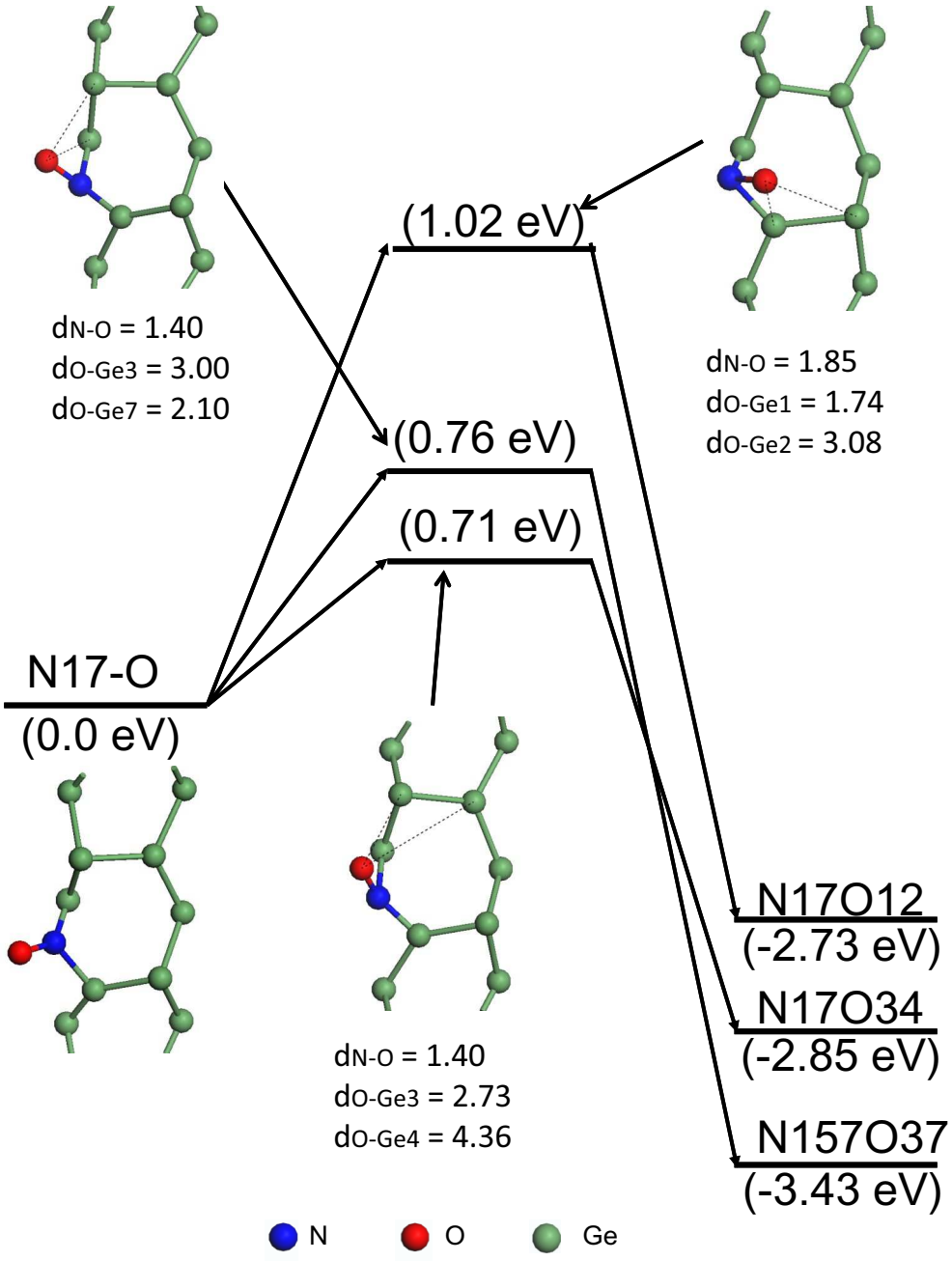

Figure 5.7: Energy variation of NO dissociation from N17–O. The bond lengths are in the unit of Å. The energies are relative to N17–O

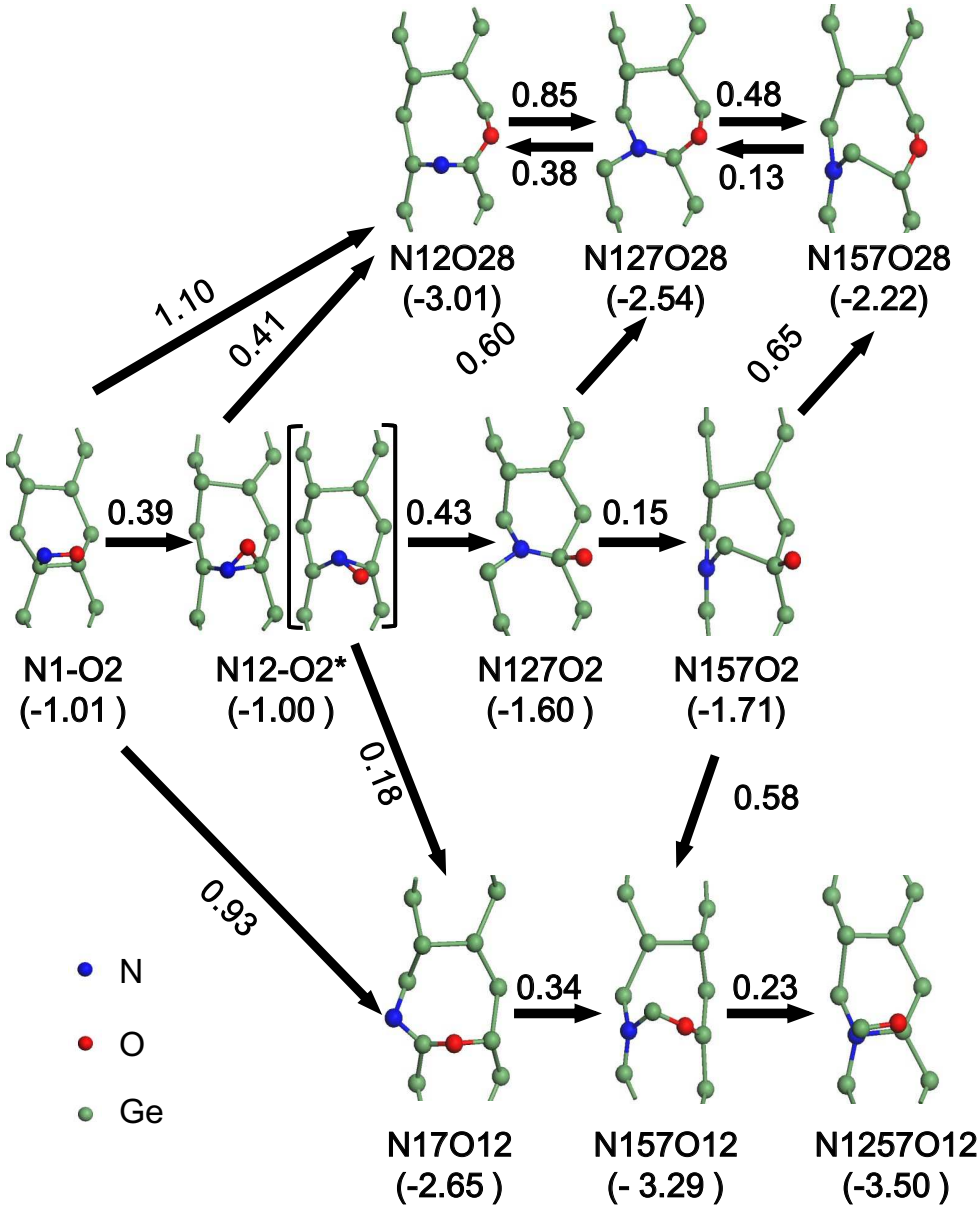

Figure 5.8: Energy variation in elementary processes of NO dissociation from N1–O2. The energies in paracenteses are relative to non-interactive system in the unit of eV. The energy barriers are given along with the reaction arrows, in the unit of eV. The structure in the square bracket is an isomer of N12–O2 with the same energy. NO tilts to an opposite direction as in N12–O2.

Table 5.3: Estimated attempting frequencies (ν) of NO dissociative processes at different temperatures.

Temperature (K)	Estimated attempting frequencies (Hz)[a]		
	E_a=0.2 eV	E_a=0.4 eV	E_a=0.6 eV
20	2×10^{-38}	8×10^{-89}	3×10^{-139}
150	1×10^{6}	2×10^{-1}	3×10^{-8}
300	2×10^{9}	1×10^{6}	4×10^{2}

[a] $\nu = \nu_0 e^{-E_a/k_B T}$, ν_0=5 THz.

5.3.1.4 Dissociation from N1–O2 and N12–O2

We moved on to search the dissociative processes from the intradimer nondissociative product N1–O2. The detailed dissociative routes are summarized in Figure 5.8. N1–O2 is one stable intradimer adduct with a binding energy of 1.01 eV. The N (or O) atom on the top of dimer atom can transfer to the neighboring back bond, leaving the O (or N) atom bridging the dimer and forming N17O12 (or N12O28). Although N1–O2 is able to directly transform to N17O12 and N17O28, the barriers are as high as 1 eV, unlikely to occur at room temperature. Alternatively, N1–O2 can first transit to an energetically degenerate intermediate N12–O2 by overcoming a small barrier of 0.39 eV. Such a twisted N–O orientation results in the lower energies of transition states from N12–O2 to N12O28 (0.41 eV) and to N17O12 (0.18 eV) than directly from N1–O2. N12–O2 can also transform to N127O2, gaining the energy of 0.60 eV after overcoming a barrier of 0.43 eV.

Once the N–O bond is cleaved, the N and O species can diffuse independently to

further stabilize the system. The N atom gradually increases its coordinate number from two in N17O12, to three in N157O12, finally to four in N1257O12. The system energy also decreases at the same time. On the other hand, N12O28 can convert to N127O28 and N157O28 to increase the N coordination number with moderate barriers. Since N127O28 and N157O28 are less stable than N12O28, the inverse process N157O28→N127O28→N12O28 is more favorable with much lower barriers (0.38 and 0.13 eV). A third dissociative product of N12–O2 is N127O2 in which N turns to be threefold coordinated while O is retained as the adatom on the top of dimer atom. The N127O2 can further diffuse into more stable structure N157O2. The O adatom in N127O2 and N157O2 can insert into the back bond (N127O28 or N157O28) or dimer bond (N157O12) with similar barriers around 0.6 eV. The conversion of O adatom to the back bond inserted O was also investigated in the case of O_2 adsorption on Ge(100), where a comparable barrier of 0.8 eV was reported [149].

In Figure 5.8, the attempting frequencies of dissociative processes can be estimated using Arrhenius equation: $\nu = \nu_0 e^{-E_a/k_B T}$, where ν_0, E_a, k_a and T refer to the prefactor, energy barrier, Boltzman constant and temperature. If the prefactor is assumed to be 5 THz [323] as a typical phonon frequency of bulk Ge, the attempting frequencies for the barriers of 0.2, 0.4 and 0.6 eV at different temperatures are listed in Table 5.3. One can see that at 20 K, the rates of all the dissociative processes in Figure 5.8 are negligible, NO cannot dissociate at such a low temperature. This is in contrast to NO on Si(100), where NO dissociation at 20 K was observed. 5.3 indicates that NO on Ge(100) may dissociate at higher temperature, and the most favorable pathways could be: N1–O2→N12–O2*→N17O12→N157O12→N1257O12 and N12-O2→N12O28. Two O-adatom structures: N127O2 and N157O2 may be trapped due to high barriers to next step of dissociation. Their existence might be detected by surface tools such as STM

and HRXPS.

5.3.2 Dimeric adsorption

If the dosage of NO increases, the NO molecules may first dimerize, then react with the Ge(100) surface. Figure 5.9 shows the optimized geometries of 18 proposed dimeric NO adsorption products. Among them, the OO group generally has the highest binding energies. OO6 is most thermodynamically favorable with a formation energy 4.05 eV with respect to the non-interactive system. In this structure, two N-O bonds completely break, and two O atoms insert into the dimer. Two N atoms form N_2, making the reaction extremely exothermic. OO2 and OO4 also release N_2, but the residual O atoms are on the top of dimer atoms with the less formation energies of around 1.9 eV. Their much less exothermicity compared to OO6 can only be ascribed to the higher energy of the dangling O adspecies. These O atoms may further insert into the dimers or back bonds, similar to OO6. In OO1, OO3 and OO5, the NO dimers retain their ONNO chain structures, with each O end binding to one dimer atom. They can be considered as the intermediate states in the release process of N_2. Although there is no N_2 released, their formation energies are surprisingly close to OO2 and OO4.

To interpret the thermodynamics in these processes, we trace the evolution of bond lengths (Table 5.4). First, the bond length of N–N in free cis-NO dimer is 1.91 Å. It is less than the experimental value (2.23 Å), as DFT systematically underestimates the N-N bond length. Nevertheless, this value indicates a weak bonding between two NO molecules. After adsorption, as in OO1, OO3 and OO5, the bond length of N-N changes to 1.24 Å, suggesting that the interaction between two N atoms transits from a weak bonding to a double bond. At the same time, the N-O bond lengths increase from 1.18

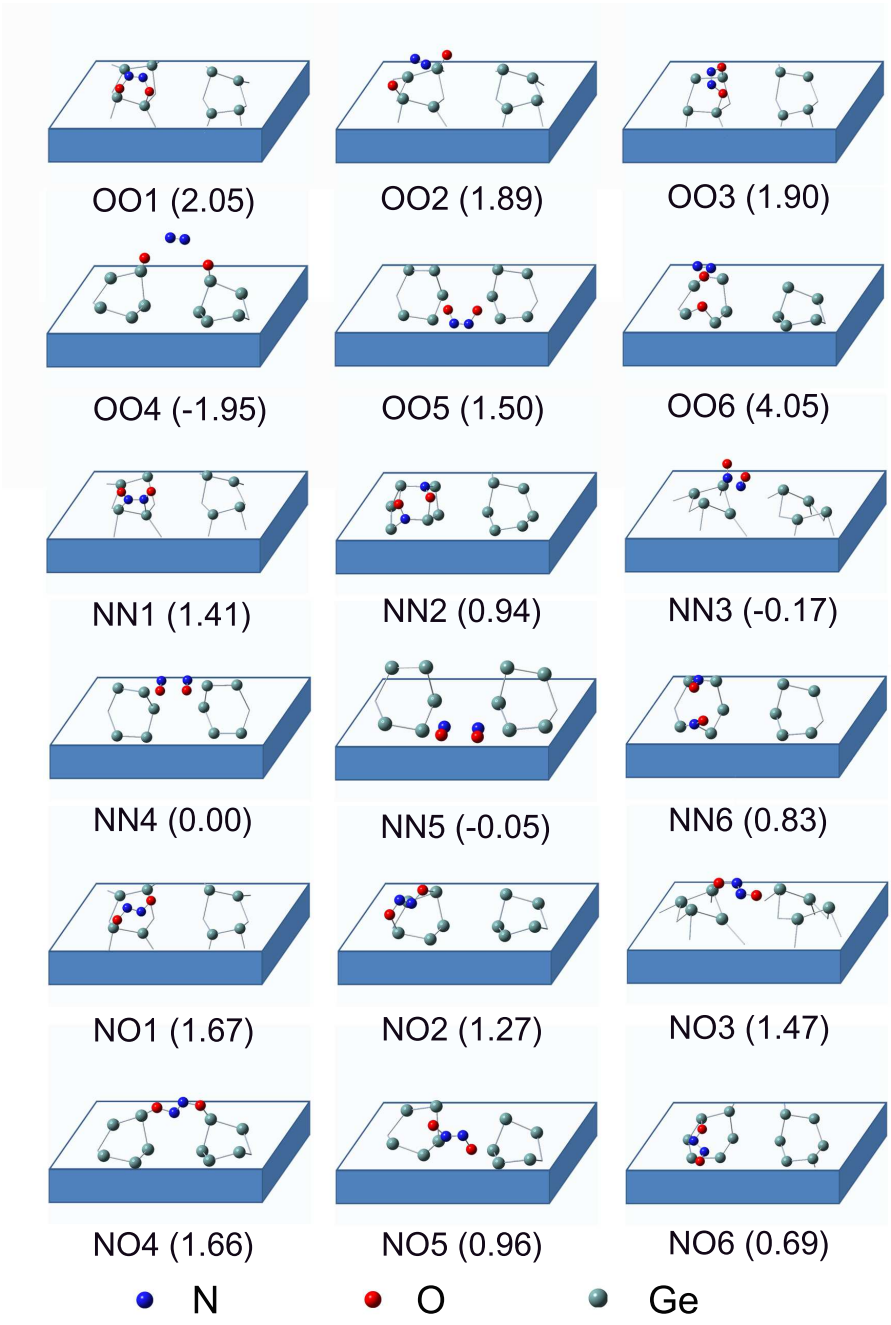

Figure 5.9: Dimeric adsorption products of NO on the Ge(100) surface. The energies given in paracenteses are in the unit of eV. Sub-layer atoms are not shown for clarity.

Table 5.4: Bond lengths in optimized geometries of 20 proposed dimeric NO adsorption products.[a]

Configurations	N–N bond length (Å)	N–O Bond length (Å)	
		Terminal O	Ge bound O
OO1	1.26		1.41
OO2	1.12		
OO3	1.26		1.40
OO4	1.12		
OO5	1.26		1.39
OO6	1.12		
NN1	1.41	1.24	
NN2			1.39
NN3	1.67	1.21	
NN4	2.27	1.26	
NN5	2.25	1.20	
NN6		1.28	1.40
NO1	1.31	1.29	1.36
NO2	1.28		1.36
NO3	1.32	1.26	1.40
NO4	1.27		1.40
NO5	1.31	1.25	1.41
NO6	1.41	1.24	1.37
Free NO dimer	1.91	1.18	

[a] Blank entries mean that there is no bond between those two atoms.

Å in free dimer to 1.40 Å after adsorption, implying the bond order decrease from 2.5 to 1. Two O atoms also form single O-Ge bond with dimer atoms. This is different from the case of monomeric NO adsorption, where the O is almost inactive toward the surface dimer. Thus, the formation of N=N bond is the key factor in dissociative adsorption of NO dimer in OO configuration. If OO1, OO3 and OO5 continue to desorb N_2, the energy releasing from formation of N_2 from N=N bond will be canceled out by the cleavage of two N-O single bonds. Thus OO1-OO5 states have similar energies regardless of N_2 release. Further theoretical calculations are under way to explore the mechanism for these N_2 release reactions.

Compared to the OO configurations, NN1-6 states both have the lower binding energies. NN1 is of the highest energy (1.41 eV). The bond length of NN (1.41 Å) indicates that NN form single bonds rather than double bonds like in OO1, OO3 and OO5 configurations. The N-O weakens to a double bonding with a length of 1.24 Å. In NN2 and NN6, the NN bonds break, and two NO molecules are adsorbed separately on the surface. For NN3, NN4 and NN5, two NO molecules fail to form any substantially bound adsorption structures, nor to retain its ONNO chain structures. It is attributable to the large tensile force of ONNO chain because of the long distance between two adsorbing sites. Thus we concluded that the NO dimers with NN attaching configurations cannot form any energetically competitive adsorption structures.

Unlike NN and OO configurations, NO1-NO6 configurations have the modest energy compared to OO or NN states. After geometric optimization, NO2 and NO4 transit to a trans-ONNO chain states, with two OO ends connecting the Ge atoms. Since the similar structures in OO group (OO2 and OO4) release the N_2 molecules, NO2 and NO4 are also possible to release N_2 as the free trans- and cis- isomers of NO dimer have small

energy difference. In NO1, NO3, NO5 and NO6, one O and one N atom are bound to Ge atoms, retaining the trans-ONNO chain. In these states, the NN bond lengths (1.31∼1.41 Å) show that the interaction between NN are enhanced but weaker than the double bond. The NO bond lengths depends on the coordination number of its O atom: the N–O bonds consisting of terminal O atoms are single bonds of the lengths greater than 1.36 Å, whereas the other N–O bonds consisting of Ge bound O atoms are double bonds with the length in (1.20∼1.29 Å). These four states, with one O atom intact with Ge surface, are probably responsible to release the N_2O as reported [199, 200].

To enhance the incorporation efficiency of N elements in nitridation of Ge, any reaction channel releasing N_2 needs to be suppressed. Fortunately, in an view of energy gaining per NO molecule, dimeric adsorption is less exothermic than the monomeric adsorption. For example, the reaction energy of most exothermic dimeric product OO6 (4.05/2 = 2.02 eV), is less than that of the typical twofold-N dissociative products N12O28 (3.01 eV) or N12O48 (2.85 eV), let alone other N-3fold and N-4fold models. Nevertheless, the formation of N_2 is consistent with the observation of TPD spectra [318,324]. Since the monomeric dissociations are thermodynamically favorable, one can optimize the nitridation processes by increasing the reaction temperature and decreasing NO concentration.

5.4 Conclusion

In conclusion, we have elucidated the atomic processes of NO dissociation on the Ge(100) surface using DFT calculations. Six non-dissociative adsorption structures were found with binding energies varying from slightly negative to 1 eV. These non-dissociative intermediates can transform into various dissociative products, resulting in the increase

of system binding energies as well as the coordination number of N and O atoms. The dissociated N atom first bridges the dimer or back bond, followed by migrating into a threefold coordination site. Finally N diffuses into a fourfold site, pushing a dimer Ge atom outwards. The transition state search indicates that the dissociative processes are unlikely to occur on Ge(100) at 20 K, in contrast to the high reactivity of NO on Si(100). The dissociation is visible at 150 K. However, the interdimer dissociation route is unfavorable due to the high energy barriers. When high coverage of NO molecules are adsorbed on Ge(100), NO may dimerize first and bind on Ge(100) in the form of ONNO chain. The binding configurations of cis-ONNO chain with two O attached are responsible for the release of N_2 observed by TPD. Since the release of N_2 is less exothermic than monomeric NO dissociation, such dimeric processes can be suppressed by lowering dosing mount of NO and/or increasing the temperature. Our study provided a detailed understanding of the atomic processes of NO dissociation on Ge(100). The results offer useful information to optimize the oxynitridation of Ge(100) by nitric oxide.

Chapter 6

Conclusion

Driven by the potential application of Ge in microelectronics, molecular devices and catalysis, this study focused on the adsorption of heterocyclic molecules, CO and NO on Ge(100). This chapter summarizes the main achievements and findings, limitation and recommendation for future work.

6.1 Summary

Imaging molecular orbitals is critical to understand the intrinsic electronic prosperities of the molecules. However, imaging molecular orbitals on semiconductor surfaces is generally difficult due to strong coupling between surface states and adsorbed molecules. In Chapter 3, we successfully imaged the molecular orbitals of pyridazine adsorbed on Ge(100). Two flower-like features were captured in filled STM images and assigned to different structures accordingly. One with three lobes in the trough between dimer rows was assigned to pyridazine datively bound to a Ge dimer atom via a N→Ge bond. The other four-lobe feature on a dimer was proposed to be pyridazine datively bound to a Ge dimer via double N→Ge bonds. The orbital resolution was attributable to the self decoupling of molecular orbitals from surface state because pyridazine stands up at Ge(100) via dative bonding. The assignment of the two features was consistent with the vibrational data from HREELS, as well as the theoretical predictions Our results showed that the molecular orbitals can be imaged on clean semiconductor surfaces. It is also demonstrated that orbital resolved STM is powerful in determining the surface

chemistry of semiconductor surfaces, inspiring future application of this technique in the field of surface chemistry.

Study of CO adsorption on Ge(100) is helpful to understand the role of Ge in catalysis. In Chapter 4, our DFT study showed that CO is exclusively bound to the Ge(100) dimer in a standing configuration with C end attached to a lower dimer Ge atom. The adsorption is weak and the CO bond is partially elongated after adsorption. The orbital analysis indicated that the Ge-CO interaction is attributable to the Ge 4pz-C 2s σ bonding, or 3σ, 4σ of CO donation to Ge. The repulsive energy between neighboring adsorbed CO molecules is less than 1 kcal/mol. The energy profile of adsorption pathway demonstrated that the adsorption is barrierless. The diffusion barrier of CO on Ge(100) surface is 14 kcal/mol. These results may be useful to the study of Ge in catalysis.

Reaction of NO on Ge surfaces is a potentially effective nitridation method of Ge surfaces, creating high quality and high-κ interface in Ge-based microelectronics. In Chapter 5, we systematically investigated the initial stage of NO reacting with Ge, including monomeric and dimeric adsorption. Six non-dissociative adsorption products of monomeric NO were found. These non-dissociative intermediates can transform into various dissociative products. However, the interdimer dissociation route is unfavorable due to the high energy barriers. The intradimer dissociation will occur at a temperature high than 20 K. This explains the puzzle that EELS did not detected any NO stretching modes. When high coverage of NO molecules is adsorbed on Ge(100) surface, NO may dimerize first and bind on Ge(100) in the form of ONNO chain. The binding configurations of cis-ONNO chain with two O attached are responsible for the release of N_2 observed by TPD. Our study provided a detailed understanding of the atomic processes of NO dissociation on Ge(100). The results offer useful information to optimize the

oxynitridation of Ge(100) by nitric oxide.

6.2 Limitations and future work

Although some molecular orbitals of pyridazine adsorbed on Ge(100) has been imaged, the investigation was limited to the HOMOs. The constant current STM images roughly reflect the cumulative density of states from E_F to E_F+eV_b. Multiple molecular orbitals need to be resolved using CITS technique, which is unfortunately unavailable on our STM. Future investigations using STM machines with CITS functionality will be desirable to achieve multiple-orbital resolution.

CO adsorption on Ge(100) has only been investigated using theoretical simulation. Although STM investigations on adsorption sites of CO on Ge(100) have been done by Choi et al [325], the desorption and diffusion of CO molecules on Ge(100) are also interesting. To verify the predicted electron-transfer mechanism between CO and Ge(100), XPS is highly recommended to observe the shift of C 1s binding energy of CO upon adsorption. HREELS could be employed to detect the C-O stretching frequency, which could be compared with that of gaseous CO.

The adsorption and dissociation of monomeric NO on Ge(100) were studied by investigated the stable geometric structures and relative transition states between them. For the dimeric ONNO chain, only stable products were studied. The reaction pathways from initial interaction-free or physisorbed states are yet to be searched. Experimentally, the puzzle of missed N–O stretching frequency would better to be revisited. Delicate HREELS studies of NO on Ge(100) at varied temperatures and coverage may solve this puzzle. The N-4fold product with N being fourfold coordinated could be checked using

XPS to detect the shift of N 1s binding energy.

Due to the time constraint, only pyridazine as the case of heterocycles were studied. A complete understanding of the surface chemistry of multifunctional heterocycles needs more studies, to survey the reactions involving different function groups. In addition, other simple gaseous oxides such as N_2O, NO_2 are also highly interesting and worthy to be studied in future.

To conclude, this study has contributed to the surface chemistry of multifunctional heterocycles and gaseous molecules on Ge. We showed that orbital resolved STM is a powerful characterization tool in studying surface chemistry of semiconductors. We elucidated the reactions of CO and NO on Ge(100), which will be helpful to understand the role of Ge in catalysis and nitridation processes. Our results will be useful to optimize Ge-containing catalysts and nitridation efficiency of Ge surfaces.

References

[1] M. Bosi and G. Attolini, *Prog. Cryst. Growth Charact. Mater.*, **2010**, *56*(3-4), 146–174.

[2] G. E. Moore, *Electronics*, **1965**, *38*(8), 114–117.

[3] P. Packan, S. Akbar, M. Armstrong, D. Bergstrom, M. Brazier, H. Deshpande, K. Dev, G. Ding, T. Ghani, O. Golonzka, et al.; High performance 32nm logic technology featuring 2nd generation high-k+ metal gate transistors; In *Electron Devices Meeting (IEDM), 2009 IEEE International*, pages 1–4. IEEE, 2009.

[4] P. W. Loscutoff and S. F. Bent, *Annu. Rev. Phys. Chem.*, **2006**, *57*, 467–495.

[5] B. Medellin, R. Gomez, and G. del Angel, *Catal. Today*, **2010**, *150*(3-4), 368–372.

[6] N. Gyorffy, I. Bakos, S. Szabo, L. Toth, U. Wild, R. Schloegl, and Z. Paal, *J. Catal.*, **2009**, *263*(2), 372–379.

[7] L. Gwendoline, M. Corina, E. Catherine, M. Patrice, and A. Michael., *Langmuir*, **2004**, *20*(24), 10612–10616.

[8] G. P. Romanova and I. I. Stepko, *Dopovidi Akademii Nauk Ukrainskoi Rsr*, **1958**, (No. 6), 585–587.

[9] S. S. M. Concepcion, G. R. Joaquin, P. M. Grazia, and B. Javier, *J. Mol. Catal. A: Chem.*, **1996**, *108*(2), 95–105.

[10] T. Komatsu, S. Hyodo, and T. Yashima, *J. Phys. Chem. B*, **1997**, *101*(28), 5565–5572.

[11] D. Haneman, *Phys. Rev.*, **1961**, *121*, 1093–1100.

[12] J.C. Phillips, *Surf. Sci.*, **1973**, *40*(3), 459–469.

[13] W. A. Harrison, *Surf. Sci.*, **1976**, *55*(1), 1–19.

[14] R. Seiwatz, *Surf. Sci.*, **1964**, *2*(0), 473 – 483.

[15] J. E. Northrup, *Phys. Rev. Lett.*, **1985**, *54*, 815–818.

[16] R. E. Schlier and H. E. Farnsworth, *J. Chem. Phys.*, **1959**, *30*(4), 917–926.

[17] R. M. Tromp, R. J. Hamers, and J. E. Demuth, *Phys. Rev. Lett.*, **1985**, *55*, 1303–1306.

[18] R. J. Hamers, R. M. Tromp, and J. E. Demuth, *Phy. Rev. B*, **1986**, *34*, 5343–5357.

[19] D. J. Chadi, *Phys. Rev. Lett.*, **1979**, *43*, 43–47.

[20] C. Yang and H. C. Kang, *J. Chem. Phys.*, **1999**, *110*(22), 11029–11037.

[21] P. Lal, A. V. Teplyakov, Y. Noah, M. J. Kong, G. T. Wang, and S. F. Bent, *J. Chem. Phys.*, **1999**, *110*(21), 10545–10553.

[22] A. Fink, D. Menzel, and W. Widdra, *J. Phys. Chem. B*, **2001**, *105*(18), 3828–3837.

[23] A. Kim, D. S. Choi, J. Y. Lee, and S. Kim, *J. Phys. Chem. B*, **2004**, *108*(10), 3256–3261.

[24] G. Lee and K. S. Chae, *J. Korean Phys. Soc.*, **2006**, *48*(3), 437–440.

[25] A. Kim, S. S. Bae, D. S. Choi, and S. H. Kim, *J. Phys. Chem. C*, **2008**, *112*(5), 1493–1497.

[26] X. Lu, M. P. Zhu, and X. L. Wang, *J. Phys. Chem. B*, **2004**, *108*(22), 7359–7362.

[27] X. L. Fan, C. C. Sun, Y. F. Zhang, and W. M. Lau, *J. Phys. Chem. C*, **2010**, *114*(5), 2200–2207.

[28] X. L. Fan, J. X. Min, C. C. Sun, Q. Chi, and Q. Z. Cheng, *Acta. Chim. Sinica.*, **2010**, *68*(16), 1589–1596.

[29] X. L. Fan, Q. Cheng, Q. Chi, Y. F. Zhang, and W. M. Lau, *J. Phys. Chem. C*, **2010**, *114*(34), 14473–14481.

[30] R. J. Hamers, J. S. Hovis, C. M. Greenlief, and D. F. Padowitz, *Jpn. J. Appl. Phys. Part 1*, **1999**, *38*(6B), 3879–3887.

[31] S. W. Lee, J. S. Hovis, S. K. Coulter, R. J. Hamers, and C. M. Greenlief, *Surf. Sci.*, **2000**, *462*(1-3), 6–18.

[32] J. H. Cho and L. Kleinman, *Phy. Rev. B*, **2003**, *67*(11), 115314.

[33] E. German, I. Lopez-Corral, A. Juan, and G. Brizuela, *Appl. Surf. Sci.*, **2010**, *256*(21), 6237–6245.

[34] P. Prayongpan, D. S. Stripe, and C. M. Greenlief, *Surf. Sci.*, **2008**, *602*(2), 571–578.

[35] A. Y. Kim, J. H. Choi, D. H. Kim, and S. H. Kim, *J. Phys. Chem. C*, **2009**, *113*(32), 14311–14315.

[36] Y. J. Hwang, E. K. Hwang, D. H. Kim, A. S. Kim, S. K. Hong, and S. H. Kim, *J. Phys. Chem. C*, **2009**, *113*(4), 1426–1432.

[37] Y. J. Hwang, A. Kim, E. K. Hwang, and S. H. Kim, *J. Am. Chem. Soc.*, **2005**, *127*(14), 5016–5017.

[38] D. H. Kim, Y. J. Hwang, J. G. Ryou, S. H. Kim, and S. K. Hong, *Surf. Sci.*, **2011**, *605*(15-16), 1438–1444.

[39] F. J. Xu, Q. J. Cai, E. T. Kang, K. G. Neoh, and C. X. Zhu, *Organometallics*, **2005**, *24*(7), 1768–1771.

[40] A. Kim, J. Y. Maeng, J. Y. Lee, and S. H. Kim, *J. Chem. Phys.*, **2002**, *117*(22), 10215–10222.

[41] R. Miotto and A. C. Ferraz, *Surf. Sci.*, **2002**, *513*(3), 422–430.

[42] J. H. Cho and L. Kleinman, *J. Chem. Phys.*, **2003**, *119*(5), 2820–2824.

[43] X. L. Fan, Q. Z. Cheng, S. Ahmad, Y. F. Zhang, and W. M. Lau, *Chem. Phys. Lett.*, **2011**, *514*(1-3), 109–113.

[44] G. Lee, K. S. Chae, E. J. Cho, and W. D. Kim, *Chem. Phys. Lett.*, **2011**, *502*(4-6), 198–201.

[45] P. W. Loscutoff, K. T. Wong, and S. F. Bent, *Surf. Sci.*, **2010**, *604*(19-20), 1791–1799.

[46] P. W. Loscutoff, K. T. Wong, and S. F. Bent, *J. Phys. Chem. C*, **2010**, *114*(33), 14193–14201.

[47] C. Mui, M. A. Filler, S. F. Bent, and C. B. Musgrave, *J. Phys. Chem. B*, **2003**, *107*(44), 12256–12267.

[48] M. A. Filler, C. Mui, C. B. Musgrave, and S. F. Bent, *J. Am. Chem. Soc.*, **2003**, *125*(16), 4928–4936.

[49] M. Kadodwala; Adsorption of aromatic compounds on si(100)-(2x1), si(111)-(7x7) and ge(100)-(2x1).; In *Abstracts of Papers, 224th ACS National Meeting, Boston, MA, United States, August 18-22, 2002*, pages COLL–150–. American Chemical Society, 2002.

[50] M. A. Filler, C. B. Musgrave, and S. F. Bent, *J. Phys. Chem. C*, **2007**, *111*(4), 1739–1746.

[51] A. V. Teplyakov, P. Lal, Y. A. Noah, and S. F. Bent, *J. Am. Chem. Soc.*, **1998**, *120*(29), 7377–7378.

[52] C. Mui, S. F. Bent, and C. B. Musgrave, *J. Phys. Chem. A*, **2000**, *104*(11), 2457–2462.

[53] R. Konecny and D. J. Doren, *Surf. Sci.*, **1998**, *417*(2-3), 169–188.

[54] S. W. Lee, L. N. Nelen, H. Ihm, T. Scoggins, and C. M. Greenlief, *Surf. Sci.*, **1998**, *410*(2/3), L773–L778.

[55] X. Lu, M. P. Zhu, X. L. Wang, and Q. E. Zhang, *J. Phys. Chem. B*, **2004**, *108*(14), 4478–4484.

[56] G. T. Wang, C. Mui, C. B. Musgrave, and S. F. Bent, *J. Am. Chem. Soc.*, **2002**, *124*(30), 8990–9004.

[57] A. Fink, R. Huber, and W. Widdra, *J. Chem. Phys.*, **2001**, *115*(6), 2768–2775.

[58] J. H. Cho, K. S. Kim, and Y. Morikawa, *J. Chem. Phys.*, **2006**, *124*(2), 024716.

[59] A. V. Teplyakov, M. J. Kong, and S. F. Bent, *J. Chem. Phys.*, **1998**, *108*(11), 4599–4606.

[60] R. B. Woodward and R. Hoffmann, *J. Am. Chem. Soc.*, **1965**, *87*(2), 395–397.

[61] Z. Guo and X. Lu, *J. Phys. Chem. B*, **2006**, *110*(21), 10461–10466.

[62] R. J. Hamers, S. K. Coulter, M. D. Ellison, J. S. Hovis, D. F. Padowitz, M. P. Schwartz, C. M. Greenlief, and J. N. Russell, *Acc. Chem. Res.*, **2000**, *33*(9), 617–624.

[63] V. N. Khabashesku, K. N. Kudin, and J. L. Margrave, *Russ. Chem. Bull.*, **2001**, *50*(1), 20–28.

[64] M. Nagao, H. Umeyama, K. Mukai, Y. Yamashita, J. Yoshinobu, K. Akagi, and S. Tsuneyuki, *J. Am. Chem. Soc.*, **2004**, *126*(32), 9922–9923.

[65] R. L. Hayes and M. E. Tuckerman, *J. Am. Chem. Soc.*, **2007**, *129*(40), 12172–12180.

[66] J. S. Hovis, H. Liu, and R. J. Hamers, *Surf. Sci.*, **1998**, *402*(1-3), 1–7.

[67] L. Li, C. Tindall, O. Takaoka, Y. Hasegawa, and T. Sakurai, *Phy. Rev. B*, **1997**, *56*(8), 4648–4655.

[68] M. Shimomura, M. Munakata, A. Iwasaki, M. Ikeda, T. Abukawa, K. Sato, T. Kawawa, H. Shimizu, N. Nagashima, and S. Kono, *Surf. Sci.*, **2002**, *504*(1-3), 19–27.

[69] F. Matsui, H. W. Yeom, I. Matsuda, and T. Ohta, *Phy. Rev. B*, **2000**, *62*(8), 5036–5044.

[70] J. H. Cho, L. Kleinman, C. T. Chan, and K. S. Kim, *Phy. Rev. B*, **2001**, *63*(7), 073306.

[71] T. Mineva, R. Nathaniel, K. L. Kostov, and W. Widdra, *J. Chem. Phys.*, **2006**, *125*(19), 194712.

[72] P. M. Ryan, L. C. Teague, and J. J. Boland, *J. Am. Chem. Soc.*, **2009**, *131*(19), 6768–6774.

[73] P. M. Ryan, L. C. Teague, D. E. Meehan, and J. J. Boland, *J. Am. Chem. Soc.*, **2011**, *133*(36), 14287–14292.

[74] Y. J. Xu and J. Q. Li, *Appl. Surf. Sci.*, **2006**, *252*(16), 5855–5860.

[75] S. J. Jung, Y. S. Youn, H. Lee, K. J. Kim, B. S. Kim, and S. H. Kim, *J. Am. Chem. Soc.*, **2008**, *130*(11), 3288–3289.

[76] S. M. Cohen, Y. M. L. Yang, E. Rouchouze, T. Jin, and M. P. D'Evelyn, *J. Vac. Sci Technol. A*, **1992**, *10*(4, Pt. 3), 2166–2171.

[77] C. Bater, M. Sanders, and J. H. Craig, *Surf. Sci.*, **2000**, *451*(1-3), 226–231.

[78] C. M. Greenlief and P. Prayongpan; Density functional study of ethylamine and allylamine on si(100)-2x1 and ge(100)-2x1 surfaces.; In *Abstracts of Papers, 236th ACS National Meeting, Philadelphia, PA, United States, August 17-21, 2008*, pages COLL–345–. American Chemical Society, 2008.

[79] C. M. Greenlief and P. Prayongpan; Adsorption of ethylamine and allylamine on si(100)-2x1 and ge(100)-2x1 surfaces.; In *Abstracts, 43rd Midwest Regional Meeting of the American Chemical Society, Kearney, NE, United States, October 8-11*, pages MWRM–071–. American Chemical Society, 2008.

[80] P. Prayongpan and C. M. Greenlief, *Surf. Sci.*, **2009**, *603*(7), 1055–1069.

[81] A. Kim, M. A. Filler, S Kim, and S. F. Bent, *J. Phys. Chem. B*, **2005**, *109*(42), 19817–19822.

[82] A. J. Keung, M. A. Filler, and S. F. Bent; Tertiary amide chemistry at the ge(100)-2x1 interface.; In *Abstracts of Papers, 229th ACS National Meeting, San Diego, CA, United States, March 13-17, 2005*, pages COLL–393–. American Chemical Society, 2005.

[83] A. J. Keung, M. A. Filler, and S. F. Bent, *J. Phys. Chem. C*, **2007**, *111*(1), 411–419.

[84] G. T. Wang, C. Mui, J. F. Tannaci, M. A. Filler, C. B. Musgrave, and S. F. Bent, *J. Phys. Chem. B*, **2003**, *107*(21), 4982–4996.

[85] P. Ardalan, N. Davani, and C. B. Musgrave, *J. Phys. Chem. C*, **2007**, *111*(9), 3692–3699.

[86] S. N. Yang, Y. W. Kim, S. M Park, H. S. Lim, and H. G. Lee, *J. Phys. Chem. C*, **2011**, *115*(18), 9131–9135.

[87] S. N. Yang, Y. W Kim, S. M. Park, K. J. Kim, and H. G. Lee, *Chem.-Asian. J.*, **2011**, *6*(9), 2362–2367.

[88] S. N. Yang, Y. C. Park, J. W. Kim, and H. G. Lee, *J. Phys. Chem. C*, **2011**, *115*(39), 19287–19292.

[89] Y. S. Youn, S. J. Jung, H. G. Lee, and S. H. Kim, *Langmuir*, **2009**, *25*(13), 7438–7442.

[90] J. S. Kachian, S. J. Jung, S. H. Kim, and S. F. Bent, *Surf. Sci.*, **2011**, *605*(7-8), 760–769.

[91] H. G. Lee, Y. S. Youn, S. N. Yang, S. J. Jung, and S. H. Kim, *Bull. Korean Chem. Soc.*, **2010**, *31*(11), 3217–3220.

[92] Y. S. Youn, H. G. Lee, and S. H. Kim, *ChemPhysChem*, **2010**, *11*(2), 354–356.

[93] Y. S. Youn, K. J. Kim, B. S. Kim, D. H. Kim, H. G. Lee, and S. H. Kim, *J. Phys. Chem. C*, **2011**, *115*(3), 710–713.

[94] S. K. Hong, Y. E. Cho, J. Y. Maeng, and S. H. Kim, *J. Phys. Chem. B*, **2004**, *108*(39), 15229–15232.

[95] H. J. Kim and J. H. Cho, *J. Chem. Phys.*, **2004**, *120*(17), 8222–8225.

[96] J. Y. Lee, S. J. Jung, S. Hong, and S. H. Kim, *J. Phys. Chem. B*, **2005**, *109*(1), 348–351.

[97] S. J. Jung, J. Y. Lee, and S. H. Kim; Adsorption structure of purine on ge(100)-2x1 surface.; In *Abstracts of Papers, 227th ACS National Meeting, Anaheim, CA, United States, March 28-April 1, 2004*, pages COLL–252–. American Chemical Society, 2004.

[98] G. B. D. Rousseau, V. Dhanak, and M. Kadodwala, *Surf. Sci.*, **2001**, *494*(3), 251–264.

[99] S. M. Jeon, S. J. Jung, H. D. Kim, D. K. Lim, H. G Lee, and S. H. Kim, *J. Phys. Chem. B*, **2006**, *110*(43), 21728–21734.

[100] H. G. Lee, S. M. Jeon, S. J. Jung, D. K. Lim, J. H. Choi, and S. H. Kim; Bond character of thiophene on ge(100): Effects of coverage and temperature.; In *Abstracts of Papers, 233rd ACS National Meeting, Chicago, IL, United States, March 25-29, 2007*, pages COLL–586–. American Chemical Society, 2007.

[101] H. G. Lee, S. M. Jeon, H. D. Kim, D. K. Lim, S. J. Jung, and S. H. Kim, *J. Phys.: Condens. Matter.*, **2008**, *20*(13), 135006.

[102] S. M. Jeon, S. J. Jung, D. K. Lim, H. D. Kim, H. G. Lee, and S. H. Kim, *J. Am. Chem. Soc.*, **2006**, *128*(19), 6296–6297.

[103] S. M. Jeon, S. J. Jung, H. D. Kim, D. K. Lim, H. G. Lee, and S. H. Kim, *AIP Conference Proceedings*, **2007**, *879*(Pt. 2, Synchrotron Radiation Instrumentation, Part 2), 1649–1654.

[104] S. M. Jeon, H. G. Lee, S. J. Jung, D. K. Lim, S. Il Kim, and S. H. Kim; Self-induced 1-d molecular chain growth of thiophene on ge(100).; In *Abstracts of Papers, 233rd ACS*

National Meeting, Chicago, IL, United States, March 25-29, 2007, pages COLL–275–. American Chemical Society, 2007.

[105] S. J. Jung, J. Y. Lee, S. K. Hong, and S. H. Kim, *J. Phys. Chem. B*, **2005**, *109*(51), 24445–24449.

[106] G. T Wang, C. Mui, C. B. Musgrave, and S. F. Bent, *J. Phys. Chem. B*, **2001**, *105*(50), 12559–12565.

[107] J. S. Kachian and S. F. Bent, *J. Am. Chem. Soc.*, **2009**, *131*(20), 7005–7015.

[108] J. S. Kachian, K. T. Wong, and S. F. Bent, *Acc. Chem. Res.*, **2010**, *43*(2), 346–355.

[109] S. S. Bae, S. H. Kim, and J. W. Kim, *Langmuir*, **2009**, *25*(1), 275–279.

[110] D. H. Kim, D. S. Choi, S. K. Hong, and S. H. Kim, *J. Phys. Chem. C*, **2008**, *112*(19), 7412–7419.

[111] D. H. Kim, D. S. Choi, A. S. Kim, S. S. Bae, S. K. Hong, and S. H. Kim, *J. Phys. Chem. B*, **2006**, *110*(15), 7938–7943.

[112] D. H. Kim, D. S. Choi, A. S. Kim, S. K. Hong, and S. H. Kim, *Jpn. J. Appl. Phys. Part 1*, **2006**, *45*(3B), 2148–2150.

[113] X. Y. Peng, X. Y. Wang, L. M. Liu, Y. L. Wang, and Y. Q. Tan, *Chem. Phys.*, **2009**, *359*(1-3), 21–26.

[114] L. Papagno, L. S. Caputi, D. Frankel, Y. Chen, and G. J. Lapeyre, *Surf. Sci.*, **1987**, *189-190*, 199–203.

[115] C. U. S. Larsson, A. S. Flodstroem, U. O. Karlsson, and Y. Yang, *J. Vac. Sci Technol. A*, **1989**, *7*(3, Pt. 2), 2044–8.

[116] C. U. S. Larsson and A. S. Flodstroem, *Phy. Rev. B*, **1991**, *43*(11), 9281–9283.

[117] C. U. S. Larsson and A. S. Flodstroem, *Vacuum*, **1991**, *42*(4), 297–300.

[118] J. H. Cho, L. Kleinman, K. J. Jin, and K. S. Kim, *Phy. Rev. B*, **2002**, *66*(11), 113306/1–113306/4.

[119] A. Foeraker and D. J. Doren, *J. Phys. Chem. B*, **2003**, *107*(33), 8507–8510.

[120] R. Konecny and D. J. Doren, *J. Chem. Phys.*, **1997**, *106*(6), 2426–2435.

[121] J. H. Cho, K. S. Kim, S. H. Lee, and M. H. Kang, *Phy. Rev. B*, **2000**, *61*(7), 4503–4506.

[122] C. W. Lim, J. M. Soon, N. L. Ma, W. Chen, and K. P. Loh, *Surf. Sci.*, **2005**, *575*(1-2), 51–59.

[123] S. S. Bae, D. H. Kim, A. S. Kim, S. J. Jung, S. K. Hong, and S. H. Kim, *J. Phys. Chem. C*, **2007**, *111*(41), 15013–15019.

[124] D. H. Kim, S. S. Bae, S. K. Hong, and S. H. Kim, *Surf. Sci.*, **2010**, *604*(2), 129–135.

[125] J. S. Kachian and S. F. Bent; Adsorption of ethanethiol, ethanol, and mercaptoethanol on ge(100)-2x1.; In *Abstracts of Papers, 232nd ACS National Meeting, San Francisco, CA, United States, Sept. 10-14, 2006*, pages COLL–347–. American Chemical Society, 2006.

[126] J. Li, Y. Q. Qu, K. L. Han, and G. Z. He, *Surf. Sci.*, **2005**, *586*(1-3), 45–55.

[127] M. A. Filler, A. J. Keung, D. J. A. Van, and S. F. Bent; Unraveling carbonyl chemistry on ge(100)-2x1 using vibrational spectroscopy.; In *Abstracts of Papers, 232nd ACS National Meeting, San Francisco, CA, United States, Sept. 10-14, 2006*, pages COLL–210–. American Chemical Society, 2006.

[128] E. K. Hwang, D. H. Kim, Y. J. Hwang, A. S. Kim, S. K. Hong, and S. H. Kim, *J. Phys. Chem. C*, **2007**, *111*(16), 5941–5945.

[129] D. H. Kim, E. K. Hwang, S. K. Hong, and S. H. Kim, *Surf. Sci.*, **2006**, *600*(18), 3629–3632.

[130] S. Sioncke, H. C. Lin, L. Nyns, G. Brammertz, A. Delabie, T. Conard, A. Franquet, J. Rip, H. Struyf, S. De, Gendt, M. Mueller, B. Beckhoff, and M. Caymax, *J. Appl. Phys.*, **2011**, *110*(8), 084907/1–084907/8.

[131] T. F. Teng, W. L. Lee, Y. F. Chang, J. C. Jiang, J. H. Wang, and W. H. Hung, *J. Phys. Chem. C*, **2010**, *114*(2), 1019–1027.

[132] P. Ardalan, C. B. Musgrave, and S. F. Bent, *Langmuir*, **2009**, *25*(4), 2013–2025.

[133] P. Ardalan, Y. Sun, P. Pianetta, C. B. Musgrave, and S. F. Bent, *Langmuir*, **2010**, *26*(11), 8419–8429.

[134] Y. H. Min, S. J. Jung, Y. S. Youn, D. H. Kim, and S. H. Kim, *J. Am. Chem. Soc.*, **2010**, *132*(26), 9014–9.

[135] L. M. Nelen, K. Fuller, and C. M. Greenlief, *Appl. Surf. Sci.*, **1999**, *150*(1-4), 65–72.

[136] A. S. Kim, M. A. Filler, S. H. Kim, and S. F. Bent, *J. Am. Chem. Soc.*, **2005**, *127*(16), 6123–6132.

[137] C. M. Greenlief and P. Prayongpan; Adsorption and reaction of amines on germanium and silicon surfaces.; In *Abstracts, 39th Midwest Regional Meeting of the American Chemical Society, Manhattan, KS, United States, October 20-22*, pages MID04–030–. American Chemical Society, 2004.

[138] J. T. Law and E. E. Francois, *Ann. Ny. Acad. Sci.*, **1954**, *58*, 925–936.

[139] J. T. Law, *J. Phys. Chem.*, **1955**, *59*, 543–549.

[140] R. J. Madix and M. Boudart, *J. Catal.*, **1967**, *7*(3), 240–251.

[141] R. Ludeke and A. Koma, *Phys. Rev. Lett.*, **1975**, *34*(18), 1170–1173.

[142] L. Surnev and M. Tikhov, *Surf. Sci.*, **1982**, *123*(2-3), 505–518.

[143] D. A. Hansen and J. B. Hudson, *Surf. Sci.*, **1991**, *254*(1-3), 222–234.

[144] D. A. Hansen and J. B. Hudson, *Surf. Sci.*, **1993**, *292*(1-2), 17–32.

[145] T. Fukuda and T. Ogino, *Phy. Rev. B*, **1997**, *56*(20), 13190–13193.

[146] T. Fukuda, *Jpn. J. Appl. Phys. Part 2*, **1999**, *38*(12A), L1450–L1452.

[147] T. J. Grassman, S. R. Bishop, and A. C. Kummel, *Surf. Sci.*, **2008**, *602*(14), 2373–2381.

[148] T. Fukuda, *Surf. Sci.*, **1998**, *417*(2/3), L1149–L1153.

[149] J. M. Soon, C. W. Lim, K. P. Loh, N. L. Ma, and P. Wu, *Phy. Rev. B*, **2005**, *72*(11), 115343/1–115343/6.

[150] X. L. Fan, W. M. Lau, and Z. F. Liu, *J. Phys. Chem. C*, **2009**, *113*(20), 8786–8793.

[151] M. Durr and U. Hofer, *Surf. Sci. Rep.*, **2006**, *61*(12), 465–526.

[152] J. A. Appelbaum, G. A. Baraff, D. R. Hamann, H. D. Hagstrum, and T. Sakurai, *Surf. Sci.*, **1978**, *70*, 654–673.

[153] L. Surnev and M. Tikhov, *Surf. Sci.*, **1984**, *138*(1), 40–50.

[154] G. M. Zhidomirov, A. L. Pushkarchuk, A. I. Trokhimets, and S. G. Gagarin, *Poverkhnost*, **1984**, (6), 84–90.

[155] Y. J. Chabal, *Surf. Sci.*, **1986**, *168*(1-3), 594–608.

[156] L. B. Lewis, J. Segall, and K. C. Janda, *J. Chem. Phys.*, **1995**, *102*(18), 7222–7228.

[157] J. Y. Lee, J. Y. Maeng, A. Kim, Y. E. Cho, and S. Kim, *J. Chem. Phys.*, **2003**, *118*(4), 1929–1936.

[158] L. Papagno, X. Y. Shen, J. Anderson, G. Schirripa Spagnolo, and G. J. Lapeyre, *Phy. Rev. B*, **1986**, *34*(10), 7188–7191.

[159] J. Eggeling, G. R. Bell, and T. S. Jones, *J. Phys. Chem. B*, **1999**, *103*(44), 9683–9689.

[160] S. Shimokawa, A. Namiki, M. N. Gamo, and T. Ando, *J. Chem. Phys.*, **2000**, *113*(16), 6916–6925.

[161] J. G. Ekerdt and B. Gong; Thermal hydrogen reactions on doped and undoped si(100) and ge(100).; In *Book of Abstracts, 219th ACS National Meeting, San Francisco, CA, March 26-30, 2000*, pages COLL–340–. American Chemical Society, 2000.

[162] J. W. Cho and R. J. Nemanich, *Phy. Rev. B*, **1992**, *46*(19), 12421–12426.

[163] J. Y. Maeng, J. Y. Lee, Y. E. Cho, S. H. Kim, and S. K. Jo, *Appl. Phys. Lett.*, **2002**, *81*(19), 3555–3557.

[164] Y. Okamoto, *J. Phys. Chem. B*, **2002**, *106*(3), 570–573.

[165] K. W. Kolasinski, W. Nessler, A. Demeijere, and E. Hasselbrink, *Phys. Rev. Lett.*, **1994**, *72*(9), 1356–1359.

[166] C. Mui, S. F. Bent, and C. B. Musgrave, *J. Phys. Chem. B*, **2004**, *108*(47), 18243–18253.

[167] M. W. Radny, G. A. Shah, P. V. Smith, S. R. Schofield, and N. J. Curson, *J. Chem. Phys.*, **2008**, *128*(24), 244707.

[168] G. A. Shah, M. W. Radny, P. V. Smith, S. R. Schofield, and N. J. Curson, *J. Chem. Phys.*, **2010**, *133*(1), 014703.

[169] Binghai Yan, Chiyung Yam, Andreia Luisa da Rosa, and Thomas Frauenheim, *Phys. Rev. Lett.*, **2009**, *103*, 189701.

[170] A. Saedi, B. Poelsema, and H. J. W. Zandvliet, *Phy. Rev. B*, **2009**, *79*(15), 153402.

[171] D. Bodlaki, H. Yamamoto, D. H. Waldeck, and E. Borguet, *Surf. Sci.*, **2003**, *543*(1-3), 63–74.

[172] G. W. Cullen, J. A. Amick, and D. Gerlich, *J. Electrochem. Soc.*, **1962**, *109*(2), 124–127.

[173] K. Zhang and L. Yeh, *J. Vac. Sci Technol.*, **1981**, *19*(3), 628–630.

[174] Y. L. Li, Z. H. Cai, L. H. Sun, and Q. Z. Qin, *Acta Chimica Sinica*, **1990**, *48*(9), 851–855.

[175] K. Z. Zhang and Q. Z. Qin, *Chem. J. Chinese. U.*, **1995**, *16*(4), 599–602.

[176] K. Ikeda, S. Imai, and M. Matsumura, *Appl. Surf. Sci.*, **1997**, *112*, 87–91.

[177] M. Gothelid, G. LeLay, C. Wigren, M. Bjorkqvist, and U. O. Karlsson, *Surf. Sci.*, **1997**, *371*(2-3), 264–276.

[178] M. Gothelid, L. G. Le, C. Wigren, M. Bjorkqvist, and U. O. Karlsson, *Surf. Rev. Lett.*, **1998**, *5*(1), 119–124.

[179] B. Stankiewicz, *Appl. Surf. Sci.*, **2008**, *254*(14), 4380–4385.

[180] A. Sanchez-Castillo, G. H. Cocoletzi, and N. Takeuchi, *Surf. Sci.*, **2002**, *521*(3), 95–103.

[181] R. D. Schnell, F. J. Himpsel, A. Bogen, D. Rieger, and W. Steinmann, *Phy. Rev. B*, **1985**, *32*(12), 8052–8056.

[182] P. Mikolajczyk and B. Stankiewicz, *Cent. Eur. J. Phys.*, **2009**, *7*(2), 279–285.

[183] P. Mikolajczyk and B. Stankiewicz, *Appl. Surf. Sci.*, **2010**, *256*(15), 4822–4828.

[184] D. Terri and H. Greg, *Appl. Surf. Sci.*, **1998**, *123–124*(0), 66–70.

[185] J. Yota and V. A. Burrows, *J. Appl. Phys.*, **1991**, *69*(10), 7369–7371.

[186] M. Sakuraba, T. Matsuura, and J. Murota, *Mater. Res. Soc. Symp. Proc.*, **1999**, *535*(III-V and IV-IV Materials and Processing Challenges for Highly Integrated Microelectronics and Optoelectronics), 281–286.

[187] S. Y. Sun, Y. Sun, Z. Liu, D. I. Lee, S. Peterson, and P. Pianetta, *Appl. Phys. Lett.*, **2006**, *88*(2), 021903.

[188] K. B. Park, Y. H. Lee, and S. W. Lim, *Appl. Surf. Sci.*, **2008**, *254*(6), 1842–1846.

[189] C. X. Li, P. T. Lai, and J. P. Xu, *Microelectron. Eng.*, **2007**, *84*(9-10), 2340–2343.

[190] C. Mahata, M. K. Bera, A. K. Chakraborty, P. K. Bose, and C. K. Maiti, *Microelectron. Eng.*, **2008**, *85*(11), 2207–2212.

[191] X. F. Zhang, J. P. Xu, C. X. Li, P. T. Lai, C. L. Chan, and J. G. Guan, *Appl. Phys. Lett.*, **2008**, *92*(26), 262902/1–262902/3.

[192] Z. M. Jiang, J. Glatthaar, and Y. P. Lee, *J. Chem. Phys.*, **2009**, *131*(14), 144504/1–144504/12.

[193] C. X. Li and P. T. Lai, *Appl. Phys. Lett.*, **2009**, *95*(2), 022910/1–022910/3.

[194] J. P. Xu, X. Zou, C. X. Li, P. T. Lai, and C. L. Chan, *Appl. Phys. A. Mater.*, **2009**, *94*(2), 419–422.

[195] C. X. Li, C. H. Leung, P. T. Lai, and J. P. Xu, *Solid-State Electron.*, **2010**, *54*(7), 675–679.

[196] H. X. Xu, J. P. Xu, C. X. Li, and P. T. Lai, *Thin Solid Films*, **2010**, *518*(23), 6962–6965.

[197] M. Croset; Formation of an oxide film on a germanium semiconductor., **1965**.

[198] V. Pravdic, A. E. Wilcox, and Albert C. Zettlemoyer, *Surf. Sci.*, **1969**, *13*(1), 280–93.

[199] M. Sanders and J. H. Craig, *Thin Solid Films*, **2002**, *414*(2), 251–255.

[200] B. M. Davies and Jr. Craig, J. H., *Surf. Sci.*, **2003**, *529*(1-2), 231–236.

[201] V. I. Lyashenko and V. G. Litovchenko, *Soviet Phys.-Tech. Phys.*, **1958**, *3*, 422–428.

[202] N. D. Morgulis and R. I. Marchenko, *Ukrains'kii Fizichnii Zhurnal (Ukrainian Edition)*, **1961**, *6*, 376–85.

[203] I. A. Kirovskaya, L. G. Maidanovskaya, and V. N. Nagovitsin, *Zhurnal Fizicheskoi Khimii*, **1967**, *41*(9), 2219–2223.

[204] M. J. Sparnaay, *Surf. Sci.*, **1969**, *13*(1), 99–109.

[205] T. T. Bykova, *Uchenye Zapiski Leningradskogo Gosudarstvennogo Universiteta imeni A. A. Zhdanova, Seriya Fizicheskikh i Geologicheskikh Nauk*, **1970**, *No. 354*, 106–111.

[206] T. T. Bykova and N. S. Tsypkina, *Fiz. Tekh. Poluprov.*, **1971**, *5*(2), 262–265.

[207] J. Vonwienskowski, *Phys. Status Solidi B.*, **1978**, *88*(2), K169–K172.

[208] A. Ben Ephraim, Zippora Calahorra, and Mordechai. Folman, *J. Chem. Soc., Faraday Trans. 2*, **1979**, *75*(1), 158–68.

[209] T. Sakurai and H. D. Hagstrum, *Phy. Rev. B*, **1979**, *20*(6), 2423–2430.

[210] A. Lubezky and M. Folman, *J. Chem. Soc., Faraday Trans.1*, **1981**, *77*(4), 791–796.

[211] J. H. Choi, J. G. Ryou, Y. S. Youn, S. K. Hong, and S. H. Kim; Adsorption of co on ge(100) at room temperature.; In *Abstracts of Papers, 233rd ACS National Meeting, Chicago, IL, United States, March 25-29, 2007*, pages COLL–336–. American Chemical Society, 2007.

[212] O. V. Krylov, S. Z. Roginskii, and V. M. Frolov, *Doklady Akademii Nauk SSSR*, **1957**, *111*, 623–625.

[213] V. I. Lyashenko, G. F. Romanova, and I. I. Stepko, *Problemy Kinetiki i Kataliza*, **1960**, (No. 10), 111–116.

[214] G. G. Fedorov, R. V. Prudnikov, and V. F. Kiselev, *Phys. Status Solidi A.*, **1972**, *14*(1), K19–K21.

[215] V. F. Kiselev, R. V. Prudnikov, and G. G. Fedorov, *Doklady Akademii Nauk SSSR*, **1973**, *208*(2), 387–390.

[216] M. A. Filler, D. J. A. Van, D. W. Porter, and S. F. Bent; Carbonyl chemistry at the ge(100)-2x1 surface: Spectroscopic identification of complex reaction products.; In *Abstracts of Papers, 227th ACS National Meeting, Anaheim, CA, United States, March 28-April 1, 2004*, pages COLL–008–. American Chemical Society, 2004.

[217] M. A. Filler, D. J. A. Van, A. J. Keung, and S. F. Bent, *J. Am. Chem. Soc.*, **2006**, *128*(3), 770–779.

[218] S. Chiodo, F. Rondinelli, N. Russo, and M. Toscano, *J. Chem. Theory Comput.*, **2008**, *4*(2), 316–321.

[219] A. S. Ello, L. Pirault-Roy, A. Wootsch, Z. Paal, and A. Trokourey, *J. Soc. Ouest-Afr. Chim.*, **2008**, *13*(26), 21–27.

[220] P. H. Bideberripe, M. J. Ramallo-Lopez, J. A. S. Figueroa, A. M. Jaworski, L. M. Casella, and J. G. Siri., *Catal. Commun.*, **2011**, *12*(14), 1280–1285.

[221] M. Louis-Charles, C. Abdellah, C. Bernard, and F. Francois, *J. Chem. Soc., Faraday Trans.*, **1997**, *93*(20), 3715–3720.

[222] T. Ya Safonova and O. A. Petrii, *J. Electroanal. Chem.*, **1998**, *448*(2), 211–216.

[223] G. E. Dima, V. Rosca, and M. T. M. Koper, *J. Electroanal. Chem.*, **2007**, *599*(2), 167–176.

[224] Watanabe Masahiro, Shibata Masami, and Motoo Satoshi, *J. Electroanal. Chem. Interfacial Electrochem.*, **1985**, *187*(1), 161–74.

[225] G. Binnig, H. Rohrer, Ch. Gerber, and E. Weibel, *Phys. Rev. Lett.*, **1983**, *50*, 120–123.

[226] L. Gross, *Nature Chemistry*, **2011**, *3*(4), 273–278.

[227] J. Bardeen, *Phys. Rev. Lett.*, **1961**, *6*, 57–59.

[228] J. Tersoff and D. R. Hamann, *Phy. Rev. B*, **1985**, *31*(2), 805–813.

[229] M. Büttiker, Y Imry, R. Landauer, and S. Pinhas, *Phy. Rev. B*, **1985**, *31*(10), 6207–6215.

[230] A. Selloni, P. Carnevali, E. Tosatti, and C. D. Chen, Feb , **1985**, *31*, 2602–2605.

[231] N. D. Lang, *Phys. Rev. Lett.*, **1986**, *56*(11), 1164–1167.

[232] N. D. Lang, *Phy. Rev. B*, **1986**, *34*(8), 5947–5950.

[233] R. M Feenstra, J. A Stroscio, and A. P Fein, MAR , **1987**, *181*(1-2), 295–306.

[234] Fabian Mohn, Leo Gross, Nikolaj Moll, and Gerhard Meyer, April , **2012**, *7*(4), 227–231.

[235] J. Repp, G. Meyer, S. Paavilainen, F. E. Olsson, and M. Persson, *Science*, **2006**, *312*(5777), 1196–1199.

[236] P. Liljeroth, I. Swart, S. Paavilainen, J. Repp, and G. Meyer, *Nano Lett.*, **2010**, *10*(7), 2475–2479.

[237] C. Joachim, J. K. Gimzewski, and A. Aviram, *Nature*, **2000**, *408*(6812), 541–548.

[238] J. Repp, G. Meyer, S. M. Stojkovic, A. Gourdon, and C. Joachim, *Phys. Rev. Lett.*, **2005**, *94*(2), 026803.

[239] Fabian Mohn, Jascha Repp, Leo Gross, Gerhard Meyer, Matthew S. Dyer, and Mats Persson, *Phys. Rev. Lett.*, **2010**, *105*(26), 266102.

[240] J. Repp and G. Meyer, December , **2006**, *85*(4), 399–406.

[241] Q. M. Guo, M. Huang, Z. H. Qin, and G. Y. Cao, *Ultramicroscopy*, **2012**, *118*, 17–20.

[242] Z. H. Cheng, S. X. Du, N. Jiang, Y. Y. Zhang, W. Guo, W. A. Hofer, and H. . J. Gao, *Surf. Sci.*, **2011**, *605*(3-4), 415–418.

[243] M. Gyamfi, T. Eelbo, M. Wasniowska, T. O. Wehling, S. Forti, U. Starke, A. I. Lichtenstein, M. I. Katsnelson, and R. Wiesendanger, April , **2012**, *85*(16), 161406.

[244] R. E. Gilman, M. J. Novak, J. C. Baum, and J. A. Olson, *Journal of Physical Chemistry C*, **2008**, *112*(37), 14545–14548.

[245] J. B. Neaton, Mark S. Hybertsen, and Steven G. Louie, *Phys. Rev. Lett.*, **2006**, *97*, 216405.

[246] W. H. Soe, C. Manzano, A. De Sarkar, N. Chandrasekhar, and C. Joachim, *Phys. Rev. Lett.*, **2009**, *102*(17), 176102.

[247] A. Bellec, F. Ample, D. Riedel, G. Dujardin, and C. Joachim, *Nano Lett.*, **2009**, *9*(1), 144–147.

[248] C. J. Chen, *J. Vac. Sci. Tech. A*, **1988**, *6*(2), 319–322.

[249] C. J. Chen, November , **1990**, *42*(14), 8841–8857.

[250] L. Jurczyszyn and B. Stankiewicz, *Prog. Surf. Sci.*, **2003**, *74*(1-8), 185–200.

[251] R. Gaspari, S. Blankenburg, C. A. Pignedoli, P. Ruffieux, M. Treier, R. Fasel, and D. Passerone, *Phy. Rev. B*, **2011**, *84*(12), 125417.

[252] H. J. Lee and W. Ho, *Science*, **1999**, *286*(5445), 1719–1722.

[253] J. R. Hahn and W. Ho, *Phys. Rev. Lett.*, **2001**, *87*(19), 196102.

[254] Leo Gross, Nikolaj Moll, Fabian Mohn, Alessandro Curioni, Gerhard Meyer, Felix Hanke, and Mats Persson, *Phys. Rev. Lett.*, **2011**, *107*(8), 086101.

[255] G. Kichin, C. Weiss, C. Wagner, F. S. Tautz, and R. Temirov, *J. Am. Chem. Soc.*, **2011**, *133*(42), 16847–16851.

[256] Zhihai Cheng, Shixuan Du, Wei Guo, Li Gao, Zhitao Deng, Nan Jiang, Haiming Guo, Hao Tang, and H. . J. Gao, *Nano Research*, **2011**, *4*(6), 523–530.

[257] R. Temirov, S. Soubatch, O. Neucheva, A. C. Lassise, and F. S. Tautz, May , **2008**, *10*, 053012.

[258] C. Weiss, C. Wagner, C. Kleimann, M. Rohlfing, F. S. Tautz, and R. Temirov, *Phys. Rev. Lett.*, **2010**, *105*(8), 086103.

[259] J. I. Martinez, E. Abad, C. Gonzalez, F. Flores, and J. Ortega, *Phys. Rev. Lett.*, **2012**, *108*(24).

[260] Q. M. Xu, L. J. Wan, S. X. Yin, C. Wang, and C. L. Bai, *J. Phys. Chem. B*, **2001**, *105*(43), 10465–10467.

[261] Z. T. Deng, H. Lin, W. Ji, L. Gao, X. Lin, Z. H. Cheng, X. B. He, J. L. Lu, D. X. Shi, W. A. Hofer, and H. J. Gao, April , **2006**, *96*(15), 156102.

[262] Ye-liang Wang, Zhi-hai Cheng, Zhi-tao Deng, Hai-ming Guo, Shi-xuan Du, and Hong-jun Gao, *Chimia*, **2012**, *66*(1-2), 31–37.

[263] F. Matino, G. Schull, F. Koehler, S. Gabutti, M. Mayor, and R. Berndt, *Proc. Natl. Acad. Sci. U. S. A.*, **2011**, *108*(3), 961–964.

[264] M. Grobis, X. Lu, K. H. Khoo, S. G. Louie, and M. F. Crommie; Energy resolved imaging of fullerene molecular orbitals; In P. M. Koenraad and M. Kemerink, Ed., *Scanning Tunneling Microscopy/Spectroscopy and Related Techniques*, Vol. 696 of *American Institute of Physics Conference Series*, pages 20–27, 2003.

[265] H. Ibach and D. L. Mills, *Electron Energy Loss Spectroscopy and Surface Vibrations;* Academic Press, 1982.

[266] A. A. Lucas and M. Šunjić, *Phys. Rev. Lett.*, **1971**, *26*, 229–232.

[267] P. Hohenberg and W. Kohn, *Phys. Rev.*, **1964**, *136*(3B), B864–B871.

[268] W. Kohn and L. J. Sham, *Phys. Rev.*, **1965**, *140*(4A), A1133–A1138.

[269] C. E. Brion, G. Cooper, Y. Zheng, I. V. Litvinyuk, and I. E. McCarthy, *Chem. Phys.*, **2001**, *270*(1), 13–30.

[270] J. P. Perdew and Alex Zunger, *Phy. Rev. B*, **1981**, *23*(10), 5048–5079.

[271] J. P. Perdew and Y. Wang, *Phy. Rev. B*, **1992**, *45*(23), 13244–13249.

[272] J. P. Perdew, K. Burke, and M. Ernzerhof, *Phys. Rev. Lett.*, **1996**, *77*(18), 3865–3868.

[273] C. T. Lee, W. T. Yang, and R. G. Parr, *Phy. Rev. B*, **1988**, *37*(2), 785–789.

[274] D. J. Chadi and Marvin L. Cohen, *Phy. Rev. B*, **1973**, *8*, 5747–5753.

[275] H. J. Monkhorst and J. D. Pack, *Phy. Rev. B*, **1976**, *13*(12), 5188–5192.

[276] Thomas A. H. and William N. L., *Chem. Phys. Lett.*, **1977**, *49*(2), 225 – 232.

[277] S. J. Clark, M. D. Segall, C. J. Pickard, P. J. Hasnip, M. J. Probert, K. Refson, and M. C. Payne, *Zeitschrift Fur Kristallographie*, **2005**, *220*(5-6), 567–570.

[278] J. M. Soler, E. Artacho, J. D. Gale, A. Garcia, J. Junquera, P. Ordejon, and D. Sanchez-Portal, *J. Phys.: Condens. Matter.*, **2002**, *14*(11), 2745–2779.

[279] L. Kleinman and D. M. Bylander, *Phys. Rev. Lett.*, **1982**, *48*(20), 1425–1428.

[280] A. D. Becke, *Phys. Rev. A.*, **1988**, *38*(6), 3098–3100.

[281] H. T. Zhou, J. H. Mao, G. Li, Y. L. Wang, X. L. Feng, S. X. Du, K. Muellen, and H. J. Gao, *Appl. Phys. Lett.*, **2011**, *99*(15), 153101.

[282] P. Liljeroth, J. Repp, and G. Meyer, *Science*, **2007**, *317*(5842), 1203–1206.

[283] H. Yang, O. Boudrioua, A. J. Mayne, G. Comtet, G. Dujardin, Y. Kuk, P. Sonnet, L. Stauffer, S. Nagarajan, and A. Gourdon, *Phys. Chem. Chem. Phys.*, **2012**, *14*(5), 1700–1705.

[284] S. Breda, I. D. Reva, L. Lapinski, M. J. Nowak, and R. Fausto, *J. Mol. Struct.*, **2006**, *786*(2-3), 193–206.

[285] E. M. Crabb and M. K. Ravikumar, *Electrochim. Acta*, **2001**, *46*(7), 1033–1041.

[286] P. Shiller and A. B. Anderson, *Surf. Sci.*, **1990**, *236*(3), 225–32.

[287] M. Watanabe and S. Motoo, *J. Electroanal. Chem. Interfacial Electrochem.*, **1986**, *202*(1-2), 125–35.

[288] F. Figueras and B. Coq, *NATO ASI Ser., Ser. C*, **1996**, *474*, 163–84.

[289] R. Mariscal, J. L. G. Fierro, J. C. Yori, J. M. Parera, and J. A. Grau, *Appl. Catal., A.*, **2007**, *327*(2), 123–131.

[290] K. Fukutani, T. T. Magkoev, Y. Murata, and K. Terakura, *Surf. Sci.*, **1996**, *363*(1-3, Proceedings of the International Symposium on Dynamical Quantum Processes on Solid Surfaces, 1995), 185–194.

[291] K. Fukutani, T. T. Magkoev, Y. Murata, M. Matsumoto, T. Kawauchi, T. Magome, Y. Tezuka, and S. Shin, *J. Electron Spectrosc. Relat. Phenom.*, **1998**, *88*, 597–601.

[292] N. Oncel, *J. Phys.: Condens. Matter*, **2008**, *20*(39), 393001.

[293] O. Gurlu, O. A. O. Adam, H. J. W. Zandvliet, and B. Poelsema, *Appl. Phys. Lett.*, **2003**, *83*(22), 4610–4612.

[294] N. Oncel, W. J. van Beek, J. Huijben, B. Poelsema, and H. J. W. Zandvliet, *Surf. Sci.*, **2006**, *600*(20), 4690–4693.

[295] D. Kockmann, B. Poelsema, and H. J. W. Zandvliet, *Phys. Rev. B*, **2008**, *78*(24), 245421/1–245421/5.

[296] A. A. Stekolnikov, J. Furthmuller, and F. Bechstedt, *Phy. Rev. B*, **2008**, *78*(15), 155434.

[297] Y. Yamashita, M. Z. Hossain, K. Mukai, and J. Yoshinobu, *Phy. Rev. B*, **2003**, *68*(3), 033314.

[298] J. P. Chamberlain, J. L. Clemons, A. J. Pounds, and H. P. Gillis, *Surf. Sci.*, **1994**, *301*(1-3), 105–117.

[299] D. Q. Hu, W. Ho, X. J. Chen, S. Wang, and W. A. Goddard, *Phys. Rev. Lett.*, **1997**, *78*(6), 1178–1181.

[300] F. T. Bacalzo, D. G. Musaev, and M. C. Lin, *J. Phys. Chem. B*, **1998**, *102*(12), 2221–2225.

[301] Y. Imamura, N. Matsui, Y. Morikawa, M. Hada, T. Kubo, M. Nishijima, and H. Nakatsuji, *Chem. Phys. Lett.*, **1998**, *287*(1-2), 131–136.

[302] F. Bacalzo-Gladden and M. C. Lin, *J. Phys. Chem. B*, **1999**, *103*(34), 7270–7276.

[303] C. H. Kleint and W. Moldenhauer, *Transactions of International Vacuum Congress 3rd, Stuttgart*, **1966**, *2*(Pt. 2), 475–479.

[304] N. Troullier and J. L. Martins, *Phy. Rev. B*, **1991**, *43*(3), 1993–2006.

[305] http://www.icmab.es/siesta/.

[306] R. Dronskowski and P. E. Blochl, *J. Phys. Chem.*, **1993**, *97*(33), 8617–8624.

[307] H.J.W. Zandvliet, *Phys. Rep.*, **2003**, *388*(1), 1–40.

[308] X. Torrelles, H. A. VanderVegt, V. H. Etgens, P. Fajardo, J. Alvarez, and S. Ferrer, *Surf. Sci.*, **1996**, *364*(3), 242–252.

[309] W. V. Glassey, G. A. Papoian, and R. Hoffmann, *J. Chem. Phys.*, **1999**, *111*(3), 893–910.

[310] C.E Housecroft and A. G. Sharpe, *Inorganic Chemistry;* Pearson Education Limited, England, 2005.

[311] D. E. P. Vanpoucke and G. Brocks, *Phy. Rev. B*, **2010**, *81*(8), 085410.

[312] G. Blyholder, *J. Phys. Chem.*, **1964**, *68*(10), 2772–2777.

[313] C. O. Chui, S. Ramanathan, B. B. Triplett, P. C. McIntyre, and K. C. Saraswat, *IEEE Electr. Device. L.*, **2002**, *23*(8), 473–475.

[314] M. L. Lee, C. W. Leitz, Z. Cheng, A. J. Pitera, T. Langdo, M. T. Currie, G. Taraschi, E. A. Fitzgerald, and D. A. Antoniadis, *Appl. Phys. Lett.*, **2001**, *79*(20), 3344–3346.

[315] K. Kutsuki, G. Okamoto, T. Hosoi, T. Shimura, and H. Watanabe, *Appl. Phys. Lett.*, **2009**, *95*(2), 022102.

[316] C. O. Chui, F. Ito, and K. C. Saraswat, *IEEE Electr. Device. L.*, **2004**, *25*(9), 613–615.

[317] D. Kuzum, A. J. Pethe, T. Krishnamohan, Y. Oshima, Y. Sun, J. P. McVittie, P. A. Pianetta, P. C. McIntyre, and K. C. Saraswat, *Tech. Dig.*, **2007**, *2*, 723–726.

[318] B. M. Davies and J. H. Craig, *Appl. Surf. Sci.*, **2003**, *205*(1-4), 22–26.

[319] M. Carbone, K. Bobrov, G. Comtet, G. Dujardin, and L. Hellner, *Surf. Sci.*, **2000**, *467*(1-3), 49–57.

[320] Y. K. Kim, J. R. Ahn, W. H. Choi, H. S. Lee, and H. W. Yeom, *Phy. Rev. B*, **2003**, *68*(7), 075323.

[321] S. Jeong, *J. Korean Phys. Soc.*, **2007**, *51*, 1962.

[322] K. Kato, Y. Nakasaki, and T. Uda, *Phys. Rev. B*, **2002**, *66*, 075308.

[323] G. Nelin and G. Nilsson, *Phy. Rev. B*, **1974**, *10*, 612–620.

[324] B. M. Davies and J. H. Craig, *Surf. Sci.*, **2003**, *529*(1-2), 231–236.

[325] J. H. Choi, J. G. Ryou, Y. S. Youn, S. K. Hong, and S. H. Kim; Adsorption of co on ge(100) at room temperature; Number Abstracts of Papers, 233rd ACS National Meeting, pages COLL–336, Chicago, IL, United States, 2007. American Chemical Society.